Stability of the floating ice shelf of the Petermann glacier and its response to a changing environment

J.F. Rosier

TU Delft Delft University of Technology

Danmarks Meteorologiske Institut

Stability of the floating ice shelf of the Petermann glacier and its response to a changing environment

By

J.F. Rosier

in partial fulfilment of the requirements for the degree of

Master of Science
in Civil Engineering

at the Delft University of Technology,
to be defended publicly on Monday August 19, 2019 at 10:30 AM.

Supervisors:	Dr. S. Lhermitte	TU Delft
	Dr. R. Mottram	DMI
Thesis committee:	Dr. S. Lhermitte	TU Delft
	Dr. M. Vizcaino,	TU Delft
	Dr. Ir. B. Wouters	TU Delft

Abstract

Nearly all major glaciers in Greenland have reduced in size over the last two decades. An increase in the amount of ice transported from the Greenland ice sheet to the oceans is predicted following an increase in Arctic air and ocean temperatures. One of the last glaciers with a floating ice shelf and draining a substantial area of the Greenland ice sheet is the Petermann glacier in North West Greenland. With two major calving events in 2010 and 2012 the extent of its floating ice shelf was reduced to only half of that prior to 2010 and since 2016 new fractures indicate a new calving event is predicted to reduce the length of the glacier by ~14 km.

Multiple studies have indicated that after the major calving event of 2012 the glacier accelerated and a new increase in the velocity, possibly linked to the next calving event, has already been observed. With every part of the glacier's ice shelf that is lost the resistive force that holds the glacier back is reduced and the amount of ice drained to the ocean increases. Losing its entire ice shelf could lead to a significant increase in the contribution of the Petermann glacier to global sea level rise as the Petermann fjord extends inlands below sea level for nearly a hundred kilometers.

This study uses ice thickness and surface elevation data combined with velocity data from different sources to analyze the current and future stability of the Petermann glacier. Ice thickness and the velocity data is used as input in a fracture model in order to investigate the different contributions of stress, thinning and an increase in the availability of surface water to the depth crevasses can reach. The areas on the glacier that show locations where crevasses penetrate deep into the ice indicate that the glacier is vulnerable to fracturing in those spots. Connected weak spots might indicate further potential for future calving events.

The results derived from the thickness data and the subsequent melt rates show that near the grounding line the glacier is experiencing significantly larger melt rates than near the calving front. The high melt rates are concentrated in space and caused three large basal channels to form, which run downstream parallel to the flow direction. The location of the western channel corresponds to the location of fractures that initiated during the same time the channel deepened, indicating a relationship between an increase in melt rate and fracturing. This relation is also observed in the results from the fracture model, where there is enough water and the ice shelf thinness fractures are capable of penetrating deep in the glacier ice. The results also show that when the average melt rate between 2011 and 2017 continues to prevail the floating ice shelf of the Petermann might be gone within the next decade.

Contents

Title 1
Abstract 5
1. Introduction 15
1.1 Arctic climate change 15
1.2 Petermann glacier 15
1.2.1 History of exploration 15
1.2.2 Current stability of the Petermann glacier 16
1.2.3 Response to instability 17
1.2.4 Calving and fracture modelling 17
1.2 Thesis aim and outline 17
1.2.1 Aim 17
1.2.2 Outline 18
2. Background 19
2.1 General background 19
2.1.1 Overview of the Petermann glacier 19
2.1 .2 Petermann fjord 20
2.2 Melt rate from ice thickness change 22
2.3 Introduction to linear elastic fracture mechanics (LEFM) 23
2.3.1 Modes of fracturing 23
2.3.2 From velocity to strain to stress 24
2.3.3 Fracture mechanics 25
2.3.4 Linear elastic fracture mechanics applied to glaciers 28
3. Data 35
3.1 Atmospheric data and regional climate model output 36
3.2 Surface elevation and bottom draft 37
3.2.1 Operation (pre-) IceBridge 37
3.2.2 ArcticDEM 38
3.2.3 Earth Gravity Model 38
3.2.4 Tide Model 38
3.3 Velocity data 39
3.4 Fracture tracking data 40

4. Method 41
4.1 Climate model and temperature data statistics 42
4.1.1 Temperature statistics 42
4.1.2 HIRHAM5/MODIS runoff and surface mass balance 42
4.2 Pre-IceBridge and Operation IceBridge 42
4.3 ArcticDEM thickness change and basal melt rate 43
4.3.1 Ice thickness from surface elevation 43
4.3.2 Drainage from surface elevation and drainage threshold 44
4.3.3 Eulerian and Lagrangian thickness change from ArcticDEM. 44
4.3.4 Basal Melt rate 44
4.4 Velocity, strain and stress 45
4.4.1 Inter-annual velocity variation 45
4.4.2 Stress and strain calculation 45
4.4.3 Intra-annual velocity and tensile stress variation 46
4.5 Fracture tracking 46
4.6 Linear elastic fracture mechanics crevasse depth model 46
4.6.1 Experiment 1 47
4.6.2 Experiment 2 47
4.6 3 Experiment 3 47
4.6 4 Experiment 4 47
5. Results 49
5.1 Atmospheric results 50
5.1.1 Temperature evolution 50
5.1.2 Evolution of Runoff 52
5.1.3 Runoff drainage paths 53
5.2 Ice thickness, thickness change and melt rates 53
5.2.1 Ice thickness 53
5.2.2 Surface elevation + bottom draft and thickness change profiles 54
5.2.3 Surface elevation derived ice thickness change 57
5.2.3 Melt rates 57
5.3 Velocity and stress 58
5.3.1 Velocity transects 58
5.3.2 Intra-annual velocity and stress variation 59
5.3 Observed fractures and fracture propagation 60
5.4 Linear Elastic Fracture Mechanics results 61
5.4.1 Comparison between observed and modelled crevasses 61

5.4.2 Effect of an increase in water 62
5.4.3 Effect of a reduction in ice thickness 63
5.4.4 Effect of a change in stress 64
6. Discussion 65
6.1 Temperature and surface hydrology: 65
6.1.1 Temperature 65
6.1.2 Drainage 66
6.2 Thickness change and melt rates 66
6.2.1 Evolution of the thickness change rate 66
6.2.2 Average thickness change and basal melt rate 67
6.3 Velocity and stress 67
6.3.1 Velocity transects 67
6.3.2 Inter annual velocity and stress variation 68
6.4 Observed fractures 68
6.4.1 Zone A 68
6.4.2 Zone B 68
6.4.3 Zone C 69
6.5 LEFM crevasse depth modelling 69
6.5.1 Sources of uncertainty 69
6.5.2 Experiments 70
7. Conclusions 71
7.1 Temperature and surface hydrology 71
7.2 Thickness change and melt rates 71
7.3 Velocity and stress 72
7.4 Fracturing due to channelized bottom melt and velocity gradients 72
7.5 Crevasse depth modelling based on future scenarios 72
7.6 Future stability of the Petermann glacier 73
8. Bibliography 74

Figures

Figure 1 Sentinel-2 image of 18-08-2018 showing the floating ice shelf of the Petermann glacier with newly observed fractures and main rift outlined. Location of the Petermann glacier in Greenland shown in top image. Image by: Uwe Dedering, Creative Commons license. 16

Figure 2 Envisat Meris image from 2008-07-01. North West Greenland with the location of the Petermann, Steensby, Ryder and H.C. Ostenfeld glacier. 20

Figure 3 Top: Petermann fjord bathymetry along the east with the connection to the Nares strait on the right side. Bottom: Petermann fjord bathymetry along the east with the connection to the Nares strait on the right side. Image altered from Tinto et al. (2015) 21

Figure 4 Schematic overview of the Petermann fjord showing the path of the different water layers under the floating ice shelf. Warm deep water flows over the sill and reaches the ice shelf near the grounding line. The melt water flows out of the fjord at intermediate depths (grey zone). Image from Johnson et al. 2011 22

Figure 5 Schematic overview of the three different terms in the mass balance of a floating section of a glacier at time t in blue and t+Δt in orange. At both time steps the glacier is cut-off at point A and B. Change in ice thickness between blue and orange glacier is due to the three terms in the mass balance. 23

Figure 6 Opening mode (mode 1), Sliding mode (mode 2) and Tearing mode (mode). Image from Van der Veen (1998b) 24

Figure 7 Schematic overview of the increase in stress intensity related to crack growth. Blue area signifies the stress free zone after fracture propagation over distance a. Red lines signifies the “path” of the stress through the object. The densification of the lines near the fracture tip represents the increase in stress intensity. Image from: fracturemechanics.org 26

Figure 8 Different energy terms related to crack growth. The atomic bond energy in blue shows that the energy required for the breaking of atomic bonds increases with fracture length. Green shows the release of energy with increasing fracture length. Sum of the two, in red, shows that until a certain point energy is required for further fracture growth and after that energy is released with increasing fracture length. Image from fracturemechanics.org 27

Figure 9 Schematic overview of crevasses in an ice shelf. Where d: depth of crevasse, a: water level below surface, w: half width between crevasses, Rxx: tensile stress. Image edited from Van der Veen (1998). 29

Figure 10 Sensitivity of the ice thickness to the SIF. The fracture toughness is plotted as dotted line. 30

Figure 11 Sensitivity of the crevasse spacing to the SIF. The fracture toughness is plotted as dotted line 31

Figure 12 Sensitivity of the ice thickness to the SIF as function of the tensile stress and lithostatic pressure. For the SIF due to tensile stress the formulation including the crevasse spacing is used. The fracture toughness is plotted as dotted line. 32

Figure 13 Stress intensity plots as function of crevasse depth on the left. SIF is cut off once the fracture toughness is reached. Final crevasse depth on the right. Final crevasse depth corresponds to the depth where the fracture toughness is reached. 34

Figure 14 ENVISAT Meris image of NW-Greenland and Ellesmere Island containing the locations of the Alert weather station, the automatic weather station and the AOI over the Petermann glacier. Green and purple lines show the flight paths of the PIB/OIB data set. 36

Figure 15 Top panel: OIB radar echogram example of the Thwaites glacier (Antarctica) showing the power of the return signal relative to the send signal along the depth relative to the WGS-84 ellipsoid. Bottom panel: surface profile in grey and bottom profile in b 37

Figure 16 Figure 2 Velocity data availability and corresponding time difference between images used for intensity/feature tracking. Colour of the dots represent the spatial coverage of Petermann's floating ice shelf. ERS-1/ERS-2/ENVISAT ranges from Aug-1991 to May-2010, Sentinel-1 ranges from Jan-2015 till July-2018. 39

Figure 17 Interpolation of the velocity data to rotated grid (left). Rotation of the interpolated velocity with the angle of the average flow direction 45

Figure 18 Left: Monthly average temperate of: AWS on the Petermann glacier, Alert weather station Canada and HIRHAM5 temperature output average of the Petermann floating ice shelf. Right: scatter plot between Alert and AWS in blue and HIRHAM5 and AWS in orange. Dashed black line shows a 1:1 ratio between temperatures. 50

Figure 19 Top: All available temperature data between January 1957 and July 2018 of Alert weather station and between January 1980 and January 2017 HIRHAM5 model output. Bottom: Alert weather station temperature and HIRHAM5 model output between January 1998 and January 2017 with a linear trend fitted through the temperature data starting at January 1998. 50

Figure 20 Summer (June, July and August), winter (December, January and February) and total annual temperature anomalies from the Alert weather station between 1957 and 2018 with respect to the respective summer, winter and total averages of the 1957-1971 period. Dashed black line shows the zero anomaly. 51

Figure 21 Runoff from HIRHAM5/MODIS model between 1980 and 2017 over a Landsat-8 image from: 2018-07-18. Top left: Linear trend in runoff per cell between 1980 and 2000. Top right: Linear trend in runoff per cell between 2000 and 2017. Bottom left: average runoff 52

Figure 22 Drainage paths of the Petermann glacier based on 2017 surface elevation. Only drainage paths that drain more than 5000 cells are shown. 53

Figure 23 Surface elevation derived ice thickness of 2017. Basal channels from left to right: western channel, central channel and eastern channel. Ice shelf on either side of the central channel are named ambient ice shelfs. Fracture zones A,B and C in blue. Fracture zone identified in PIB/OIB flight line West as green dots. 2017 grounding zone as solid black line. 54

Figure 24 A: Surface elevation and bottom draft along the Western flight line of pre-OIB/OIB between 2002 and 2017. B: The average thickness change per year in a Eulerian framework smoothed with a moving average filter with a window size of 10 km. C: Surface elevation and bottom draft profiles shifted along the flight line to match the position of the 2017 profile. D: The thickness change rate in a Lagrangian framework smoothed with a moving average filter with a window size of 300 m where only floating ice is compared. The change from grounded to floating ice in the grounding zone is shown as two vertical black dotted lines and the location where new fractures

have been observed as the fracture zone in blue. All profiles are referenced to the sea level which is shown as the horizontal zero line. 55

Figure 25 A: Surface elevation and bottom draft along the Central Eastern flight line of pre-OIB/OIB between 2002 and 2017. B: The average thickness change per year in an Eulerian framework smoothed with a moving average filter with a window size of 20 km. C: Surface elevation and bottom draft profiles shifted along the flight line to match the position of the 2017 profile. D: Thickness change rate in a Lagrangian framework smoothed with a moving average filter with a window size of 300 m where only floating ice is compared. The change from grounded to floating ice in the grounding zone shown as two vertical black dotted lines and the location where new fractures have been observed as the fracture zone in blue. All profiles are referenced to the sea level which is shown as the horizontal zero line. 56

Figure 26 Thickness change rates over the Petermann glacier. Background: Sentinel-2 Aug-2016 image with latitude on the vertical and longitude on the horizontal axis. Left: Lagrangian ice thickness change between 2011 and 2017 derived from surface elevation data between the two flow lines shown as black dashed lines. Two grounding zones are shown which mark the transition from floating to grounded ice of the 2017 thickness in black and of the 2011 thickness in orange. Right: Thickness change in an Eulerian framework over the entire floating ice shelf with the grounding zone of 2017 and 2011 at the same location shown in black. 57

Figure 27 Melt rates over the Petermann glacier. Background: Sentinel-2 Aug-2016 image with latitude on the vertical and longitude on the horizontal axis. Two grounding zones are shown which mark the transition from floating to grounded ice of the 2017 thickness in black and of the 2011 thickness in orange. Left: Basal melt rate between 2011 and 2017 derived from the Lagrangian thickness change and the SMB. Right: SMB over the Petermann glacier from HIRHAM5/MODIS output 58

Figure 28 Top and bottom left: Winter velocity (January, February, March) transect of ENVI/ERS-1/ERS-2 data up to 2011 and Sentinel-1 data from 2015 till 2019. Top right: Winter velocity (January, February, March) transect of ENVI/ERS-1/ERS-2 data up to 2011 and Sentinel-1 data from 2015 till 2019 with location of central channel between the two vertical black dashed lines. Bottom right: Overview of transect locations over Sentinel-2 Aug-2016 image with latitude on the vertical and longitude on the horizontal axis 59

Figure 29 Left: First principle stress average over the floating part of the glacier from 2015 till August 2018. Right: Ice velocity magnitude from 2015 till August 2018. All panels: Only data with at least 75% of spatial coverage is used. Months: June, July and August are in red. The rest of the months are in blue. 59

Figure 30 Top: Sentinel-2 images from 18-07-2018 of the Petermann glacier. Each zoom-in correspond to a location on the glacier where in since 2014 new fractures have appeared. Zoom-in B shows three separate fractures with each number located under the right tip of the respective fractures. The overview image has longitude on the horizontal and latitude on the vertical axes. Bottom: Fracture propagation of the three fractures shown in zoom-in B since fracture 1 started to form..... 60

Figure 31 Left: Sentinel-1 backscatter from 21-09-2017 over Petermann glacier with latitude along vertical and longitude along horizontal axis. Right: Crevasse depth over ice thickness ratio with tensile stress and ice thickness from July 2017 and water level at locations where water is available set 5 m below the surface. Data overlies Aug-2016 Sentinel-2 image of the Petermann glacier with latitude along vertical and longitude along horizontal axis. 61

Figure 32 Comparison of LEFM model output for two different water levels. Left: Crevasse depth over ice thickness ratio with tensile stress and ice thickness from July 2017 and water level at locations where water is available set 5 m below the surface. Right: Crevasse depth over ice thickness ratio difference between the situation with water versus the situation without water 62

Figure 33 Left: Difference in crevasse depth over ice thickness between situation with 2017 ice thickness versus situation with ice thickness of 2011. Right: Difference in crevasse depth over ice thickness between the situation with 2017 ice thickness versus situation with ice thickness of 2020. Green corresponds to locations where the applied thickness change caused the ice thickness to fall below zero and no fracture propagation is possible. 63

Figure 34 Left: Crevasse depth over ice thickness from winter situation without water availability. Right: Difference in crevasse depth over ice thickness between summer and winter situation 64

1. Introduction

1.1 Arctic climate change

For the past 50 years the average temperature in the Arctic has been increasing twice as fast compared to the rest of the world and, with a medium or high greenhouse gas scenario, the Arctic autumn and winter temperatures are projected to rise an additional 4-5 ^{0}C (AMAP 2017). The Arctic has played a dominant role in global sea level rise since 1974 with approximately 70% of the contribution of the Arctic to sea level rise coming from Greenland (AMAP 2017). The increase in mass loss from the Greenland ice sheet (GrIs) is both attributed to a decreasing surface mass balance (SMB) and an increase in ice discharge through marine-terminating glaciers (Rignot et al. 2010) . Rignot et al. (2008a) found that variations in ice discharge of marine-terminating glaciers are strongly linked to the SMB and can dominate the total mass balance of the Greenland ice sheet (GrIS). There is still a considerable amount of uncertainty when it comes to the drivers of mass loss of marine-terminating glaciers on Greenland (Carr et al. 2013). Many glaciers respond differently to the same kind of forcing due to differences in: basal topography, ice flow velocity or fjord geometry (Carr et al. 2013). This makes it hard to generalize and assume that different glaciers will respond equally to the changing climate. Uncertainties about how the Greenland ice sheet and its surrounding glaciers will respond to the projected warming make it hard to estimate the magnitude of future sea level rise (Carr et al. 2013), yet global sea level rise is expected to accelerate (SWIPA, 2017). Increasing the understanding about the interaction between processes that drive climate change in the Arctic and its effect on the Greenland glaciers is imperative for policy-makers all over the world (SWIPA, 2017). To increase the understanding on how marine terminating glaciers react to climate change the Petermann glacier, the fourth largest glacier in Greenland (Rignot and Kanagaratnam 2006), is discussed in this thesis.

1.2 Petermann glacier

1.2.1 History of exploration

The Petermann glacier has been the subject of many scientific papers and expeditions. First documented and discovered by C.F. Hall in 1871 during the American Polaris expedition (Kollmeyer 1980) and mapped by Koch in 1928 after two expeditions from 1917 and 1921 respectively. Higgins (1991) already observed the large water filled crevasses that lead to calving and noted that the largest tabular bergs lost from the Petermann glacier were approximately 10 by 12 km in size (Higgins 1991). With availability of remote sensing data growing so grew the understanding of the Petermann glacier. Contrarily to what was previously assumed Rignot (1996) found that, by using remote sensing data, the majority of mass loss from the Petermann glacier was due to basal melt instead of surface melt, with peak values near the grounding line. This was later confirmed by Rignot and Steffen (2008a) who calculated the steady state melt rate and showed that approximately 80% of the total mass loss occurred through basal melt. After the major calving event of 2010, where the glacier lost 270 km^2 of ice (Babiker and Miles 2013), the interest in the Petermann glacier intensified, yet Nick et al. (2012) found that losing ~25% of its ice shelf did not cause the Petermann glacier to accelerate. The next large calving event in 2012 where the glacier lost another ~130 km^2 did trigger an increase in the flow

velocity (Münchow et al. 2016),(Rückamp et al. 2019) and marked the furthest retreat in the observed history of the Petermann glacier (Babiker and Miles 2013). Johanessen et al. (2011) found that the calving event of 2010 was an extreme event within the 50 year period of observed calving on the Petermann glacier due to the size of the calved ice island as well as the calving front retreat associated with it. Johanessen et al. (2013) noted that the size of the calving event of 2012 was not extraordinary (~130 km^2 versus ~153 km^2 and ~168 km^2 in 1959 and 1991 respectively), but the short period of two years between two large calving events was not observed before on the Petermann glacier. Rignot and Steffen (2008) suggested that the Petermann glacier was vulnerable to calving due to channelized bottom melt and increased fracturing, but Johanessen et al. (2013) stated that there was not enough data available to determine whether the calving events of 2010 and 2012 are part of a natural cycle or that the retreat marked a permanent change in the calving front location.

1.2.2 Current stability of the Petermann glacier

According to Shroyer et al. (2017) it is possible that the Petermann glacier has reached a new quasi-equilibrium length of 40-45 km. The hypothesis of Shroyer et al. (2017) is based on outcome from a coupled sea-ice and ocean model. The model shows that the basal melt process that is associated with the calving events of 2010 and 2012 will not cause the glacier to retreat further than the calving front position of 2012 (Shroyer et al. 2017). Münchow et al. (2016) supports this hypothesis and states that the main rift currently visible near the calving front (Figure 1) indicates that the glacier will calve and retreat to approximately the same position as it did after the 2012 calving event.

According to Münchow et al. (2016) changes in the basal melt rate will determine whether the new-equilibrium position is stable or that the calving front position is only temporary and further retreat will follow. Wilson et al. (2017) showed high average basal melt rates near the grounding line of ~50 m a^{-1} using surface elevation derived ice thickness maps between 2011 and 2015. The values reported by Wilson et al. (2017) are higher than the basal melt rate of ~25 m a^{-1} between 2002/2003 observed by Rignot and steffen (2008), but the only observations on whether the melt rate is increasing are from Münchow et al. (2014). Münchow et al. (2014) showed that between 2007 and 2010 the average thickness decreased along the glacier by ~5 m a^{-1}.

Besides the main rift that Münchow et al. (2016) identified as the new calving front new fractures are forming in the south west of the floating ice shelf (Figure 1). The combination of newly observed fractures and high basal melt rates raises the question whether the Petermann glacier has indeed reached a new equilibrium length or that additional calving will lead to a positive feedback mechanism and eventually the collapse of the floating ice shelf of the Petermann glacier.

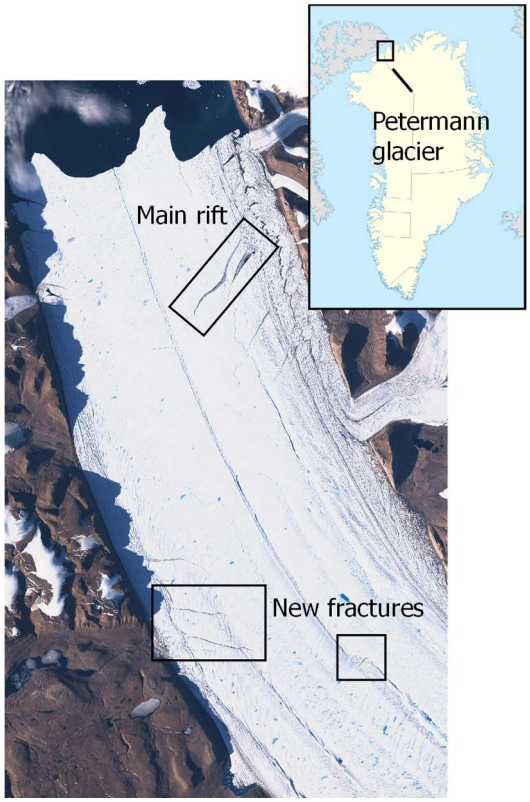

Figure 1 Sentinel-2 image of 18-08-2018 showing the floating ice shelf of the Petermann glacier with newly observed fractures and main rift outlined. Location of the Petermann glacier in Greenland shown in top image. Image by: Uwe Dedering, Creative Commons license.

1.2.3 Response to instability

The response of the Petermann glacier to forcing's such as an increase in basal melt and an increase in runoff has been discussed by Nick et al. (2010, 2012). Nick et al. (2012) showed that increasing the basal melt documented by Johnson et al (2011) by a factor three would remove the floating ice shelf completely and cause significant grounding line retreat. The responds of the Petermann to calving glacier is modelled by Rückamp et al. (2019) and Hill et al. (2018). Rückamp et al. (2019) was able to reconstruct the speed up after the 2012 calving event using the Ice Sheet System Model confirming the increase in velocity was due to a reduction in the buttressing stress that restrained the glacier flow. Rückamp et al. (2019) also showed that the ice berg associated with the next calving event is already dynamically detached from the ice shelf, which means it no longer provides resistance to glacier flow and that the Petermann glacier has experienced a velocity increase as a consequence. Hill et al. (2018) modelled the consecutive response of the flow velocity of the Petermann glacier to losing sections of its floating ice shelf. The thickness of the section that calves off determines the increase in velocity as thick sections provide more resistance to the glacier's flow compared to thin sections (Hill et al. 2018). A significant increase in the flow velocity at the grounding line is found after ice calves with an average thickness larger than 200 m, which is found within 12 km of the grounding line (Hill et al. 2018). Losing the entire ice shelf could eventually lead to a velocity increase at the grounding line of 96% (Hill et al. 2018). The increase in ice discharge following the loss of the entire ice shelf leads to an increase in the mass loss from the GrIS of ~14 Gt a^{-1} (currently ~11 Gt a^{-1}) and can increase even further if the grounding line would retreat further inland (Hill et al. 2018), since the Petermann fjord extents inland for ~100 kilometer as a canyon below sea level (Bamber et al. 2013) the potential for additional mass loss is significant.

1.2.4 Calving and fracture modelling

In order the model the response of the Petermann glacier to different forcing's Nick et al. (2012) used the method of Nye (1957) to calculate the calving front resulting from crevasses penetrating to a certain depth as described in Nick et al. (2010). The method of Nye (1955, 1957) is a simpler approach to crevasse modelling than the, more frequently used, linear elastic fracture mechanics (LEFM) model. The LEFM model is based on the principle that the stresses in the ice cause factures to propagate and is used in a broad spectrum of papers such as: Krug et al. (2014) who calculated the calving front of the Helheim glacier as part of a numeric ice flow model, Mottram and Benn (2009) attempting to recreate vertical crevasse fields on the Breiðamerkurjökull glacier using the approach of Van der Veen (1998) or Larour et al. (2004) who modelled the propagation of horizontal rifts on the Ronne ice shelf in Antarctica. Enderlin and Bartholomaus (2019) showed that the observed pattern of crevasses poorly matched the modelled crevasses over 19 Greenland glaciers using the Nye method. Mottram and Benn (2009) showed that the LEFM approach of Van der Veen resulted in a better match between observed and modelled crevasses than the Nye method, provided the necessary parameters were known. For this reason the LEFM approach of Van der Veen is used in this thesis to investigate crevasse propagation.

1.2 Thesis aim and outline

1.2.1 Aim

The aim of this thesis is to analyze the stability of the Petermann glacier in its current form and to make a prediction on the stability of the near future ice shelf in order to answer the main question:

How long will it approximately take before the floating ice shelf of the Petermann glacier collapses?

The main question stems directly from the observations by Münchow et al. (2016) and Shroyer et al. (2017) who speculate that the Petermann glacier has, possibly temporarily, reached a new quasi-equilibrium position with the main rift of Figure 1 marking the new calving front. However they also state that the glacier is most likely not in a steady state in its current form. Adding to the observations by Münchow et al. (2016) and Shroyer et al. (2017) newly observed fractures in the south west of the glacier possibly indicate a decrease in ice thickness (Bassis and Ma 2015). In order to analyze the stability of the Petermann glacier in its current form and to make a prediction on its future stability five objectives have been identified:

1. *Extend the analysis of Münchow et al. (2014, 2016) and Rückamp et al. (2019) in order to get more recent melt rates and velocity fields and identify any changes or lack of changes that indicate whether the glacier has reached a quasi-equilibrium.*

2. *Identify whether the additional thinning documented by Münchow et al (2014) is due to a decrease in the SMB or an increase in the basal melt rate. By identifying the source of the thinning and the underlying mechanism for its increase a projection is made for its future effect on the stability of the Petermann glacier.*

3. *Calculate the stresses from the velocity field in order to identify whether the increase in velocity following the speedup related to the calving event of 2012 and the detachment of the ice berg related to the main rift has led to an increase in the tensile stress on the glacier.*

4. *Identify any recently formed fractures on the Petermann glacier, track the propagation of these fractures over time and find a possible correlation between the location of these fractures and the updated melt rate maps.*

5. *Use the 2017 thickness map and stress field as input in the LEFM model to calculate the theoretical crevasse depth over the entire glacier for the current situation and compare the locations where crevasses are present based on objective 4 with the locations of the modelled crevasses. Then visualize the effect of continued melt rates, increased levels of stress and ample surface water availability on the propagation of crevasses to find whether additional crevassing is to be expected.*

1.2.2 Outline

With the availability of updated data sets of the velocity field up to July 2018 and thickness data up to July 2017 the analysis of the temporal and spatial variation of the melt rate and velocity field as performed by Münchow et al. (2014, 2016) and Rückamp et al. (2019) was extended. This analysis was supplemented by quantifying the increase in runoff by using output from the regional climate model HIRHAM5 combined with a MODIS albedo product described in (Peter L. Langen et al. 2017) and showing the velocity field derived stresses.

New fractures have been identified and their propagation was tracked over time. The location and time of formation was linked to basal melt rates and velocity gradients in order to assess what allowed these fractures to initiate. In order to estimate whether the conditions for further fracturing will become more favorable between 2017 and 2020 the effect of: thinning, an increase in stress and the availability of additional runoff on crevasse propagation using the LEFM approach of Van der Veen (1998) was assessed.

2. Background

In the background section first general information on the Petermann glacier and Petermann fjord is given. Second to further understand the process of basal melt and the influence of the fjord geometry and bathymetry on this process the interaction between ocean and the base of the Petermann glacier is explained. Third the process of calculating the basal melt and thickness change is discussed. Last after the ice-ocean interaction and thickness change is discussed background information is provided on the LEFM theory. Since the LEFM theory is generally not well known to people without an engineering background a more extensive introduction is provided including a sensitivity analysis showing the relative importance of different factors such as ice thickness and water availability on the propagation of crevasses.

2.1 General background

2.1.1 Overview of the Petermann glacier

The Petermann glacier drains approximately 6% of the Greenland ice sheet area, which makes it the fourth largest glacier in Greenland (Rignot and Kanagaratnam 2006) and is one of only seven glaciers with a floating ice shelf in Greenland (Moon et al. 2012). The glacier has an average velocity of ~1.2 km a^{-1} with summer velocities being 10-20% higher than winter velocities (Nick et al. 2012) and drains ~12 Gt of ice per year (Rignot and Steffen, 2008). At the point where the glacier becomes floating, also known as the grounding zone, the ice thickness is approximately 600 m and reduces to 200 m at the calving front (Münchow et al. 2016). The main cause of the thinning along the ~45 km long ice shelf is basal melt which accounts for approximately 80% of the mass loss (Rignot and Steffen, 2008). Prior to 2010 the floating ice shelf was approximately 70 km long, but lost a combined length of ~40 km during two calving events in 2010 and 2012 respectively (Johanessen et al. 2013). Snow accumulation is low as the north west of the Greenland ice sheet is one of its driest regions with the Petermann having a snow accumulation of just 10 cm in 2003, 2004 and 2005 (Rignot and Steffen, 2008, Steffen and Box, 2001). The glacier is located in the north west of Greenland and drains into the Petermann fjord (Figure 2). The Petermann fjord is connected with the Lincoln Sea and the Arctic Ocean in the north and the Atlantic Ocean in the south by the Nares Strait.

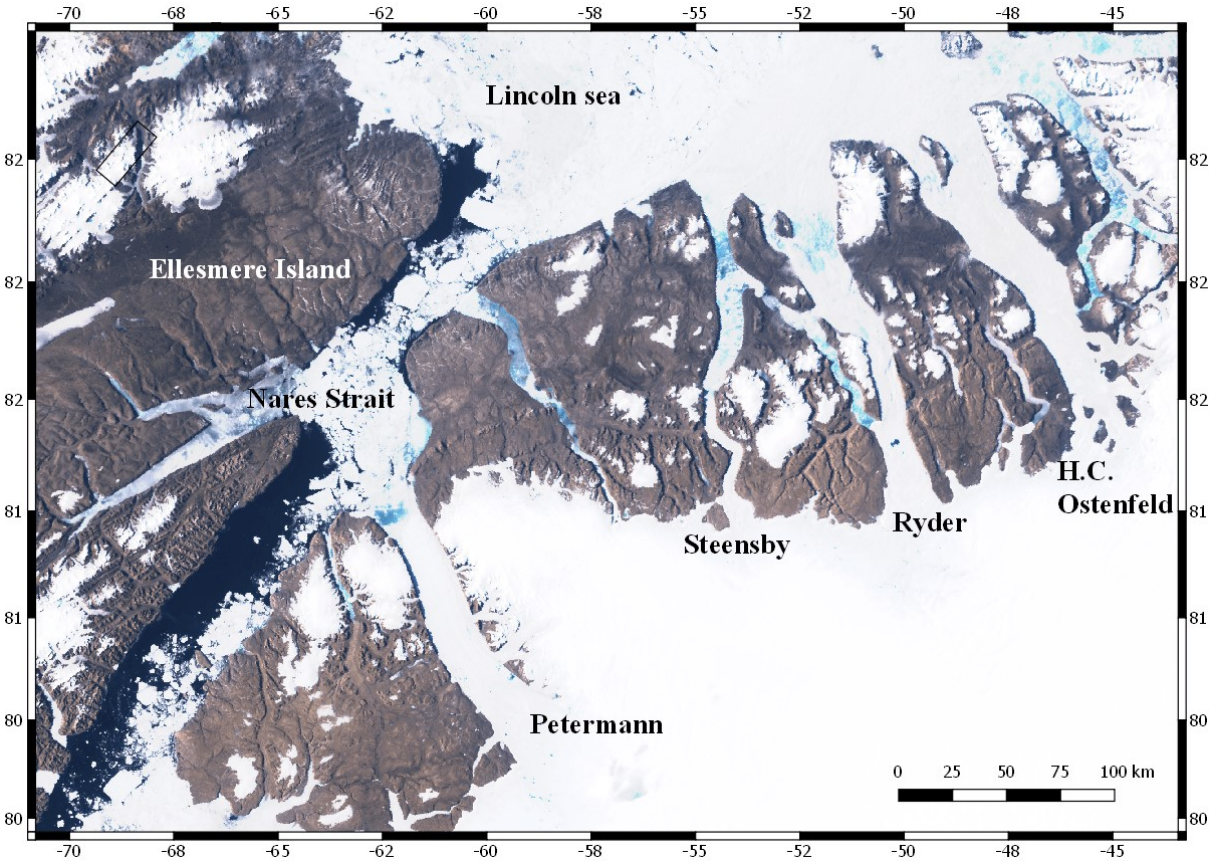

Figure 2 Envisat Meris image from 2008-07-01. North West Greenland with the location of the Petermann, Steensby, Ryder and H.C. Ostenfeld glacier.

2.1.2 Petermann fjord

The Petermann ice shelf is contained between the fjord walls of the Petermann fjord, reaching depths of over 1100 m at its deepest point see Figure 3. The Petermann fjord bathymetry can be divided in several sections. Near the grounding line the bed deepens and forms an inner basin. This inner basin is separated from the outer basin by an inner sill, which might have served as a stable grounding line position during a former retreat of the Petermann glacier (Tinto et al. 2015). The depth of the outer basin is around 300-600 m deeper on the east side of the fjord compared to the west side (Tinto et al. 2015). The outer sill that serves as a partial barrier between the Petermann fjord and the Nares strait is approximately 410-350 m deep and is located 85 km from the grounding line (Johnson et al. 2011).

The Nares Strait connects the Lincoln Sea with Baffin Bay with a prevailing southward current it transports sea ice from the Arctic to the Atlantic Ocean (Shroyer et al. 2015). The sea-ice is mobile in summer time, but can be halted and changed to a stationary state in winter time through the formation of an ice arch (Shroyer et al. 2015). An ice arch forms when particular large pieces of ice get wedged between Ellesmere Island and Greenland and block the flow of sea-ice. These ice arches play an important role in the amount of warm water that is provided to the Petermann fjord, as recent publication from Shroyer et al. (2017) shows the importance of incorporating the relation between sea ice in the Nares Strait and the amount of relative warm water that enters the Petermann fjord. When the sea ice in the Nares Strait is in a mobile state the wind stress that acts on the ocean surface causes an Ekman transport of westward, relative cool, surface water (Shroyer et al. 2015). This surface water is then replaced by upwelling deep relative warm salty water on the east side of the Nares Strait (Shroyer et al. 2015). Combined with an increase in exchange between water from the Petermann fjord and the Nares Strait due to eddy-induced circulation at the mouth of the Petermann glacier the

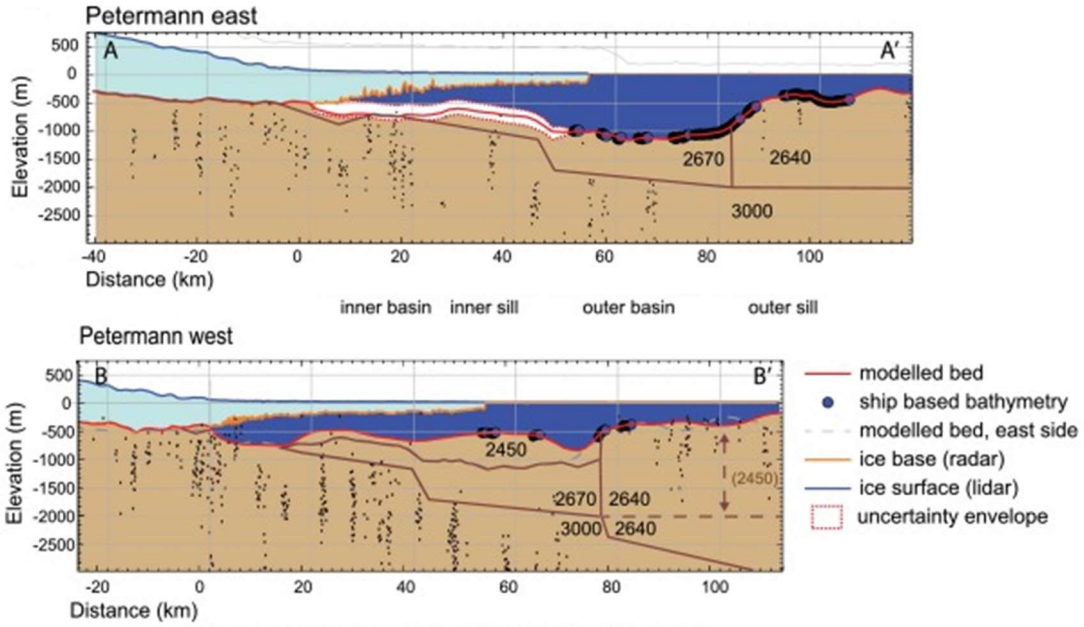

Figure 3 Top: Petermann fjord bathymetry along the east with the connection to the Nares strait on the right side. Bottom: Petermann fjord bathymetry along the east with the connection to the Nares strait on the right side. Image altered from Tinto et al. (2015)

mobile sea-ice state provides more warm water to the Petermann fjord compared to the stationary sea-ice state (Shroyer et al. 2017).

The effect of an increase in warm water in the Petermann fjord is expected to only affect the outer part of Petermann ice tongue where the ice draft is less than 200m (Shroyer et al. 2017).

The relative warm salty water that is responsible for the basal melt near the grounding line originates from the North Atlantic current (Münchow et al. 2016). The North Atlantic water mixes with cooler water from the Skagerrak and flows along the Norwegian coast to split up in several directions (Straneo et al. 2013). One part of the current passes Spitsbergen as the Western Spitsbergen current and flows poleward into the Arctic Ocean (Straneo et al. 2013). When the Atlantic water reaches the Lincoln Sea its temperature has decreased, but the temperature of around 0.3 °C at a depth of 300 m, which coincides with the sill depth between the Nares Strait and the Lincoln Sea, is still higher than the -2.2 °C pressure-dependent freezing point at the base of the Petermann ice tongue (de Steur et al. 2013; Münchow et al. 2016). It is this relative warm water that flows over the ~380m deep sill between the Petermann fjord and the Nares Strait (Johnson et al. 2011). The warm Atlantic water remains at depth until it reaches the Petermann glacier at the grounding line where it partly melts the glacier and mixes with the fresh water originating from surface melt (Johnson et al. 2011). The mixture of Atlantic water with glacier ice melt water has a distinct potential temperature – salinity slope of 2.5°C/psu, also known as the Gade line (Johnson et al. 2011; Gade 1979). Water with this distinct mixing slope can be found under the ice tongue at depths of 300 m (Figure 4). (Münchow et al. 2016) speculates that the mixed water rises vertically due to its increased buoyancy and flows towards the mouth of the Petermann fjord. This implies that the majority of basal melt takes place close to the grounding line and diminishes close to the calving front.

The future stability in relation to basal melt will be mostly determined by the ocean circulation within the Petermann fjord and the supply of warm salty Atlantic water to the base of the Petermann ice tongue in combination with turbulent mixing of warm ocean water with fresh runoff from the glacier (Münchow et al. 2016).

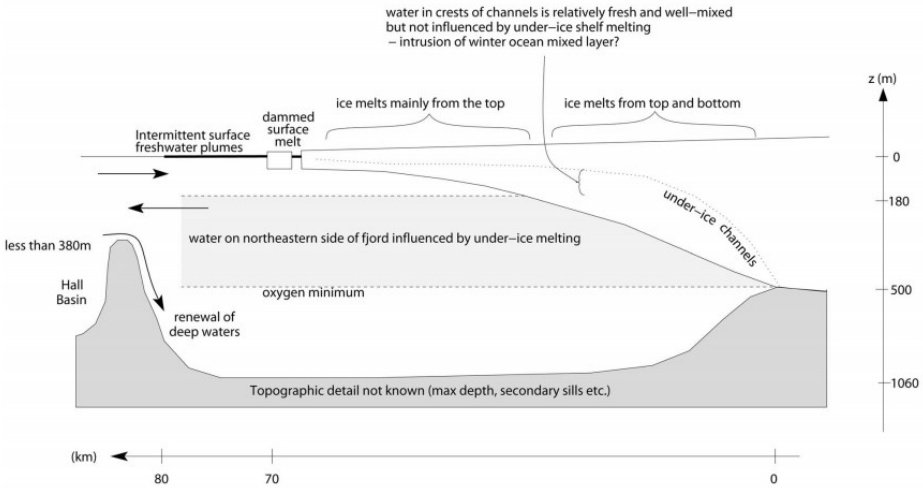

Figure 4 Schematic overview of the Petermann fjord showing the path of the different water layers under the floating ice shelf. Warm deep water flows over the sill and reaches the ice shelf near the grounding line. The melt water flows out of the fjord at intermediate depths (grey zone). Image from Johnson et al. 2011

2.2 Melt rate from ice thickness change

Thickness change of the Petermann glacier is due to three components: the basal mass balance, the SMB and dynamic thinning (Wilson et al. 2017). Dynamic thinning represent the thickness change due to stretching or compression caused by velocity gradients. The basal mass balance represents the thickness change due to basal melt and refreezing. The SMB represents the thickness change due to runoff and snowfall. The principle of conservation of mass is used, as shown in Münchow et al. (2014), to describe the relation between thickness change and melt rates:

$$\frac{\partial I}{\partial t} + I\nabla\vec{u} + \vec{u}\nabla I = \dot{a} + \dot{m} \qquad (1)$$

Where $\frac{\partial I}{\partial t}$ represents the non-steady state thinning, $\vec{u}\nabla I$ the thickness change due to the advection of the gradient, $I\nabla\vec{u}$ the non-linear dynamic thickness change, $\dot{a}$ is the thickness change due to the surface mass balance and $\dot{m}$ the thickness change due to basal melt. According to Münchow et al. (2014) the non-linear dynamic thickness change $\nabla\vec{u}$ is small compared to the other terms and is therefore ignored. A schematic overview of the different terms in equation (1) is given in Figure 5 where a floating ice shelf is depicted at time t=0 in blue and the same ice shelf after a certain amount of time Δt in orange. From Figure 5 it shows that ice thickness I_0 has reduced to I_1 due to three different processes namely: the thickness change over time due to the SMB $\frac{\partial I}{\partial t_{smb}}$, the thickness change over time due to basal melt an refreezing $\frac{\partial I}{\partial t_{basal}}$ and $\vec{u}\nabla I$ where ∇I is depicted as $\frac{\partial I}{\partial y}$. When both the orange and blue thickness is know the thickness change can be calculated in two different ways. The first is in a Eularian framework where the blue and orange thicknesses are compared at the same location. This gives the non-steady state melt rate $\frac{\partial I}{\partial t}$ which shows how the melt rate has changed over the considered time period. The downside of this approach is that the ice sheet is not as smooth as depicted in Figure 5 and any surface or bottom terrain features would introduce errors in the calculated melt rate. This effect is also known as temporal aliasing and described in, among other papers, Wilson et al (2017). The second approach is to use a Lagrangian framework, where the orange ice shelf is shifted back by the velocity $(\vec{u})$ times the time difference Δt in order to compare ice thickness I_1 with I_0. The Lagrangian reference frame thickness comparison will results in the total thickness change and is not influenced by shifting terrain features as the same column of ice is compared.

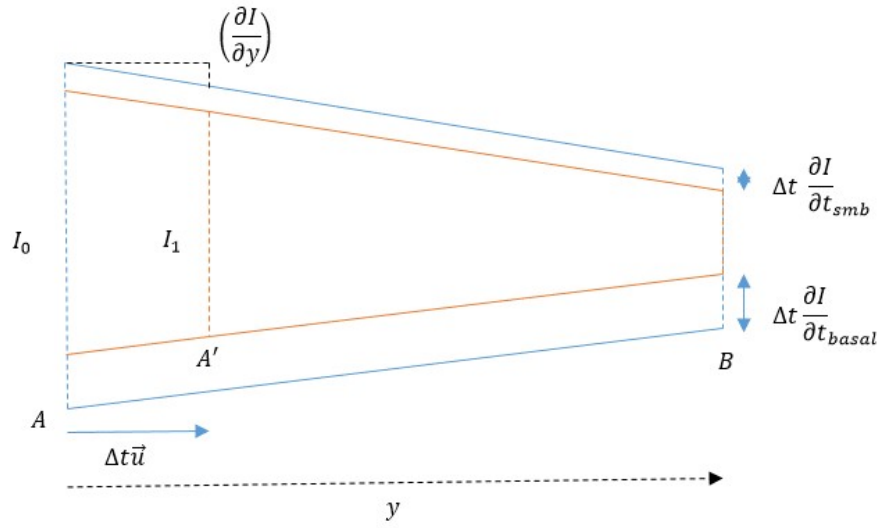

Figure 5 Schematic overview of the three different terms in the mass balance of a floating section of a glacier at time t in blue and t+Δt in orange. At both time steps the glacier is cut-off at point A and B. Change in ice thickness between blue and orange glacier is due to the three terms in the mass balance.

2.3 Introduction to linear elastic fracture mechanics (LEFM)

Crevasses can be seen as large fractures that under the influence of stress propagate to a certain depth, length and width. Nye (1955) was one of the first people to use stress to estimate the depth a vertical crevasse would reach and found that a crevasse in a field of crevasses the maximum depth lies at the point where the tensile stress equals the closing overburden pressure. Weertman (1973) showed that the final depth a crevasse can reach is increased significantly and can even penetrate the entire ice thickness when the crevasse is filled with water. Smith (1976) was the first to use the LEFM theory to calculate the crevasse depth splitting the contribution of stress, overburden pressure and water pressure. Rist et al. (1996), Van der Veen (1998a,b) and Van der Veen (2008) all improved on the method of Smith (1976) by including a depth varying stress, the effect of a finite thickness and an additional mode of fracturing.

2.3.1 Modes of fracturing

The three different modes of fracturing as shown in Figure 6 represent the basics of LEFM on glaciers as any general stress configuration can be expressed using these three modes. Mode 1 represents fracturing due to a tensile normal stress acting perpendicular to the failure plane. Mode 1 is also known as the opening mode as it causes the crack faces to move away from each other. Mode 2, or the sliding mode, causes fracturing when shear stress acts parallel to the failure plane. Mode 3 is the tearing mode and causes fracturing when the shear stress acts perpendicular to the failure plane.
In this thesis only mode 1 fracturing is considered following the approach of Van der Veen (1998b). To compensate for excluding the modes related to shear stress the first principle stress is used, which is the stress configuration where the shear stress equals zero.

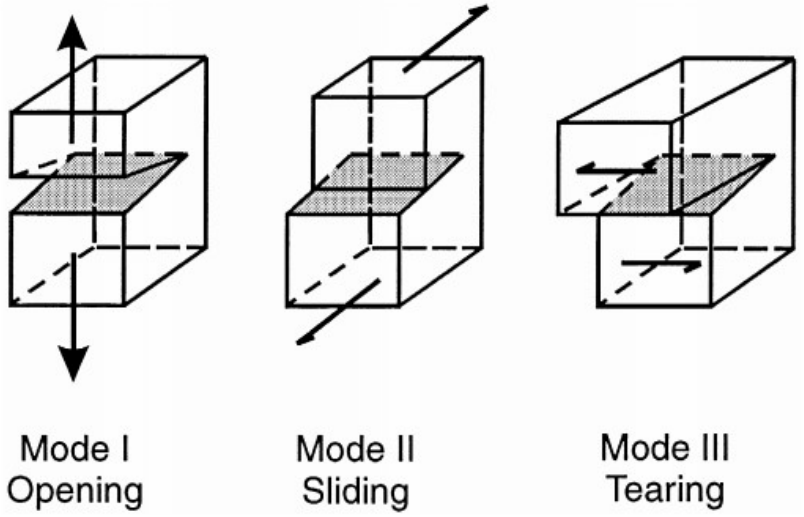

Figure 6 Opening mode (mode 1), Sliding mode (mode 2) and Tearing mode (mode). Image from Van der Veen (1998b)

2.3.2 From velocity to strain to stress

The linear elastic fracture mechanics theory uses stresses to calculate the propagation of crevasses. To obtain the stresses that act on and in a glacier there are two options: the first option is to model the stresses using an ice flow model like ELMER/ICE or Úa (Hill et al. 2018) and the second option is to use flow velocity observations either from satellite or from the field (Mottram (2008), Mottram and Benn (2009) to calculate the strain rates and stresses respectively. Here the way stresses are calculated from the strain rates derived from flow velocity measurements is described.

The strain rate is calculated using the method described in Nye (1959) who states that the strain rate is equal to the velocity gradient and that the strain rate tensor is given by:

$$\begin{bmatrix} \dot{\varepsilon}_{xx} & \dot{\varepsilon}_{xy} \\ \dot{\varepsilon}_{yx} & \dot{\varepsilon}_{yy} \end{bmatrix} = \begin{bmatrix} \dfrac{\partial u}{\partial x} & \dfrac{1}{2}\left(\dfrac{\partial v}{\partial x} + \dfrac{\partial u}{\partial y}\right) \\ \dfrac{1}{2}\left(\dfrac{\partial v}{\partial x} + \dfrac{\partial u}{\partial y}\right) & \dfrac{\partial v}{\partial y} \end{bmatrix} \quad (2)$$

When the strain rates are known they can be used to calculate the principle strain rates. The principle strain rates are needed to calculate the principle stresses and are defined as the strain along the axis where the normal strain rates are maximum and the shear strain is zero. The principle strain rates are calculated using equation (3), (4) and (5) from Nye (1959).

$$\dot{\varepsilon}_1 = \frac{1}{2}\left(\dot{\varepsilon}_{xx} + \dot{\varepsilon}_{yy}\right) + \sqrt{\frac{1}{4}\left(\dot{\varepsilon}_{xx} + \dot{\varepsilon}_{yy}\right)^2 + \dot{\varepsilon}_{xy}} \quad (3)$$

$$\dot{\varepsilon}_3 = \frac{1}{2}\left(\dot{\varepsilon}_{xx} + \dot{\varepsilon}_{yy}\right) - \sqrt{\frac{1}{4}\left(\dot{\varepsilon}_{xx} + \dot{\varepsilon}_{yy}\right)^2 + \dot{\varepsilon}_{xy}} \quad (4)$$

$$\dot{\varepsilon}_2 = -\left(\dot{\varepsilon}_{xx} + \dot{\varepsilon}_{yy}\right) \quad (5)$$

$$\dot{\varepsilon}_{eff} = \sqrt{\frac{1}{2}\left({\dot{\varepsilon}_1}^2 + {\dot{\varepsilon}_2}^2 + {\dot{\varepsilon}_3}^2\right)} \quad (6)$$

According to Van der Veen (1998b) it is not the strain rate but the stress that causes a crevasse to open and in order to calculate the stress from the strain rate the method from Nye (1959) and Glen (1955) is used. Ice behaves as a visco-elastic material, which means that although the ice flows under an applied stress it still shows some internal resistance. To describe the relation between the applied stress and the observed strain Glen (1955) formulated Glen's flow law as follows:

$$\tau_{eff} = \left(\frac{\dot{\varepsilon}_{eff}}{A}\right)^{\frac{1}{n}} \quad (7)$$

The equation describes the relation between the effective strain rate $\left(\dot{\varepsilon}_{eff}\right)$ as calculated in equation (6) and effective shear stress $\left(\tau_{eff}\right)$. In the equation (A) is a measure for the viscosity of the ice and is temperature dependent and (n) is called the flow parameter. (A) is sometimes replaced by (B), also known as the rigidity parameter. The relation between (A) and (B) is:

$$A = B^{-1/n} \quad (8)$$

To get from the effective shear stress to the maximum tensile stress Nye (1959) used the following equation:

$$\sigma_1 = 2\left(\frac{\tau_{eff}}{\dot{\varepsilon}_{eff}}\right)\dot{\varepsilon}_1 + \left(\frac{\tau_{eff}}{\dot{\varepsilon}_{eff}}\right)\dot{\varepsilon}_3 \quad (9)$$

The equation shows that the maximum tensile stress is not only dependent on the maximum tensile strain but also on the minimum tensile strain (or maximum compressive strain). This means that even though the maximum tensile strain is positive the maximum tensile stress can still be negative. This underlines the importance of using stresses instead of strain rates to calculate crevasse depths. The first principle stress (σ_1) is the maximum tensile stress and will be used in the LEFM approach to calculate the theoretical crevasse depth in mode 1 fracturing.

2.3.3 Fracture mechanics

Fracture mechanics is the study of how fractures initiate and propagate. The theory on how fractures initiate is not discussed here as the assumption is made that glaciers contain enough initial flaws (van der Veen 1999). The theory of LEFM was developed by A. A. Griffith, a British engineer in the First World War. Griffith noticed that the tensile stress needed to break the atomic bonds of glass is approximately 100 times higher than the tensile stress required to fracture a glass plate (Griffith 1921). Griffith (1921) hypothesized that microscopic flaws in the glass were the reason for the significant difference in tensile strength. Testing this hypothesis he found that the fracture stress of glass is equal to a constant (C) divided by the square root of the fracture length (a), where $\left(\sigma_{fr}\right)$ is the fracture stress as show in equation (10).

$$\sigma_{fr} = \frac{C}{\sqrt{a}} \quad (10)$$

The constant, Griffith found, can be described in terms of surface energy and strain energy. The amount of energy (R) that is required to create new surface is equal to the energy required to break anatomic bonds (γ) times the length and width of the fracture $(a * B)$ times two as a fracture has two faces:

$$R_{surface} = 2 * \gamma * a * B \quad (11)$$

The strain energy can be derived from the principles of work and energy. Work (W) is a measure of mechanical energy that describes the relation of force (F) times the distance over which the force is applied:

$$W = \int F\,dx \qquad (12)$$

Since the formulation of linear elastic fracture mechanics uses stress instead of force it is convenient to express the work in terms of stress, where stress (σ) is force (F) divided by area (A) and strain (ε) is the change in length (dx) over length (L), the expression becomes:

$$W = \int \frac{F}{A}\frac{dx}{L}V = \int \sigma\, d\varepsilon * V \qquad (13)$$

The work, or strain energy, now can be expressed in stress only by using Hook's law in equation (14), where (E) stands for the modulus of elasticity and (ε) is strain for uniaxial tension:

$$\sigma = E * \varepsilon \qquad (14)$$

Combining equation (13) and (14) gives:

$$W_{str} = \int E\varepsilon\, d\varepsilon * V = \frac{1}{2}E\varepsilon^2 V \qquad (15)$$

$$W_{str} = \frac{\sigma^2}{2E}V \qquad (16)$$

Figure 7 illustrates the reduction of strain energy following the propagation of a fracture. As the fracture increases in length the stress free zone increases as well. The energy release corresponding to this stress free zone is equal to the strain energy per unit volume times the volume the zone:

$$W_r = \frac{\sigma^2}{2E}B\pi a^2 \qquad (17)$$

Combining the fracture free strain energy and the strain energy release rate the expression for the total strain energy as function of fracture length becomes:

$$W_t = \frac{\sigma^2}{2E}V - \frac{\sigma^2}{2E}B\pi a^2 \qquad (18)$$

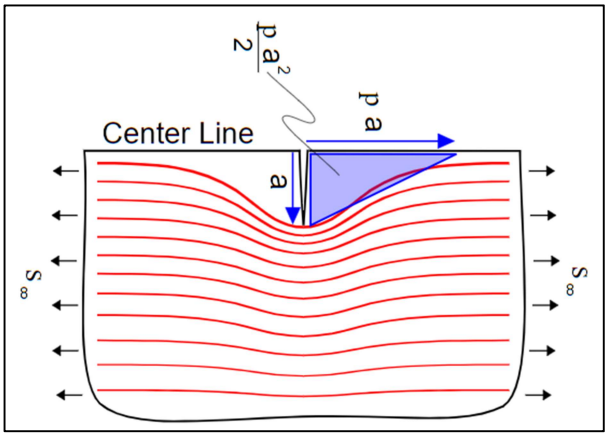

Figure 7 Schematic overview of the increase in stress intensity related to crack growth. Blue area signifies the stress free zone after fracture propagation over distance a. Red lines signifies the "path" of the stress through the object. The densification of the lines near the fracture tip represents the increase in stress intensity. Image from: fracturemechanics.org

With an expression for both the surface energy (11) and the strain energy (18) the total energy of the glass plate becomes:

$$R_t = R_s + W_t \qquad (19)$$

$$R_t = 2 * \gamma * a * B + \frac{\sigma^2}{2E} * V - \frac{\sigma^2}{2E} * B * \pi * a^2 \quad (20)$$

In Figure 8 the relation between total energy, surface energy and the strain energy is shown and demonstrates that for small cracks energy has to be put in the system in order for the fracture to grow, however after a certain point energy is reduced with a growing fracture length. The reduction of total energy with an increasing fracture length means that the fracture can grow spontaneously. The stress at which the fracture transitions from a stable state to an unstable state is called the failure stress and can be calculated by setting the derivative of the total stress to zero.

$$\frac{R_t}{da} = 2\gamma - \frac{\sigma^2}{2E}\pi a = 0 \quad (21)$$

Rewriting equation (21) gives the expression for the failure stress (σ_f):

$$\sigma_f = \sqrt{\frac{2\gamma E}{\pi a}} \quad (22)$$

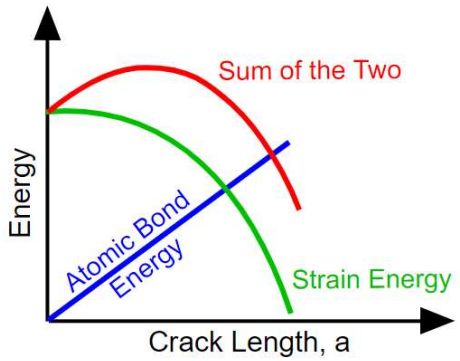

Figure 8 Different energy terms related to crack growth. The atomic bond energy in blue shows that the energy required for the breaking of atomic bonds increases with fracture length. Green shows the release of energy with increasing fracture length. Sum of the two, in red, shows that until a certain point energy is required for further fracture growth and after that energy is released with increasing fracture length. Image from fracturemechanics.org

In the above expression the assumption is made that stress act in only one direction and perpendicular to the fracture orientation. The expression from Griffith (1920) takes the form:

$$\sigma_f = \sqrt{\frac{2\gamma E}{\pi a \vartheta}} \quad (23)$$

For plane stress and:

$$\sigma_f = 2\sqrt{\frac{\gamma \mu}{\pi a \vartheta}} \quad (24)$$

For plane strain, with (ϑ) as the Poisson's ratio and (μ) as the modulus of rigidity and differs from the equation (22) as it includes equibiaxial tension. The formulation of Griffith describes the stability of fracture propagation and is only applicable to very brittle materials such as glass or ceramics. For metals the theory vastly underestimated the critical stress due to the presence of plastic deformation at the fracture tip, a process that increases the energy required to increase the crack length.

It was Irwin (1957) who found a way to account for the non-elastic deformation at the fracture tip and modified the theory of Griffith. Irwin (1957) described the stress state at the fracture tip and named it the stress intensity factor (SIF). The stress intensity factor is now used in almost all applications involving fracture mechanics and is one of its most fundamental parameters. Irwin (1957)

based his theory on Westergaard's (1939) solution of the stress state in a plate containing a crack. For a mode 1 fracture Irwin's formulation of the stress near the crack tip is:

$$\sigma_{xx} = \frac{\sigma_\infty \sqrt{\pi a}}{\sqrt{2\pi r}} f_{xx}(\theta) \quad (25)$$

$$\sigma_{yy} = \frac{\sigma_\infty \sqrt{\pi a}}{\sqrt{2\pi r}} f_{yy}(\theta) \quad (26)$$

$$\tau_{xy} = \frac{\sigma_\infty \sqrt{\pi a}}{\sqrt{2\pi r}} f_{xy}(\theta) \quad (27)$$

From equation (25), (26) and (27) the stress (σ) at any location in the plate at a radius (r) and angle (θ) can be calculated based on the length of the crack (a) and the far field stress (σ_∞).
Note that all three formulas contain the same $\sigma_\infty \sqrt{\pi a}$ term. Irwin (1957) defined this term as the stress intensity factor (K). To account for different crack geometries the stress intensity factor is often expressed including a geometry factor as well:

$$K = f\sigma\sqrt{\pi a} \quad (28)$$

Where (f) is only dependent on the geometry of the crack, f =1 for a central crack in an infinite plate. The stress intensity factor is linked to the energy release rate in the following way:

$$K = \sqrt{GE} \quad (29)$$

$$G = 2(\gamma_b + \gamma_{bp}) \quad (30)$$

(G) is known as the energy release rate and includes now the molecular bond energy as well as a term that represents the energy needed for plastic deformation introduced by Irwin (1947). As for the critical energy release rate the critical stress intensity factor is the value at which the fracture propagation becomes unstable. The critical stress intensity factor is also known as the fracture toughness, which is a material specific property. This relative straightforward way to calculate the combination of stress and fracture length where the fracture propagation becomes unstable is what makes the stress intensity factor such an attractive tool.

2.3.4 Linear elastic fracture mechanics applied to glaciers

The theory above describes the situation where the stress is uniform over the entire fracture length. This means that once a fracture reaches a critical length the propagation becomes unstable and unstoppable. For glaciers the assumption that the stress is uniform over the entire fracture length is not valid, this is especially true when looking in the vertical direction. The non-uniformity of the stress state means that initially the fracture propagation can be unstable and become stable again after reaching a certain length. Van der Veen (1998) used the stress intensity theory from Irwin (1957) to describe the stress state at the tip of a crevasse to calculate at which depth a fracture becomes stable. By doing so he could calculate the depth a crevasse would reach under certain circumstances. Mottram and Benn (2009) showed that the stress intensity approach performed better than the models of Nye (1955) and Weertman (1973) provided that the parameters were correctly tuned. Here a description of the stress intensity method for calculating crevasses depths is given as well as the relative importance of the different tuning parameters.

First the vertical propagation of fractures on ice shelfs for mode 1 fracturing is discussed. A schematic overview is given in Figure 9. There are several different contributors to the stress state at the tip of a fracture that play a role in its propagation. Firstly there is the tensile stress due to velocity gradients on the ice shelf. The tensile stress is considered to be uniform over the entire thickness of the ice. There are some situations in which this assumption is not valid, especially when the top layer consists of snow and firn as Rist et al. (1996) showed. For the Petermann glacier, especially in the summer, there is no snow or firn layer present (Dow et al. 2018) which makes the uniform stress over ice thickness valid.

Secondly there is the overburden pressure of the ice itself, also called the lithostatic pressure, it provides a resistive pressure to the propagation of a crevasse (Van der Veen 1998). As the depth of the crevasse becomes larger the lithostatic pressure becomes larger as well and since the tensile stress is considered uniform at a certain depth the tensile stress and lithostatic pressure will cancel out at a certain depth below the surface. It is the lithostatic pressure that prohibits unstable fracture propagation all the way down the bottom of the ice shelf.

The third contribution is the pressure due to the presence of water in the crevasse. When a crevasse fills up with water the hydrostatic pressure of the water acts to open the fracture and promotes further propagation. The water pressure can have a big influence on the final depth a crevasse can reach according to Van der Veen (1998), this will be confirmed again in the next section where the relative importance of the different stress contributions is discussed.

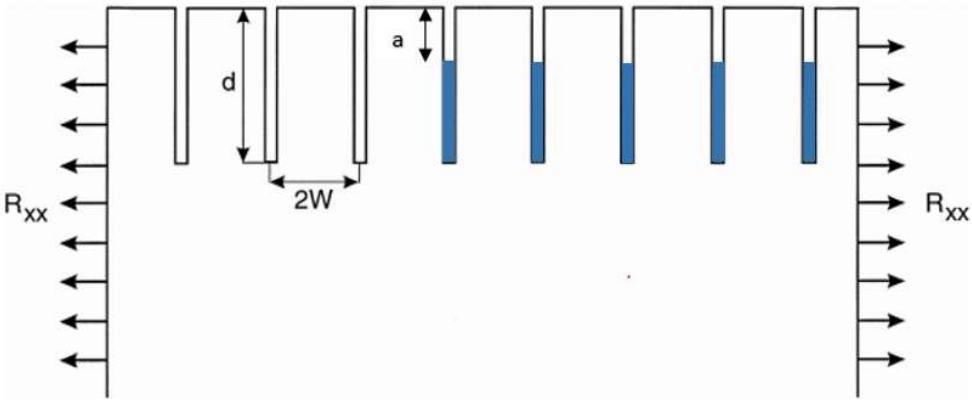

Figure 9 Schematic overview of crevasses in an ice shelf. Where d: depth of crevasse, a: water level below surface, w: half width between crevasses, Rxx: tensile stress. Image edited from Van der Veen (1998).

Van der Veen (1998) used the stress intensity factor theory to describe the stress state at the crevasse tip. The formula for the stress intensity factor is given by equation (28). The total SIF at the tip of a crevasse is the sum of the SIFs due to tensile stress (K_1^1), over burden pressure (K_1^2) and water pressure (K_1^3) (Van der Veen 1998) and is shown in equation (31). Crevasse propagation continues while the total SIF is lower than the fracture toughness. In the following figures a fracture toughness of 100 kPa $m^{1/2}$ is used, which is the average of typical fracture toughness values for ice (Petrovic 2003).

$$K_1^{total} = K_1^1 + K_1^2 + K_1^3 \quad (31)$$

Here the different geometry factors are discussed for the three different stresses acting on the crevasse. The SIF as a result of the tensile stress is given by:

$$K_1^1 = F(\lambda)\sigma\sqrt{\pi d} \quad (32)$$

With the fracture geometry parameter is determined by fitting a polynomial through finite element model output and is defined as:

$$F(\lambda) = 1.12 - 0.23\lambda + 10.55\lambda^2 - 21.72\lambda^3 + 30.39\lambda^4 \quad (33)$$

$$\lambda = \frac{d}{I} \quad (34)$$

This geometry factor is dependent on the ratio of fracture length (d) to the ice thickness (I). This relation means that the stress intensity increases with increasing fracture length through the standard relation of equation (32) and that this increase becomes stronger when the ratio of crevasse depth to ice thickness approaches one. This effect is illustrated in Figure 10 where the SIF as function of crevasse depth is plotted for several different ice thicknesses. The effect of the ratio of crevasse depth and ice thickness also means that for a thinner ice shelf this effect influences the crevasse propagation even for relative small crevasse depths.

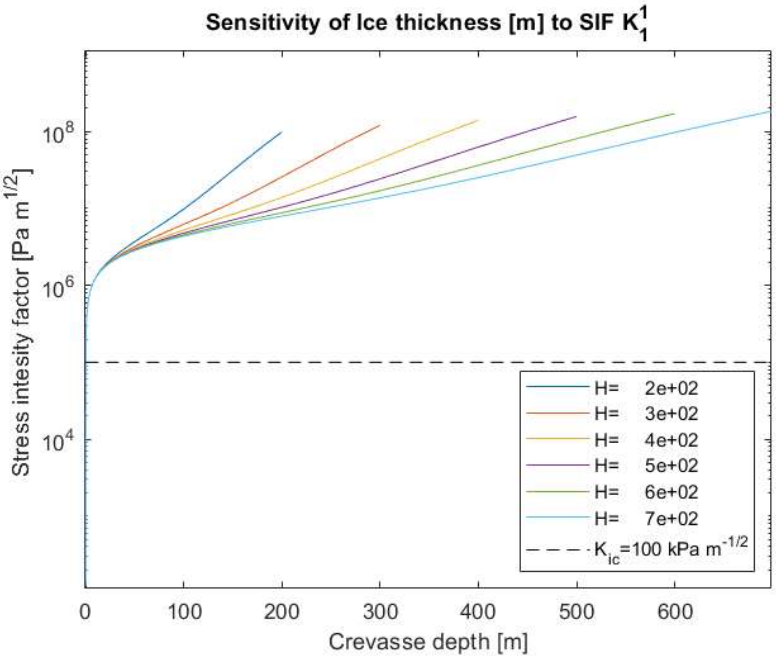

Figure 10 Sensitivity of the ice thickness to the SIF. The fracture toughness is plotted as dotted line.

The geometry factor for the tensile stress is only valid for a single crevasse. The spacing between consecutive crevasses is important because when the spacing between crevasses is relatively small the stress concentration at the crevasse tip is reduced (Veen 1998; Mottram and Benn 2009).
The new geometry factor that takes the crevasse spacing into account is:

$$D(S) = \frac{1}{\sqrt{\pi}}\left[1 + \frac{1}{2}S + \frac{3}{8}S^2 + \frac{5}{16}S^3 + \frac{35}{128}S^4 + \frac{63}{256}S^5 + \frac{231}{1024}S^6\right] + 22.501S^7 - 63.502S^8 + 58.045S^9 - 17.577S^{10} \quad (35)$$

$$S = \frac{W}{W + d} \quad (36)$$

The expression of the stress intensity factor due to tensile stress becomes:

$$K_1^1 = D(S)\sigma\sqrt{\pi dS} \quad (37)$$

The new geometry factor is dependent on the crevasse spacing half width (W) and the crevasse depth (d). The drawback of this geometry factor is that it does not account for the ratio of crevasse depth over ice thickness. For crevasses that are spaced far apart the factor becomes 1.12 which is the same value the factor (F) has for shallow crevasses from equation (33). The consequence is that the

influence of multiple crevasses on the maximum crevasse depth can only be taken into account for shallow crevasses ($d < 0.2I$). The sensitivity of the crevasse spacing to the SIF is shown in Figure 11. The figure shows the difference between a single crevasse (infinite spacing) and crevasses with finite spacing. The single crevasse has the highest SIF and the lowest SIF corresponds to the smallest spacing. The SIF is plotted up to a depth of 100 m, with an ice thickness of 500 m this falls within the shallow crevasse criterion.

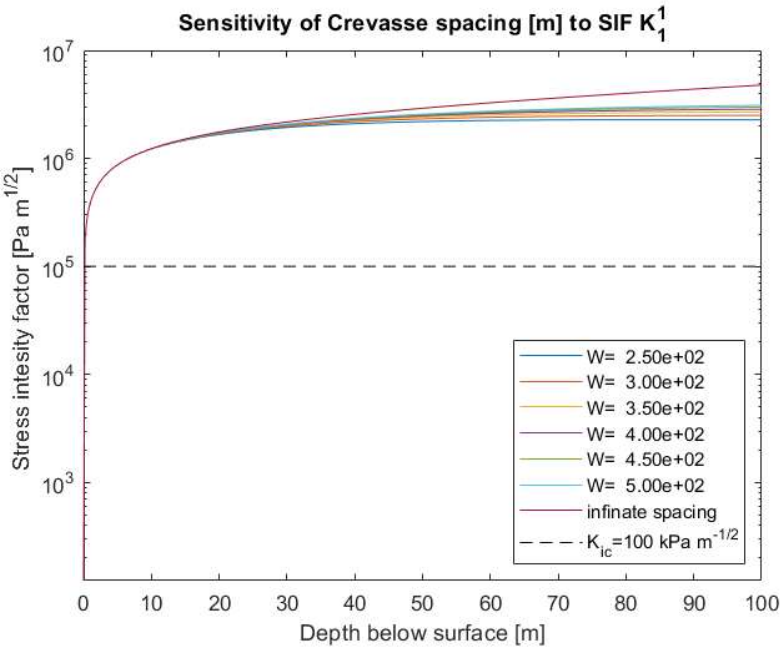

Figure 11 Sensitivity of the crevasse spacing to the SIF. The fracture toughness is plotted as dotted line.

The SIF as a result of the lithostatic pressure is slightly more complex compared to the SIF of the tensile stress. This is due to the linear increase in lithostatic stress with depth. The SIF of the lithostatic stress at the crevasse tip is calculated by integrating the SIF along the crevasse depth:

$$K_1^{(2)} = \int_0^d dK_1^{(2)} \tag{38}$$

$$dK_1^{(2)} = \frac{2\sigma_l(b)db}{\sqrt{\pi d}} G(\gamma, \lambda) \tag{39}$$

$$G(\gamma,\lambda) = \frac{3.52(1-\gamma)}{(1-\lambda)^{3/2}} - 4.35 - \frac{5.28\gamma}{(1-\lambda)^{\frac{1}{2}}} + \left[1.30 - \frac{0.30\gamma^{\frac{3}{2}}}{(1-\gamma^2)^{\frac{1}{2}}} + 0.83 - 1.76\gamma\right][1-(1-\gamma)\lambda] \tag{40}$$

$$\sigma_l(b) = -\rho g b \tag{41}$$

Where b is the depth below the surface and ranges from 0 to the crevasse depth (d). (λ) is again the ratio of crevasse depth over ice thickness and (γ) the ratio of depth below the surface over crevasse depth. The dependence of the lithostatic pressure SIF on the ratio of crevasse depth over ice thickness means that as with the SIF due to tensile stress, for a single crevasse, the SIF increases as the ratio approaches one. By including the contribution of the tensile stress as well as the lithostatic pressure in the calculation of the SIF, the total SIF eventually falls below the fracture toughness marking the

end of the unstable propagation as shown in Figure 12. Since the SIF due to the lithostatic pressure is dependent on the ratio of crevasse depth over ice thickness and the SIF due to tensile stress is not dependent, when using the formulation including crevasse spacing, on this ratio the thinnest ice sheet will also give the smallest crevasse.

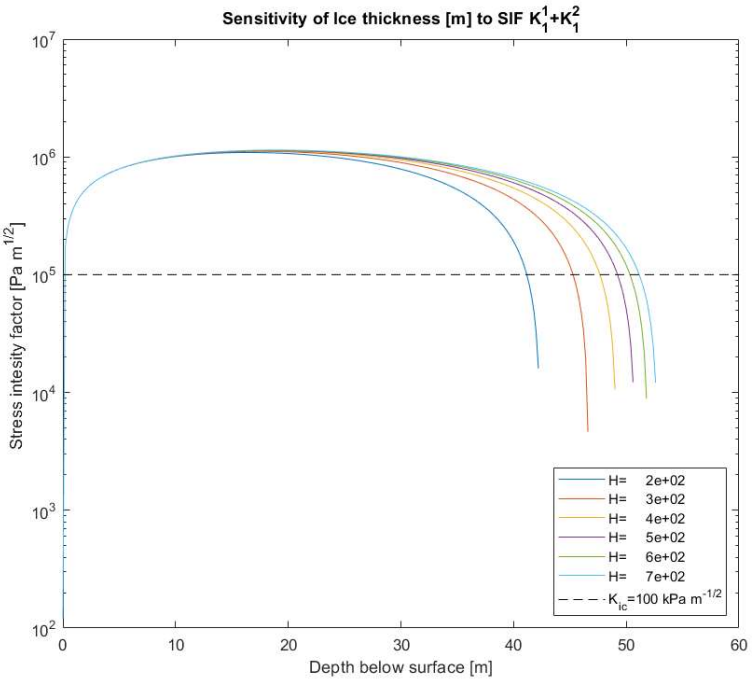

Figure 12 Sensitivity of the ice thickness to the SIF as function of the tensile stress and lithostatic pressure. For the SIF due to tensile stress the formulation including the crevasse spacing is used. The fracture toughness is plotted as dotted line.

The third contribution to the total stress intensity at a fracture tip is due to water pressure. The water pressure is similar as lithostatic pressure with the only difference is that it acts to open the crevasse instead of closing it. The SIF due to water in the crevasse is:

$$K_1^{(3)} = \int_0^d dK_1^{(3)} \quad (42)$$

$$dK_1^{(3)} = \frac{2\sigma_w(b)db}{\sqrt{\pi d}} G(\gamma, \lambda) \quad (43)$$

$$\sigma_w(b) = \rho_w g(b-a) \quad (44)$$

With (b) the depth below the surface, $(\sigma_w(b))$ the depth dependent hydrostatic pressure, and (a) the water level defined as the depth below the surface where water is present. The water only starts to influence the total SIF at a depth greater than (a) (shown in Figure 9). Similar to the other SIF components the water pressure SIF is dependent on the ratio of crevasse depth over ice thickness. This means that the water pressure SIF gets higher as the crevasse gets deeper due to the increase in water pressure and the effect of the depth-thickness ratio. In Figure 13 this effect is demonstrated as the combined SIF of the tensile stress, lithostatic pressure and water pressure is plotted for a single crevasse (infinite spacing) as well as for a field of crevasses with different spacing. The water level in the crevasse is set to be 10 m below the surface in the left two figures and in the two figures on the right the water level is set to be 20m below the surface. The main difference between the top left and right figure is that a higher water level can mean the difference between a crevasse that propagates the entire thickness and a crevasse that remains relative shallow.

a)

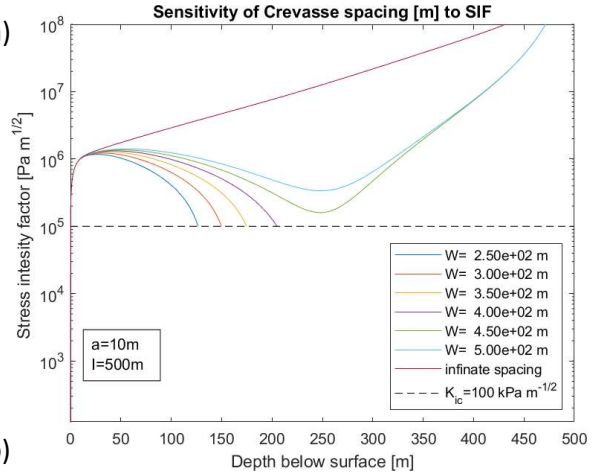
Sensitivity of Crevasse spacing [m] to SIF
Stress intesity factor [Pa m^1/2]
Depth below surface [m]
W= 2.50e+02 m
W= 3.00e+02 m
W= 3.50e+02 m
W= 4.00e+02 m
W= 4.50e+02 m
W= 5.00e+02 m
infinate spacing
K_ic=100 kPa m^-1/2
a=10m
l=500m

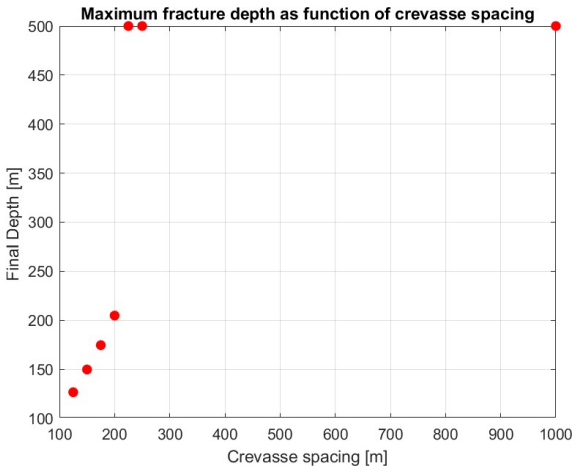
Maximum fracture depth as function of crevasse spacing
Final Depth [m]
Crevasse spacing [m]

b)

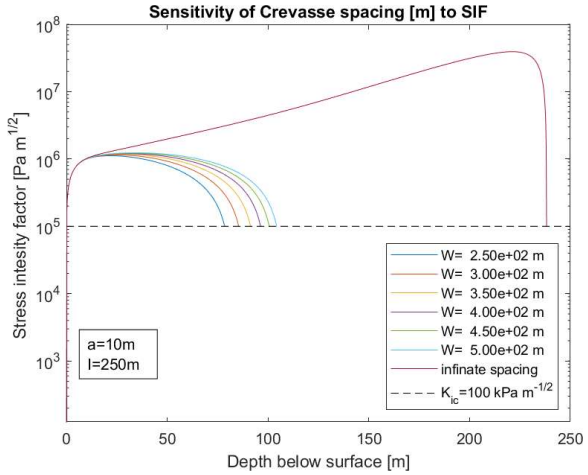
Sensitivity of Crevasse spacing [m] to SIF
Stress intesity factor [Pa m^1/2]
Depth below surface [m]
W= 2.50e+02 m
W= 3.00e+02 m
W= 3.50e+02 m
W= 4.00e+02 m
W= 4.50e+02 m
W= 5.00e+02 m
infinate spacing
K_ic=100 kPa m^-1/2
a=10m
l=250m

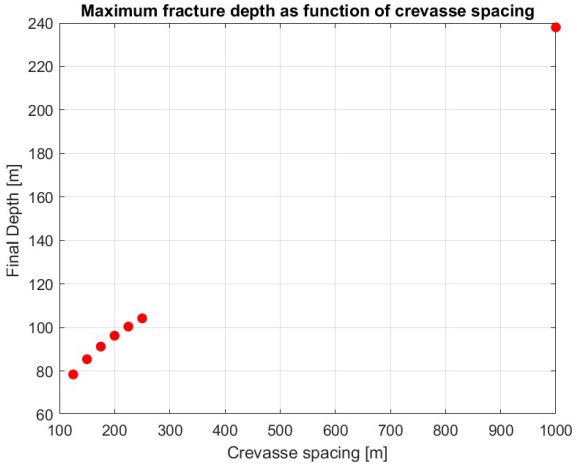
Maximum fracture depth as function of crevasse spacing
Final Depth [m]
Crevasse spacing [m]

c)

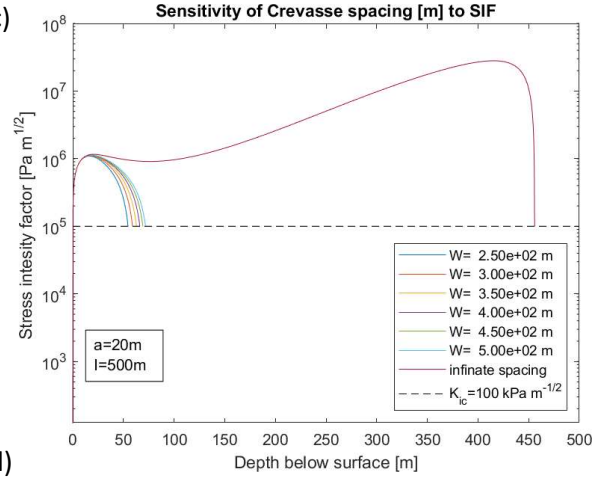
Sensitivity of Crevasse spacing [m] to SIF
Stress intesity factor [Pa m^1/2]
Depth below surface [m]
W= 2.50e+02 m
W= 3.00e+02 m
W= 3.50e+02 m
W= 4.00e+02 m
W= 4.50e+02 m
W= 5.00e+02 m
infinate spacing
K_ic=100 kPa m^-1/2
a=20m
l=500m

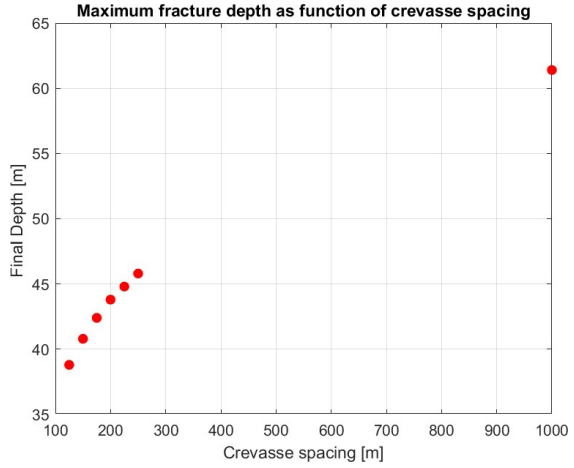
Maximum fracture depth as function of crevasse spacing
Final Depth [m]
Crevasse spacing [m]

d)

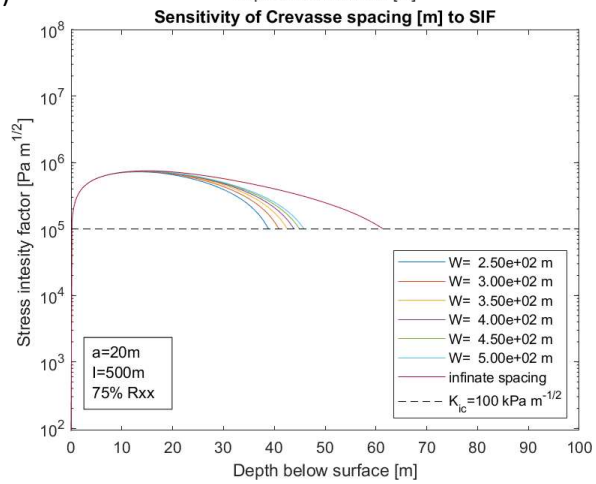
Sensitivity of Crevasse spacing [m] to SIF
Stress intesity factor [Pa m^1/2]
Depth below surface [m]
W= 2.50e+02 m
W= 3.00e+02 m
W= 3.50e+02 m
W= 4.00e+02 m
W= 4.50e+02 m
W= 5.00e+02 m
infinate spacing
K_ic=100 kPa m^-1/2
a=20m
l=500m
75% Rxx

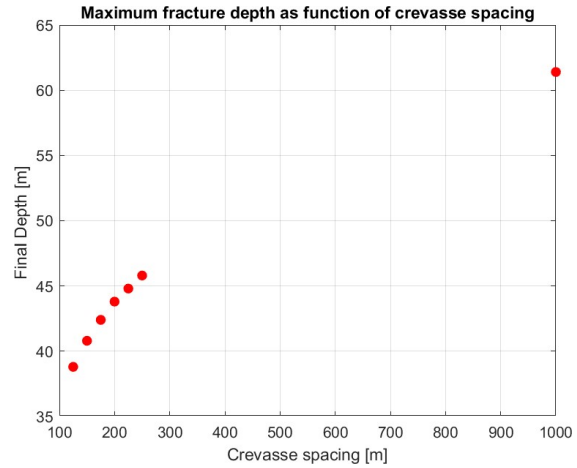
Maximum fracture depth as function of crevasse spacing
Final Depth [m]
Crevasse spacing [m]

Figure 13 Stress intensity plots as function of crevasse depth on the left. SIF is cut off once the fracture toughness is reached. Final crevasse depth on the right. Final crevasse depth corresponds to the depth where the fracture toughness is reached.
a: Sensitivity of crevasse spacing to the SIF with ice thickness: 500m and water level 10m below the surface.
b: Sensitivity of crevasse spacing to the SIF with ice thickness: 250m and water level 10m below the surface.
c: Sensitivity of crevasse spacing to the SIF with ice thickness: 500m and water level 20m below the surface.
d: Sensitivity of crevasse spacing to the SIF with ice thickness: 500m and water level 20m below the surface with 75% of the applied stress.

In Figure 13 four different scenarios are used to plot the SIF as function of depth for different values of crevasse spacing with the maximum depth the crevasse reaches as function of the crevasse spacing where the infinite crevasse spacing is set to 1000m on the left. In figure (a) and (c) the water level varies and shows that a crevasse spacing between infinite and 250m can mean the difference between a relative shallow crevasse and a crevasse that penetrates the entire ice thickness. The ice thickness varies between figure (a) and (b) with an ice thickness of 500 m for figure (a) and 250 m for figure (b). It shows that for a thinner ice shelf the propagation depth is considerably less than for a thicker ice shelf. It has to be noted that for figure (a) the condition of shallow crevasses is violated and that the SIF beyond a 100 m below the surface gives an underestimation of the SIF and most likely the crevasses propagate through the entire ice thickness for all values of the crevasse spacing. To show the influence of the stress on the maximum crevasse depth in figure (d) the same situation as in figure (c) is depicted with the only difference that the stress is 75% of the stress applied in the other scenarios. It shows that for a lower stress amount even the single crevasse does not propagate the entire thickness of the ice.

From the sensitivity analysis a few important conclusions can be made:

1. The single crevasse overestimates the SIF for shallow crevasses in case of a crevasse field, but the crevasse field SIF underestimates the SIF for crevasses with a crevasse depth over ice thickness ratio larger than 0.2.
2. A smaller ice thickness leads to more shallow crevasses compared to a relative large ice thickness. This is due to the relation between the ratio of crevasse depth to ice thickness and the lithostatic SIF.
3. The stress mainly plays a role in the initial part of crevasse propagation. If the stress is high enough to let the crevasse propagate to a depth where there is water present than the propagation can continue otherwise the propagation stops.

The depth at which water is available for crevasse propagation can mean the difference between a shallow crevasse and a crevasse that propagates the entire thickness of the ice shelf.

3. Data

The data sets used in this thesis are divided in four general sections. The first section contains the data used to describe the temperature evolution and surface melt processes on the Petermann glacier. Secondly the datasets are discussed that describe the surface elevation and bottom draft from two different sources: Ice penetrating radar and optical satellite images. This includes the data sources that provide the necessary corrections and transformations to reference the surface elevation to the water level in the Petermann fjord. Thirdly the spatial and temporal coverage of two different flow velocity data sets used are shown. Lastly the satellite images used to identify and track the propagation of the fractures and rifts are discussed.

3.1 Atmospheric data and regional climate model output

In order to assess the evolution of temperature over the Petermann glacier three sources of data have been used. The first source is temperature data from Canadian weather station Alert. Alert has the longest temperature record of the region going back to 1957 and is located 200 km to the North of the Petermann glacier on the northern coast of Ellesmere Island (Figure 14). The near surface air temperature data from Alert was downloaded from the National climate data enter archives at www.ncdc.noaa.gov. The Alert temperature record contains a data gap between August 1971 and January 1998. The second data set is the temperature product from the regional climate model HIRHAM5 with a resolution of ~5.5 km as described in Langen et al. (2015). The HIRHAM5 temperature product provides an uninterrupted record between January 1980 and January 2017 over the Petermann glacier and is provided by the Danish Meteorological Institute. The third data set is the near surface temperature from an automatic weather station (AWS) on the Petermann glacier at the location shown in Figure 14. Temperature measurements from the AWS are available between June 2002 and June 2006 provided through the measuring campaign of K. Steffen et al. (1996) and have a precision of 0.10 °C.

To describe the surface melt process the surface runoff and surface mass balance (SMB) products from the HIRHAM5 model coupled with a MODIS albedo product as described in Langen et al. (2017) was used. Both the runoff and SMB have a spatial resolution of ~5.5 km.

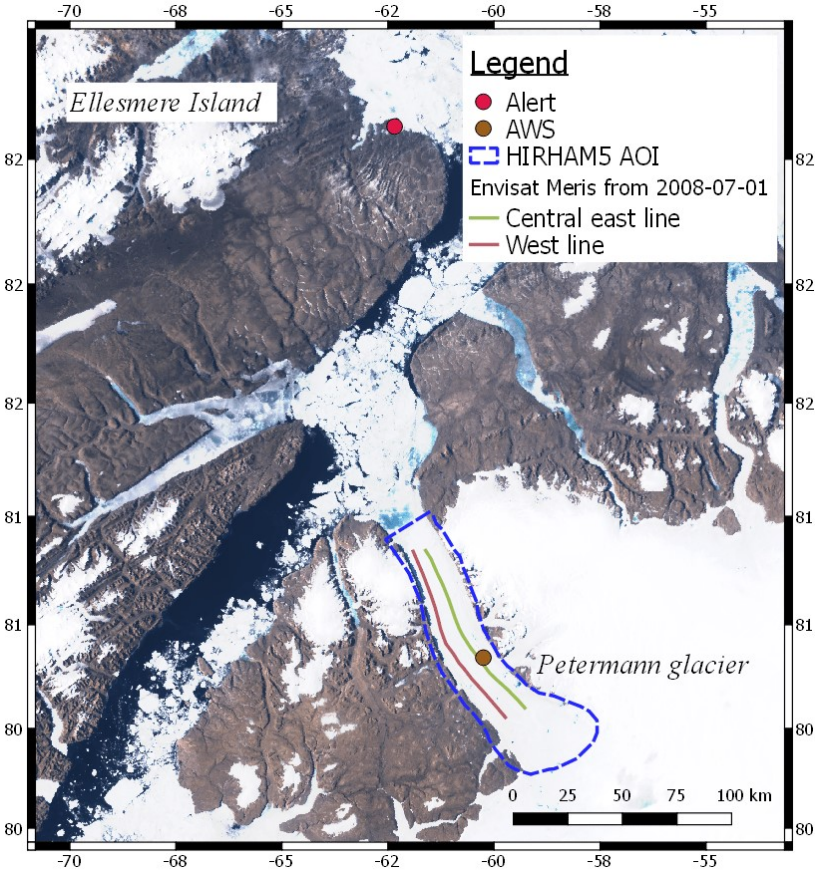

Figure 14 ENVISAT Meris image of NW-Greenland and Ellesmere Island containing the locations of the Alert weather station, the automatic weather station and the AOI over the Petermann glacier. Green and purple lines show the flight paths of the PIB/OIB data set.

3.2 Surface elevation and bottom draft

3.2.1 Operation (pre-) IceBridge

To assess the ice thickness and change in ice thickness over time data from the Pre-IceBridge and Operation Ice Bridge measurement campaigns have been used. Over the Petermann glacier there have been extensive airborne measuring campaigns between June-1992 and September-2007 under the project Pre-IceBridge (PIB) (Allen 2011) and between October-2002 and December-2017 under the name Operation Ice Bridge (OIB) (Allen 2010). The data is available from NASA's National Snow and Ice Data Centre (NSIDC) website. Both PIB as well as the OIB used the Multichannel Coherent Radar Depth Sounder (MCoRDS) which transmits radar signals with different frequencies over a bandwidth of 10 MHz (Shi et al. 2010). The OIB data has an uncertainty of 4.5 m, along track resolution of ~25 m and sample spacing of 14 m. The PIB range resolution is not specified, but since the same type of instrument is used similar specifications are assumed.

Radar signals partially reflect when they enter a new medium, for instance due to a transition from air to ice at the surface of the glacier and from ice to water at the bottom of the glacier. Measuring the two way travel time of these reflected radar signals allows for the calculation of the distance between the aircraft and the surface and bottom respectively. In order to identify which reflection corresponds to the locations of the surface and bottom of the glacier the distances are first converted to heights relative to the WGS-84 reference ellipsoid and then plotted together with the strength of the reflected signal in an echogram. In the top panel of Figure 15 an example of an echogram, showing the calculated distances based on the travel time and the strength of the reflected signal, is shown. From the echograms the surface and bottom profiles are identified based on the strength of the reflected signal as shown in the bottom panel of Figure 15. When the surface and bottom profiles are know the thickness of the ice shelf can be calculated by taking the difference between the surface and bottom height. The quality of the data was assessed by using the quality measure provided with the data. Due to heavily crevassed areas the radar signal can be reflected multiple times resulting in a longer travel time and therefore appearing to be further away. Every measurement point comes with a quality measure, ranging from 1 to 3, where 1 indicates a high confidence the measurement is accurate and 3 indicates a low confidence. Data with a low quality is disregarded and only data with a quality measure of 1 or 2 is used. The OIB and PIB data used along flightpaths of Figure 14 over the Petermann glacier is shown in Table 1.

West	Central East
28/05/2002 (PIB)	28/05/2002 (PIB)
07/05/2011 (OIB)	07/05/2011 (OIB)
05/05/2014 (OIB)	20/04/2013 (OIB)
14/04/2017 (OIB)	14/04/2017 (OIB)

Table 1 OIB and PIB Acquisition dates of the surface and bottom elevation profiles over the Petermann glacier per flight line.

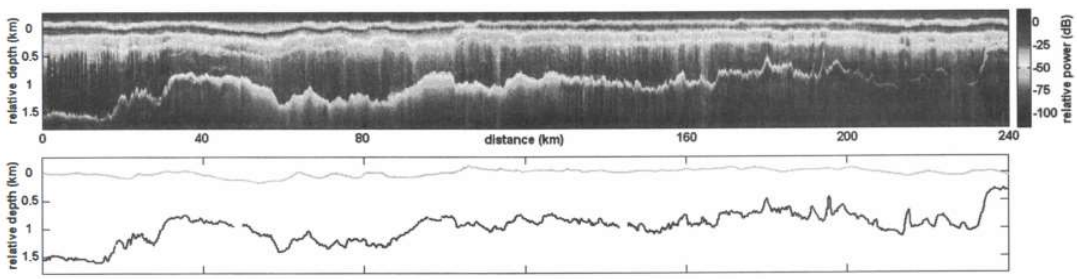

Figure 15 Top panel: OIB radar echogram example of the Thwaites glacier (Antarctica) showing the power of the return signal relative to the send signal along the depth relative to the WGS-84 ellipsoid. Bottom panel: surface profile in grey and bottom profile in b

3.2.2 ArcticDEM

In order to make surface elevation maps of the Petermann glacier several Digital Elevation Model (DEM) strips are combined provided by the ArcticDem program of the University of Minnesota (Porter et al. 2018) to create a 2011 and 2017 DEM. The DEM strips contain surface elevation data of the Petermann's floating ice shelf on a 2 m x 2 m grid and are referenced to the WGS-84 ellipsoid. The specific DEM strips used for each DEM are shown in Table 2 with the file name convention: Sensor_Date_Image1_Image2__segment_Resolution_Version.

The 2011 and 2017 images are from the WorldView-1 (WV01) and Worldview-2 (WV02) satellites both of which fly in a sun-synchronised orbit (SSO) meaning they pass over any point on earth at the same local time. For WVO1 the overpass time is 10:20 AM local time and for WVO2 the overpass time is 10:30 AM local time. The surface elevation data of a single DEM strip is calculated from a pair of high spatial resolution (~0.50 m) panchromatic (optical) images (Image1 and Image2 in the name convention) showing the same area from different angles. The surface elevation is then calculated using a photogrammetry technique. For a more extensive explanation on the (automated) process of extracting surface elevation from optical images the reader is referred to Noh and Howat (2017). Each DEM strip is provided with a zxy-offset based on IceSAT altimetry data which is not yet applied by default.

2011 DEM strip file:	zxy-Offset [m]	2017 DEM strip file:	zxy-Offset [m]
WV02_20110611_103001000BBD3F00_103001000B71F500_seg1_2m_v3.0	2.926 -3.489 -1.110	WV01_20170716_1020010062418B00_102001006407A000_seg1_2m_v3.0	1.061 0.519 1.923
WV02_20110611_103001000BD86D00_103001000B9F0B00_seg1_2m_v3.0	2.993 -3.441 2.042	WV01_20170720_10200100606F7E00_1020010064615F00_seg1_2m_v3.0	1.130 0.755 -0.662
WV02_20110612_103001000B966D00_103001000A493A00_seg1_2m_v3.0	2.891 -1.392 0.341	WV01_20170720_10200100649CBF00_1020010061A7BD00_seg1_2m_v3.0	1.398 0.080 -1.612

Table 2 DEM strips used for the 2011 and 2017 DEM's from the ArcticDEM project of the University of Minnesota with file name convention: Sensor_Date_Image1_Image2__segment_Resolution_Version with its respective IceSAT zxy-offsets in metres.

3.2.3 Earth Gravity Model

In order to calculate ice thickness from surface elevation, using the principle of Archimedes, the ArcticDEM height above the WGS-84 reference ellipsoid was converted to height above mean sea level using pre-calculated geoid heights from the Earth Gravity Model 2008 (EGM2008). EGM2008 provides tide free height differences between the WGS-84 ellipsoid and the geoid. The geoid heights are made publicly available by the U.S. National Geospatial-Intelligence (NGA) agency. The data is provided with a spatial resolution of 1x1-minute (1 minute equals 1.86 km at 80° Latitude). The EGM2008 model has been used in earlier work by both Münchow et al (2014) and Rückamp et al. (2019) to convert ellipsoidal height to height above mean sea level.

3.2.4 Tide Model

In order to correct the ArcticDEM surface elevation for the influence of the tide the Tidal Model Driver package developed by Earth & Space Research (ERS) from Egbert and Erofeeva (2002) was used. The Tidal Model Driver uses the Arctic Ocean Tidal Inversion Model 5 (AOTIM-5) from Egbert and Erofeeva (2002). Both Münchow et al (2014) and Rückamp et al. (2019) used the AOTIM-5 model to correct for tide induced variations in the surface elevation of the Petermann floating ice shelf. Münchow et al.

(2014) speculates that the spatial variation of the tide within the fjord is <0.1 m based on Reeh et al. (2000) who calculated the tidal variation under the 60 km long floating ice shelf of the Nioghalvfjerdsfrorden glacier in northern Greenland. The computed tide can therefore considered to be constant along the entire floating ice shelf of the Petermann glacier.

3.3 Velocity data

In order to analyze the flow velocity of the Petermann glacier and calculate the stresses acting on the glacier two different datasets containing velocity data of the Petermann glacier have been used. Between August 1991 and May 2010 velocity data is provided through the ESA CCI program. The ESA CCI velocity maps of the floating ice shelf are derived from ERS-1/2 and ENVISAT SAR intensity tracking and projected on a 500 by 500 m grid. Each velocity map is derived from two consecutive images with the difference between images ranging from 1 to 35 days with acquisition date as the average of the two images. The acquisition dates and the corresponding time difference between the images from August 1991 until May 2010 are shown in Figure 16. Provided by ENVEO the velocity data between January 2015 and July 2018 is derived from Sentinel-1 feature tracking and projected on a 250 by 250 m grid. Every measurement point is obtained by dividing the distance certain features have travelled by the time difference between two consecutive images (image repeat cycle). The image availability and image pair's repeat cycle is shown in Figure 16 between January 2015 and July 2018.

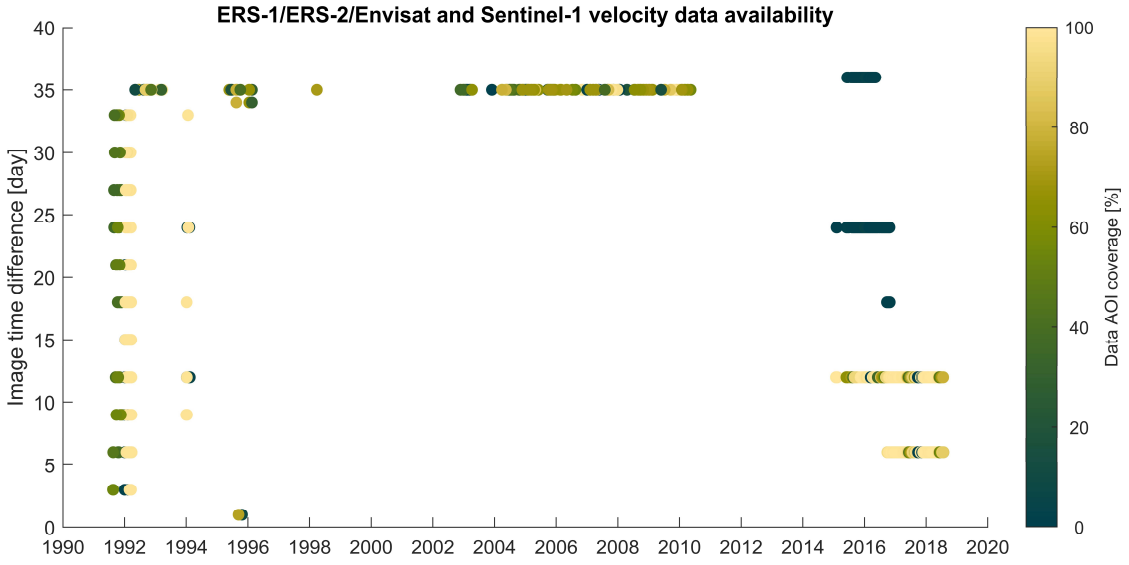

Figure 16 Figure 2 Velocity data availability and corresponding time difference between images used for intensity/feature tracking. Colour of the dots represent the spatial coverage of Petermann's floating ice shelf. ERS-1/ERS-2/ENVISAT ranges from Aug-1991 to May-2010, Sentinel-1 ranges from Jan-2015 till July-2018.

3.4 Fracture tracking data

In order to identify the fractures and large crevasses that are present on the glacier and to track their horizontal propagation two different types of satellite images have been used. To track the propagation of fractures over time 21 images from ESA's Landsat-8 satellite in the visible spectrum (true colour images) between September-2014 and September-2018 have been selected. Each image was selected to be spaced approximately one month apart. The images used are shown in Table 3

In order to compare the modelled crevasses with the crevasses present on the glacier a Sentinel-1 C-band radar image of 21-09-2017 was selected. Similarly to the OIB and PIB Sentinel-1 sends out radar signals and measures the travel time and strength of the reflected radar signal. The main difference is that the wavelength of the Sentinel-1 radar is significantly lower than the OIB radar (~5 cm vs ~1.6 m). The smaller wavelength makes it harder for the signal to penetrate the ice and a larger percentage is reflected. The differences in return strength from the glacier surface then allows for the identification of crevasses. The Sentinel-1 image of 21 September was selected as opposed to an image during the summer because the contrast between fractures and surrounding ice is higher when a snow layer is present on the ice.

Table 3 Image acquisition dates of Landsat-8 images used in fracture tracking

Landsat-8 true colour images: [yy-mm-dd]
14-09-30
15-05-01
15-06-03
15-07-04
15-08-01
15-09-01
16-04-01
16-04-30
16-06-01
16-06-26
16-08-01
17-03-22
17-05-01
17-06-01
17-07-01
17-08-09
17-09-22
18-03-22
18-05-01
18-06-01
18-07-01

4. Method

The method chapter starts with the statistical analysis of the temperature and runoff+SMB data over the Petermann glacier. The temperature over Greenland is showing a long term upward trend (Hanna et al. 2008), however the magnitude of this trend is varying strongly between different areas on Greenland (Westergaard-Nielsen et al. 2018). With temperature records and HIRHAM5 regional climate model output going back to the 1950s and 1980s trends in the temperature data and HIRHAM5 model output were computed. The average temperature on the glacier has a direct effect on the ice viscosity (Cuffey and Paterson, 2010) which was used in the LEFM crevasse depth model. The SMB and runoff product from the HIRHAM5/MODIS regional climate model were used in the calculation of the basal melt rate and to determine a threshold value for the availability of water for hydrofracturing respectively. The way the trends are calculated and how the threshold value for hydrofracturing was selected is discussed in the "Climate model and temperature data statistics" section

The surface elevation/bottom draft and thickness change profiles from the PIB/OIB data were used in order to identify locations where the thickness change is particularly high and possibly basal crevasses have formed. The section: "Pre-IceBridge and Operation IceBridge," discusses how the thickness change in a Lagrangian and Eulerian reference frame from the pre-IB/OIB surface elevation and bottom draft was calculated.

The combination of the thickness change based on the ArcticDEM elevation maps and SMB from HIRHAM5 was used to determine which percentage of total thickness change is due to basal melt. The thickness maps used in the calculation of thickness change over the entire floating ice shelf were later used in the LEFM crevasse depth model as well. The "ArcticDEM thickness change and basal melt rate" section describes the process of calculating ice thickness from surface elevation and the calculation of thickness change in a Lagrangian and Eulerian framework.

The stress plays an important role in the LEFM crevasse depth model. The process of going from velocity to strain rate to stress is discussed in the "Velocity, strain and stress" section

The fracturing that took place between 2014 and 2018 was tracked in order to identify the regions on the glacier that might lead to a future calving event. The locations of these fractures were then compared with the locations with high levels of (basal) melt and that showed high crevasse depth over ice thickness ratios calculated from the LEFM crevasse depth model. The way the fractures were tracked is discussed in the "Fracture tracking" section.

Lastly the four different experiments that were performed using the LEFM crevasse depth model are explained. The four LEFM model experiments combine almost all the data and results that were calculated earlier and were used to make a prediction on the future stability of the floating ice shelf of the Petemann glacier. The different settings and input used in the LEFM model are discussed in thee "Linear elastic fracture mechanics crevasse depth model" section.

4.1 Climate model and temperature data statistics

4.1.1 Temperature statistics

In order to provide a longer time series of temperature data of on the Petermann glacier, than the four years of observations from the automatic weather station, the AWS temperature data was compared to the HIRHAM5 model output and Alert weather station data. A comparison based on the normalized RMSE and the correlation coefficient was used to assess whether one or both sources are representative for the situation on the Petermann glacier. Based on the longer time series of the Alert data and HIRHAM5 model output two linear trends were fitted through both data sets. Using the data gap of the Alert time series between 1971 and 1998 as a divide resulting in a 1957-1971 and a 1998-2018 trend for Alert and a 1980-1998 and 1998-2017 trend for HIRHAM5. The statistical validity of the trends was determined by their p-value. Trends with a p-value below the significance level of 0.05 were accepted. A p-value below 0.05 means that the chance there is no correlation between the linear trend and the data is low. For both the AWS and Alert weather station the standard deviation of the AWS is used 0.1 K. For further analysis of the respective summer and winter temperature change the Alert summer, winter and yearly mean temperature anomalies were calculated. The anomalies of the summer average, (months: June, July and August), winter average (months: December, January, February) and annual average for each year were calculated with respect to 1957-1971 respective summer, winter and yearly mean temperatures.

4.1.2 HIRHAM5/MODIS runoff and surface mass balance

Similar to the temperature time series the HIRHAM5/MODIS model runoff between 1980 and 2017 was split up in two parts. Since the HIRHAM5/MODIS uses satellite data from a satellite that was launched in 1999 a selection is made based on the availability of satellite data. For both the pre-MODIS time from 1980-2000 and the post-MODIS time from 2000-2017 a linear trend and mean runoff per cell was calculated respectively. The same pre-MODIS/post-MODIS divide was applied to the SMB product of the HIRHAM5/MODIS model. In order to get the thickness change due to the SMB between January 2011 and January 2018 the HIRHAM5/MODIS SMB was extrapolated to include 2017 based on the average SMB between 2011 and 2017 and the post-MODIS trend.

4.2 Pre-IceBridge and Operation IceBridge

In order to compare the ice thickness profiles of the PIB and OIB from different years the surface and bottom profiles were first referenced to the water level in the Petermann fjord. Not every flight line passes over a stretch of water making simply shifting the profiles based on the water level impossible. The water level of every profiles was set to zero by correcting for the height difference between the WGS-84 ellipsoid and mean sea level, a tidal offset, a firn/snow layer and a possible platform offset. The height above sea level of floating ice is related to the ice thickness and the ratio of the density of sea water over the density of ice following the principle of Archimedes. Similar to the approach of Münchow et al. (2014b) this relation between ice thickness and surface elevation above sea level was used to calculate the sum of the combined offsets and the ratio between the density of ice and the density water. From Equation (45) both the ratio and offset were calculated:

$$Z = \text{ratio} * I + \text{offset} \quad (45)$$

Z is the surface elevation above the WGS-84 ellipsoid, where only data of the floating ice shelf is selected and grounded ice is excluded. Ice thickness I was calculated by taking the difference between the surface elevation and bottom draft and since the offsets are equal for the surface and bottom the ice thickness is independent of the chosen reference system. ratio is defined as $1-\rho_{ice}/\rho_{water}$ where ρ_{ice}

is the density of ice and ρ_{water} is the density of water, with ρ_{ice} = 917 kgm^{-3} and ρ_{water} = 1027 kgm^{-3} based on Münchow et al. (2014b). The offset and ratio were calculated via least-squares and are assumed to be constant along the flight line.

After referencing the surface elevations and bottom drafts to sea level the change in ice thickness was calculated both in a Lagrangian and in Eulerian framework. The thickness change in a Lagrangian framework required the profiles to be shifted by the distance the ice has travelled within the time difference between the profiles. Profiles before 2010 were shifted using the average flow velocity from the ERS-1/ERS-2/ENVI ESA CCI data between 2002 and 2010. The profiles between 2010 and 2017 were shifted using the average flow velocity from the Sentinel-1 ENVEO data of 2015. In order to remove the influence of small mismatches due to thickness undulations and to match the sample spacing of each profile a moving average filter with a window size of 300 m was applied over the shifted thickness profiles. The Lagrangian average thickness change per year was then calculated by taking the thickness difference between consecutive profiles and dividing by the time difference between the acquisition dates.

The Euler framework did not require the profiles to be shifted, but had as a downside that (basal) crevasses and cavities cause strong fluctuations in the thickness change over time. These fluctuations can be the result of crevasses propagating downstream and are therefore not necessarily due to changes in melt rate. In order to reduce the influence of the propagation of crevasses the average thickness change along the profile was calculated by applying a moving average filter with a window size of 20 km on the thickness profile of the Central Eastern transect and a window size of 10 km on the Western transect. The window size captures the large spatial scale fluctuations and reduces the influence of small scale undulations, but this also means the calculated thickness change in the Eulerian framework is only a moving average along each profile.

4.3 ArcticDEM thickness change and basal melt rate

4.3.1 Ice thickness from surface elevation

Two ice thickness maps were created for the calculation of the thickness change between 2011 and 2017 from ArcticDEM surface elevation data. In order to calculate ice thickness from surface elevation the data was first referenced to the sea level in the Petermann fjord by applying a series of (offset) corrections. The DEMs of 2011 and 2017 containing the surface elevation data were each constructed by combining three different DEM strips. Each DEM strip was first regridded from a 2x2 m resolution grid to a 30x30 m resolution grid for computational purposes. The DEM strips were then corrected for the elevation offset provided with the data and a tidal offset based on the acquisition date using the AOTIM-5 tidal model. Both offsets were considered constant over a DEM strip. On strip WV01_20170716 an additional offset correction of 3.5 m was applied based on the average remaining offset present between overlapping areas with the neighbouring DEM strip. After the offset and tidal correction the strips were merged into one single DEM and referenced to sea level by subtracting the geoid heights from the surface elevation. The geoid heights from the EMG-2000 model are provided on a 1x1 degree grid and were first regridded to match the 30x30 m DEM grid. After the conversion from ellipsoidal height to height above sea level the ice thickness was calculated using equation (46):

$$\mathrm{I} = \mathrm{H}\frac{\rho_\mathrm{w}}{(\rho_\mathrm{w} - \rho_\mathrm{i})} \qquad (46)$$

Where I is the ice thickness, H is the surface height above sea level, ρ_w the density of sea water and ρ_i the density of ice. With $\rho_w = 1027\ kgm^{-3}$ and $\rho_i = 917\ kgm^{-3}$ based on Münchow et al. (2014b). An estimation of the uncertainty of the ice thickness derived from the ArcticDEM is made by calculating the RMSE between the DEM and OIB surface elevation.

4.3.2 Drainage from surface elevation and drainage threshold

The drainage paths of the Petermann glacier were calculated in order to get the locations where water is available for hydrofracturing. Using the surface elevation from the 2017 ArcticDEM DEM as input in the watershed function of QGIS the drainage area of each point was calculated. A threshold of significant drainage was determined based on the observation of Macdonald et al. (2018) that glacial lakes on the Petermann ice shelf can drain within a day through hydrofracturing and the dimensions of small crevasse that penetrates the average ice thickness of the Petermann glacier. Macdonald et al. (2018) showed a daily mean runoff, using the HIRHAM5/MODIS runoff output of 2014/2015/2016, over the Petermann glacier of ~35 mm weq day^{-1} during the month of July. The 35 mm weq day^{-1} runoff would allow a cell with a drainage area of 5000 cells to fill up a 300 m deep, 100 m long and 5 m wide crevasse within a day. The threshold for the number of cells that one cell drains is based on the requirement that a relative small crevasse can be filled within a day and is therefore set to 5000. During the LEFM crevasse depth experiments the threshold was used to determine which locations on the floating ice shelf contained enough water for hydrofracturing.

4.3.3 Eulerian and Lagrangian thickness change from ArcticDEM.

From the two thickness maps of 2011 and 2017 both the thickness change in the Lagrangian and Eulerian frame work have been calculated. The average thickness change between 2011 and 2017 in an Eulerian framework was calculated by subtracting the ice thickness of 2011 from the ice thickness of 2017 and dividing the difference by six years.

The thickness change in a Lagrangian framework was calculated by shifting the 2011 thickness map to match the 2017 thickness map. The shifting was performed along the flow lines of the glacier. A flow line shows the path the ice follows given a certain start location and was computed using the stream2 function of Matlab. Each flow line was calculated from Sentinel-1 ENVEO velocity data of 2015 interpolated on the 2017 DEM grid. Both the 2011 and 2017 ice thickness was interpolated on the flow lines and the ice thickness data of 2011 was shifted with a distance based on the average Sentinel-1 ENVEO velocity of 2015 multiplied by six years. Finally the Lagrangian thickness change was calculated by subtracting the shifted thickness of 2011 from the 2017 thickness and dividing the difference by six years.

4.3.4 Basal Melt rate

The total thickness change consists of three contributions: basal melt balance, surface mass balance and dynamic thinning. The importance of dynamic thinning is considered negligible for the Petermann glacier according to Münchow et al. (2016). By subtracting the SMB from the Lagrangian thickness change the basal mass balance was calculated over the floating part of the Petermann glacier. Based on the total thickness change, basal mass balance and SMB the respective contributions of each source of melting to the total thickness change was determined.

4.4 Velocity, strain and stress

4.4.1 Inter-annual velocity variation

To analyse the inter-annual velocity and the spatial variation of the velocity the flow velocity was selected along three transects across the glacier using the ERS-1/2 and ENVISAT velocity data from 1992 till 2011 and the Sentinel-1 data from 2015 till 2018. The transects were chosen to show the velocity of the grounded ice, floating ice between the grounding line and the calving front and the ice near the calving front. In the comparison of the velocity between years the average of the months of January, February and March was used. The reason only winter velocity was used is due to the larger spatial data coverage during these months.

4.4.2 Stress and strain calculation

In order to analyse the stresses on the glacier and use the stress as input for the LEFM model the first principle stress was calculated from the ERS-1/2 and ENVISAT and Sentinel-1 ENVEO velocity data. The velocity data is provided in east and north direction, so in order to get the velocity and strain rate in the direction of and perpendicular to the flow the velocity data was first interpolated to a grid where the y-axis aligns with the average flow direction (Figure 17, left) and then rotated using the average flow direction θ (Figure 17, right). The average flow direction was determined by dividing the velocity field in sections of ~10 km long where each section is considered to have a uniform flow direction.

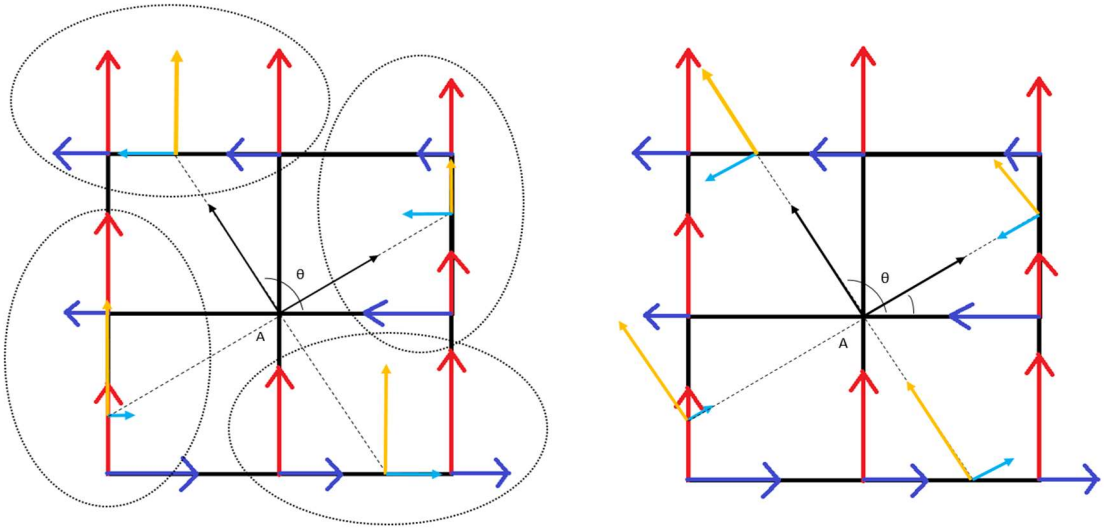

Figure 17 Interpolation of the velocity data to rotated grid (left). Rotation of the interpolated velocity with the angle of the average flow direction

With the ice velocity data relative to the direction of the flow and perpendicular to the flow the data was used to calculate the principle strain rates using equation 4, 5 and 6 from the background section based on the theory of Nye (1959). The principle strain rates were then used to calculate the first principle stress using Glen's flow law, equation 9 and 10 from the background section, with flow parameter $n = 3$ (Cuffey and Paterson 2010) and creep parameter $A = 3.0\mathrm{e}^{-25}\ s^{-1}\mathrm{Pa}^{-3}$ based on Rückamp et al (2019).

4.4.3 Intra-annual velocity and tensile stress variation

To analyse the intra-annual changes in the flow velocity and tensile stress of the glacier between January 2015 and August 2018 the average flow velocity and tensile stress of the floating ice shelf was calculated from the Sentinel-1 ENVEO velocity data using only velocity maps with a spatial coverage larger than 75%. From the first principles stress only the positive values were selected in order to show the true tensile stress over the glacier.

4.5 Fracture tracking

Three main fracture zones were identified on the Petermann glacier by visually inspecting Landsat-8 images between 2014 and 2018. In order to track the propagation of the fractures in the identified fracture zones of each separate image a polygon was manually overlaid on the fractures. From each of these polygons the fracture length was then calculated.

4.6 Linear elastic fracture mechanics crevasse depth model

To model the propagation of fractures on the Petermann glacier the LEFM theory, as described in the background chapter on LEFM, was applied over the floating part of the glacier. Four different experiments were performed, where each of the experiments corresponds to one of the different processes that influence fracture propagation.

Using the principle of Van der Veen (1998) the theoretical crevasse depth at every point on a 60x60 m grid was calculated. The final crevasse depth was taken to be the depth at which the total SIF falls below the fracture toughness. In order to show the crevasse depth relative to the ice thickness the final crevasse depth was divided by the ice thickness. To keep computational time within an acceptable limit the ice thickness data was first rounded to the nearest meter. The parameters that were kept the same in every experiment are shown in Table 4. The input that changed with every experiment was the ice thickness, stress map and water availability. Water availability was determined based on the drainage map and the earlier discussed threshold value. In locations with a drainage area larger than the threshold values the water level was kept at a fixed level of 5 m below the surface.

Table 4 LEFM model parameters used in every experiment. Fracture toughness based on Petrovic (2003), ice density based on Cuffey and Paterson 2010. The crevasse spacing is based on observed crevasses on the Petermann glacier on 07/08/2018 at Lat: 80.825, Lng: -60.52. Initial crevasse depth based on Mottram and Ben (2009).

Parameter:	**Symbol:**	**Value:**
Crevasse spacing	W	500 [m]
Fracture toughness	K_c^1	100000 [Pa]
Density of water	ρ_w	1000 [kg/m^3]
Density of ice	ρ_{ice}	917 [kg/m^3]
Initial crevasse depth	d_0	1e^{-7} [m]

4.6.1 Experiment 1

The crevasse depth over ice thickness ratio of the first scenario with the standard settings of 2017 was calculated in order to compare the outcome to a sentinel-1 backscatter image showing the fractures on the Petermann glacier. The data used in the standard scenario is shown in Table 5.

4.6.2 Experiment 2

The second experiment was used to show the influence of an increase in runoff on the propagation of crevasses. The water availability threshold in order to fill the specified crevasse of the standard scenario was a drainage area of 5000 cells. The 5000 cells drainage threshold is based on the approximate average mean daily runoff of 35 mm weq Macdonald et al. (2018) showed. Macdonald et al. (2018) also showed that the maximum mean daily runoff during 2014/2015/2016 was approximately 1.5 times higher than the 35 mm weq. To simulate the effect on crevasse propagation of the maximum value compared to the approximate average July runoff the threshold is lowered to 3333 in the "increase in water" scenario. This corresponds to a 50% increase in runoff with respect to the standard scenario. The comparison was made by subtracting the calculated crevasse depth over ice thickness of the "increase in water" scenario from the standard scenario. The data used in the "increase in water" scenario is shown in Table 5.

4.6 3 Experiment 3

The third experiment was conducted to show the effect of a reduction in ice thickness on the ratio of crevasse depth over ice thickness. The experiment is split in two parts: the difference between the 2011 and the standard 2017 scenario without water and the difference between the standard 2017 without water and a hypothetical 2020 scenario. In the 2011 scenario the shifted ArcticDEM derived ice thickness map was used in order to show the effect of the total thickness change. In the 2020 scenario the Lagrangian ice thickness change between 2011 and 2017 was assumed to be constant over the period 2017-2020. For every year between 2017 and 2020 the ice thickness was calculated by applying the fixed Lagrangian thickness change and shifting the thickness map along the flowlines with a distance equal to the average annual speed of 2015 from the Sentinel-1 ENVEO data set. After three years of additional thickness change the 2020 ice thickness map was shifted back along the flowlines to match the 2017 position in order to show the effect of the total thickness change on the crevasse depth over ice thickness ratio. The data used in the standard 2017 scenario without water is shown in Table 5.

4.6 4 Experiment 4

The fourth experiment was performed to show the effect of a change in tensile stress on the crevasse depth over ice thickness ratio. In experiment four the difference in crevasse depth over ice thickness between the standard 2017 scenario without water and the reduced stress scenario was calculated on the 250x250 m grid of the tensile stress. The data used in the standard 2017 scenario without water and the reduced stress scenario is shown in Table 5.

Table 5 Overview of data sets used as input for different scenarios

Scenario:	Ice thickness:	Stress:	Water availability:
Standard	July 2017 ArcticDEM derived ice thickness map	Average first principle stress of July 2017	July 2017 ArcticDEM derived drainage map using a threshold value of 5000 cells.
Increased water	July 2017 ArcticDEM derived ice thickness map	Average first principle stress of July 2017	July 2017 ArcticDEM derived drainage map using a threshold value of 3333 cells.
2011	Shifted June 2011 ArcticDEM derived ice thickness map.	Average first principle stress of July 2017	no water available
2020	Shifted July 2020 ArcticDEM derived ice thickness map	Average first principle stress of July 2017	no water available
Standard without water	July 2017 ArcticDEM derived ice thickness map	Average first principle stress of July 2017	no water available
Reduced stress	July 2017 ArcticDEM derived ice thickness map	Average first principle stress of January 2017	no water available

5. Results

The results are presented in five sections. An atmospheric section showing the temperature evolution on the Petermann glacier, the change in surface water runoff, what percentage of runoff drains of the glacier and where the drainage paths are located.

Secondly a thickness change and melt rate section with the thickness change both in a Lagrangian and Eulerian framework. Along two transects between 2002 and 2017 and over the entire floating ice shelf between 2011 and 2017 the thickness change is presented in order to track the thickness change through time and to show its spatial variation. The combination of total thickness change and surface mass balance is plotted show which percentage of the total thickness change is due to basal melting.

Thirdly a velocity and stress sections to show the evolution of the velocity between 1992 and 2018 and the intra-annual change of the stress and velocity over the floating ice shelf.

Fourthly an overview of the locations where fractures have formed between 2014 and 2018 and the propagation of a selection of these fractures is shown.

Lastly the results of four experiments, using the LEFM theory, are presented to show how certain changing conditions affect the propagation of crevasses on the glacier.

5.1 Atmospheric results

5.1.1 Temperature evolution

Temperature from the AWS, Alert weather station and HIRHAM5 model output between June 2002 and May 2006 is shown in the left panel of Figure 18. The correlation between the AWS and Alert and AWS and HIRHAM5 temperature is shown in the right panel of Figure 18. Both Alert and HIRHAM5 show a high correlation with the AWS temperature which is confirmed by the Pearson correlation coefficient between AWS and Alert and between AWS and HIRHAM5 of 0.9887 and 0.9858 respectively. Despite some Alert summer temperatures and HIRHAM5 winter temperatures being higher than the AWS reported temperatures it follows that the temperature at Alert and the output from HIRHAM5 is representative of that on the Petermann glacier. The normalised root mean square error (NRMSE) between Alert and the AWS temperature is 5.3% and the NRMSE between HIRHAM5 and the AWS is 7.9%.

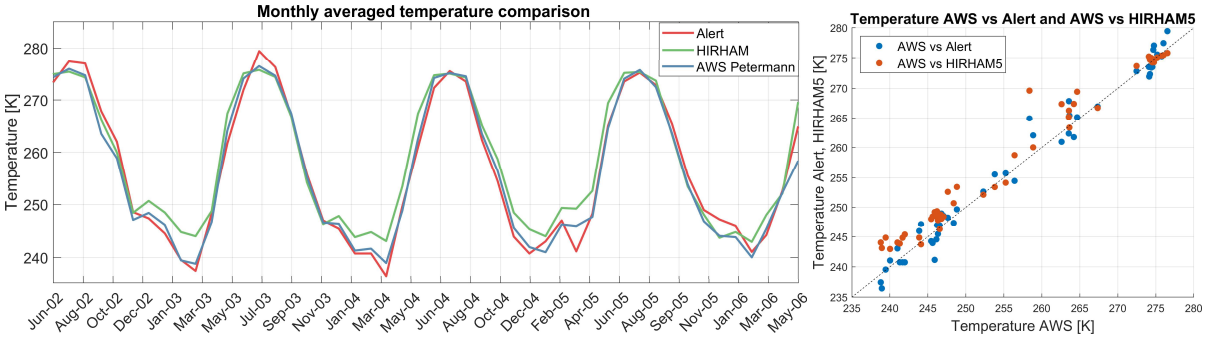

Figure 18 Left: Monthly average temperate of: AWS on the Petermann glacier, Alert weather station Canada and HIRHAM5 temperature output average of the Petermann floating ice shelf. Right: scatter plot between Alert and AWS in blue and HIRHAM5 and AWS in orange. Dashed black line shows a 1:1 ratio between temperatures.

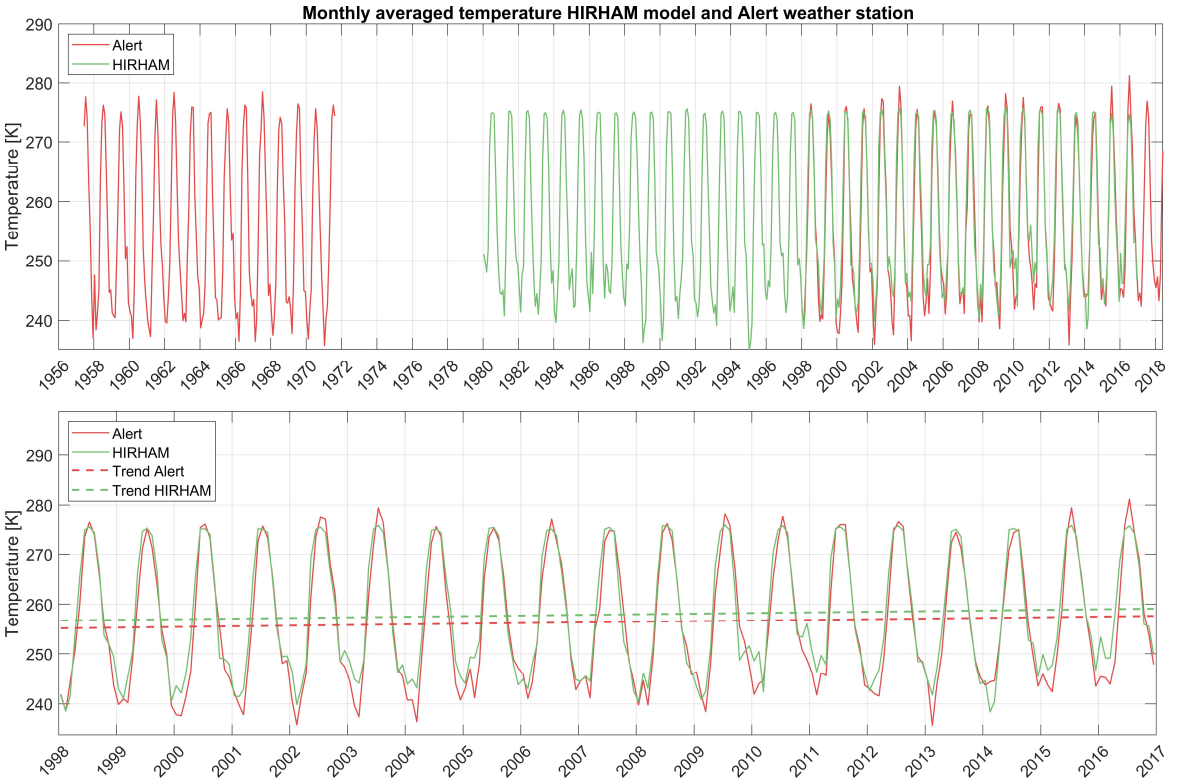

Figure 19 Top: All available temperature data between January 1957 and July 2018 of Alert weather station and between January 1980 and January 2017 HIRHAM5 model output. Bottom: Alert weather station temperature and HIRHAM5 model output between January 1998 and January 2017 with a linear trend fitted through the temperature data starting at January 1998.

To investigate the long term change in temperature over the Petermann glacier the entire temperature record of the Alert weather station and HIRHAM5 model output is plotted in the top panel of Figure 19. During the first 14 years of Alert temperature measurements between January 1957 and January 1971 the mean temperature was 255.26 ± 0.0076 K and no statistically significant trend was present. The HIRHAM5 mean temperature between January 1980 and January 1998 was with 257.07 K almost two degrees higher than the pre 1971 Alert temperature and as with the Alert data no statistically significant trend was present during this period.

A zoom-in of the 1998 -2018 period from the top panel is shown in the bottom panel of Figure 19 where the temperature data and linear trends are plotted. According to the Alert data the average temperature between January 1998 and January 2018 was 256.48 ± 0.0065 K and a statistically significant linear trend shows an average increase of 0.0980 ± 1.5e^{-4} Ka^{-1}. The average HIRHAM5 temperature of the period 1998-2017 is 258.0 K and for the HIRHAM5 temperature a statistically significant trend was found of 0.122 Ka^{-1}.

The Alert weather station summer, winter and total annual mean anomalies with respect to the 1957-1971 period average temperatures are plotted in Figure 20. Similar to what the difference in trend between the 1957-1971 and 1998 -2018 periods shows is that during the latter period the temperature has increased. Figure 20 shows that the change in average annual temperature is predominantly due to an increase in the winter month temperatures as opposed to the summer months.

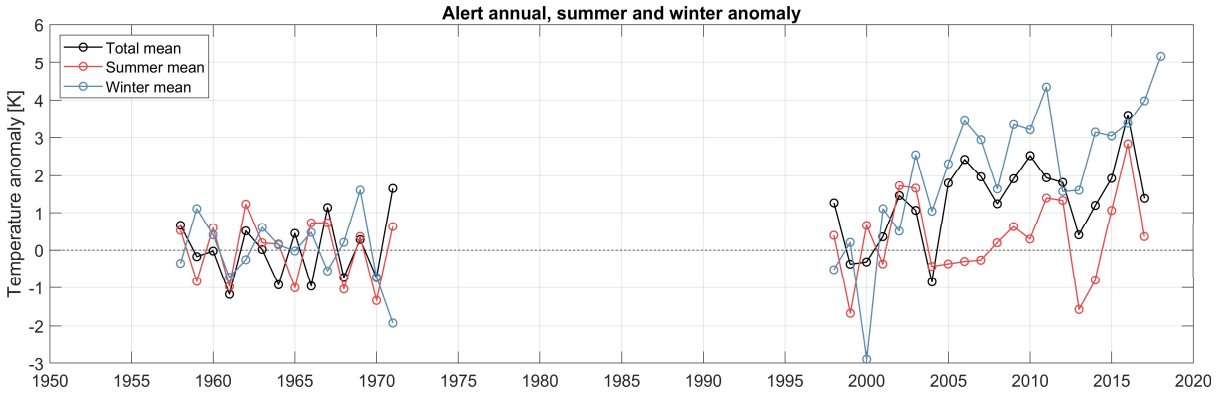

Figure 20 Summer (June, July and August), winter (December, January and February) and total annual temperature anomalies from the Alert weather station between 1957 and 2018 with respect to the respective summer, winter and total averages of the 1957-1971 period. Dashed black line shows the zero anomaly.

5.1.2 Evolution of Runoff

In the top two panels of Figure 21 the linear trend in the runoff from the HIRHAM5/MODIS model over a part of the Petermann glacier is plotted. The two periods show a significant difference in the trend with an average trend of 1.13 mma^{-2} weq between 1980 and 2000 and an average trend of 12.52 mma^{-2} weq between 2000 and 2017. Over a period of 16 years the average trend of 12.52 mma^{-2} weq caused an increase of 200.32 mm a^{-1} weq over the Petermann glacier. This is an increase of 47% with respect to the average runoff over the glacier between 2000 and 2017. The trend in the runoff is especially high over the grounded part of the glacier with values reaching over 30 mma^{-2} weq whereas the runoff has increased by a relative small amount over the floating part of the glacier. This difference in trend is offset by the average runoff which is higher over the floating ice shelf (between 1000 and 1400 mm a^{-1} weq) compared to the grounded part (between 0 and 800 mm a^{-1} weq) as shown in the bottom panels of Figure 21.

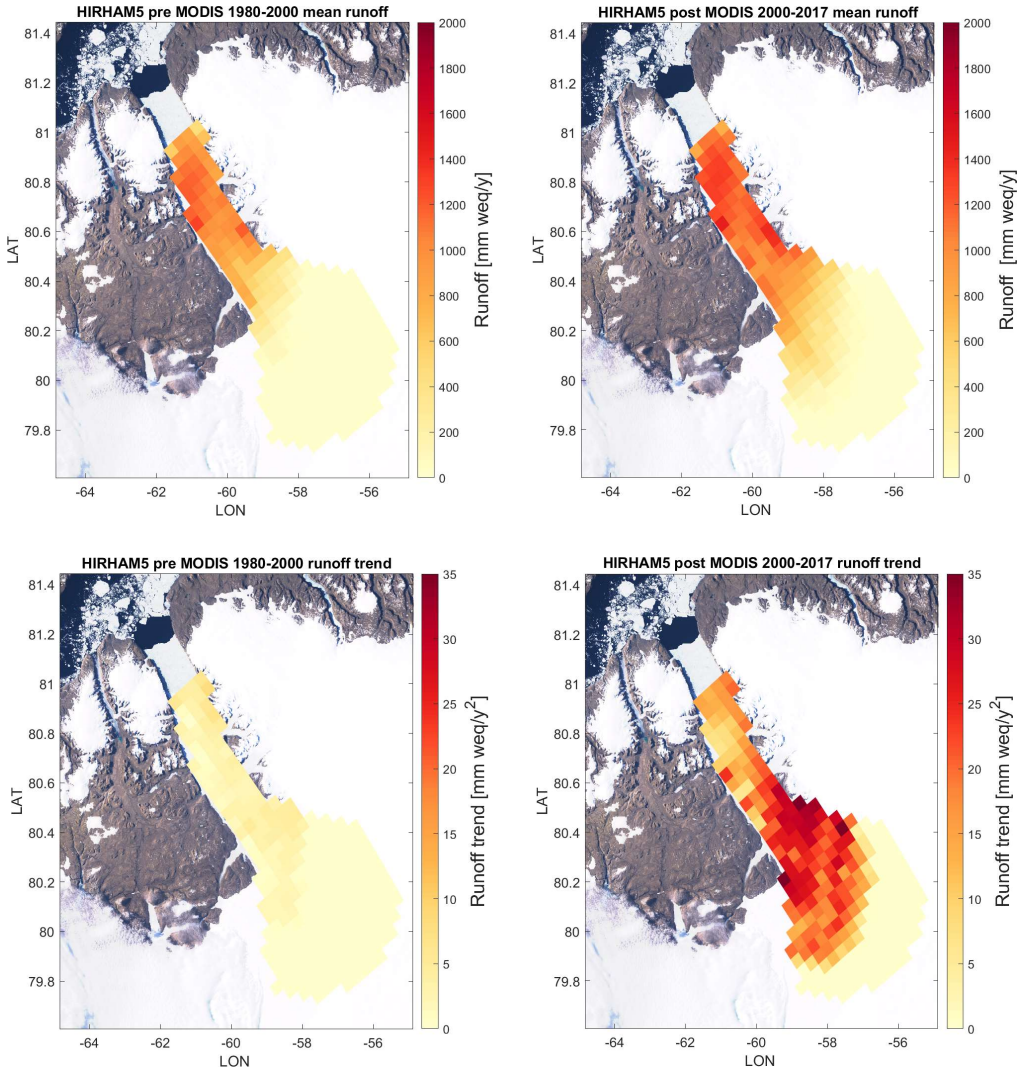

Figure 21 Runoff from HIRHAM5/MODIS model between 1980 and 2017 over a Landsat-8 image from: 2018-07-18. Top left: Linear trend in runoff per cell between 1980 and 2000. Top right: Linear trend in runoff per cell between 2000 and 2017. Bottom left: average runoff

5.1.3 Runoff drainage paths

Based on the drainage paths from Figure 22 81% percent of the runoff from the glacier is transported into the fjord either at the calving front or at the margins of the glacier. The drainage map shows only the drainage paths that drain more than 5000 cells. With each cell spanning an area of 900 m^2 a drainage area of 5000 cells corresponds to a total area of 4.5 km^2

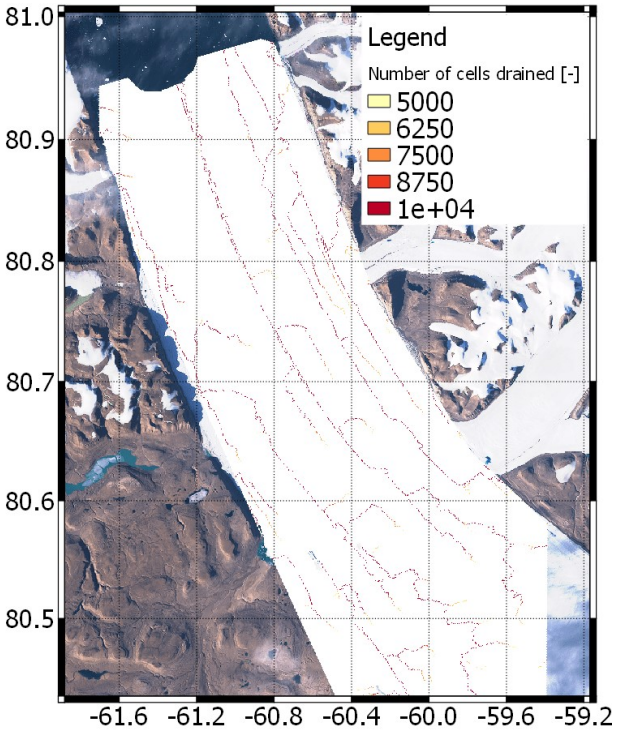

Figure 22 Drainage paths of the Petermann glacier based on 2017 surface elevation. Only drainage paths that drain more than 5000 cells are shown.

5.2 Ice thickness, thickness change and melt rates

5.2.1 Ice thickness

The 2017 ice thickness derived from surface elevation is shown in Figure 23. Based on the comparison between DEM derived ice thickness and OIB derived ice thickness of the Wester flight line the uncertainty in ice thickness is approximately 26 m. In Figure 23 three areas have been identified where the ice shelf has a considerably lower ice thickness compared to the surrounding ice. The western channel outlines an area where the average ice thickness is ~150 m and ranges between ~250 and ~13 m. The average thickness is approximately 80 m less than the area west of the channel and approximately 170 m less than the area between the western and central channel. The central and eastern channel outline regions where the ice thickness is on average ~100 m and ranges between ~200 and ~20m. The ice thickness between the central and the eastern channel decreases from ~300 m in the south to ~200 m at the calving front. The ice thickness east of the eastern channel shows a similar decrease and decreases from ~300 m in the south to ~100 m at the calving front. From this point onwards the area west of the central channel is called the Western ice shelf and the area between the central channel and the eastern channel is called the eastern ice shelf. The three fracture zones are shown in blue. Both fracture zone A and C are located on the central channel. Fracture zone B overlaps with the western channel.

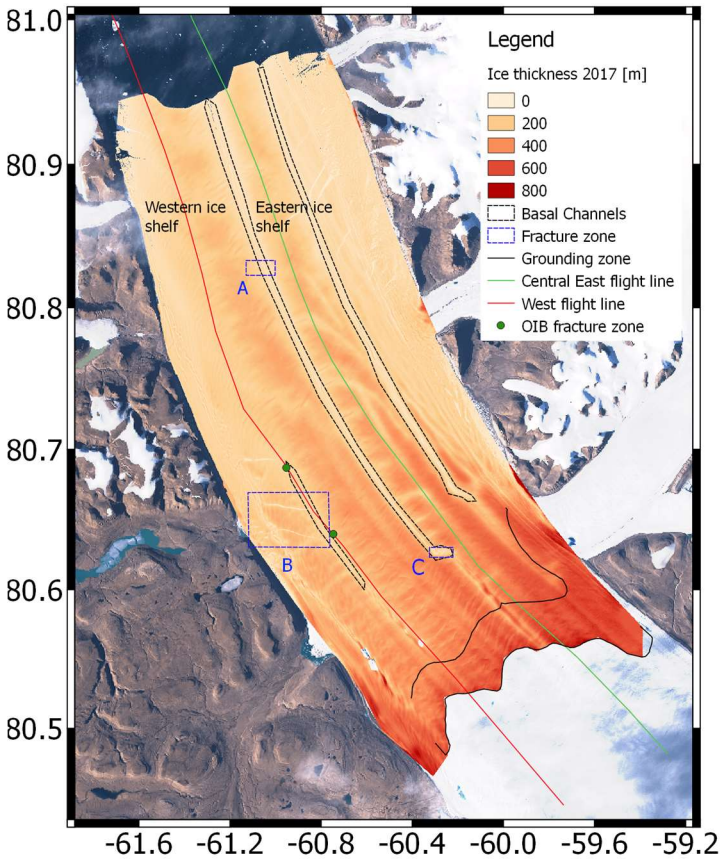

Figure 23 Surface elevation derived ice thickness of 2017. Basal channels from left to right: western channel, central channel and eastern channel. Ice shelf on either side of the central channel are named ambient ice shelfs. Fracture zones A,B and C in blue. Fracture zone identified in PIB/OIB flight line West as green dots. 2017 grounding zone as solid black line.

5.2.2 Surface elevation + bottom draft and thickness change profiles

Following the western flight line from pre-OIB/OIB the surface elevation and bottom draft as well as the thickness change rate between 2002 and 2017 is plotted in Figure 24. The change from grounded to floating ice is marked by the grounding zone in black and the location where recent fractures have been observed is marked by the blue fracture zone. Both in the Lagrangian and Eulerian framework are the thickness changes rates are highest near the grounding line and in the fracture zone. The Eulerian thickness change in panel b of Figure 24 shows that a cavity started to form in the fracture zone between 2011 and 2014 and that this cavity kept growing between 2014 and 2017 with an increased thickness change rate of approximately -15 ±4 ma^{-1}. The shifted surface elevation and bottom draft profiles in the third panel of Figure 24 show that between 2002 and 2011 basal crevasses started to form near the grounding line. These basal crevasses kept growing between 2011 and 2017 with Lagrangian thickness change rates exceeding -80 ma^{-1}.

In Figure 25 the ice thickness and thickness change rate between 2002 and 2017 is plotted along the central eastern flight line from pre-OIB/OIB. The thickness change rate is plotted both in an Eulerian and Lagrangian reference frame. Similar to Figure 24 the change from grounded to floating ice is marked by the grounding zone in black. Along the central eastern flight line there is no sign of a cavity or strong basal crevassing near the grounding line. Instead basal crevasses formed roughly between a distance of 30 and 50 km from the reference point as shown along the shifted profiles of Figure 25 C. The majority of the basal crevasses formed between 2002 and 2013 and are the major contributor to the total thickness change. The Eulerian thickness change does not capture these changes over small distances and shows a fairly uniform thickness change between 0 and -5 ma^{-1}. The exception is the thickness change between 2011 and 2013 near the grounding line between -10 and -15 ma^{-1} and a positive thickness change near the calving front of 5 ma^{-1}.

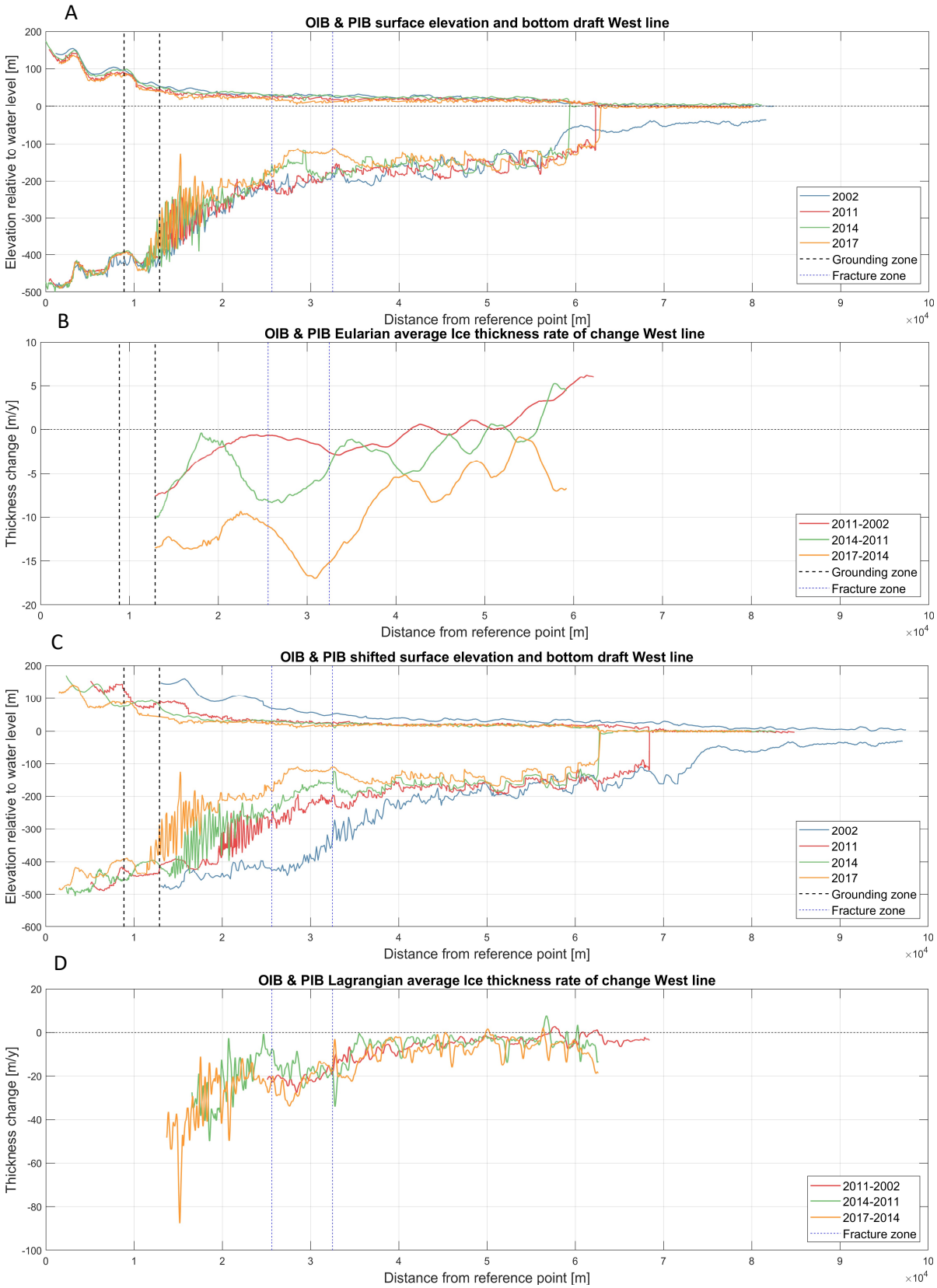

Figure 24 A: Surface elevation and bottom draft along the Western flight line of pre-OIB/OIB between 2002 and 2017. B: The average thickness change per year in a Eulerian framework smoothed with a moving average filter with a window size of 10 km. C: Surface elevation and bottom draft profiles shifted along the flight line to match the position of the 2017 profile. D: The thickness change rate in a Lagrangian framework smoothed with a moving average filter with a window size of 300 m where only floating ice is compared. The change from grounded to floating ice in the grounding zone is shown as two vertical black dotted lines and the location where new fractures have been observed as the fracture zone in blue. All profiles are referenced to the sea level which is shown as the horizontal zero line.

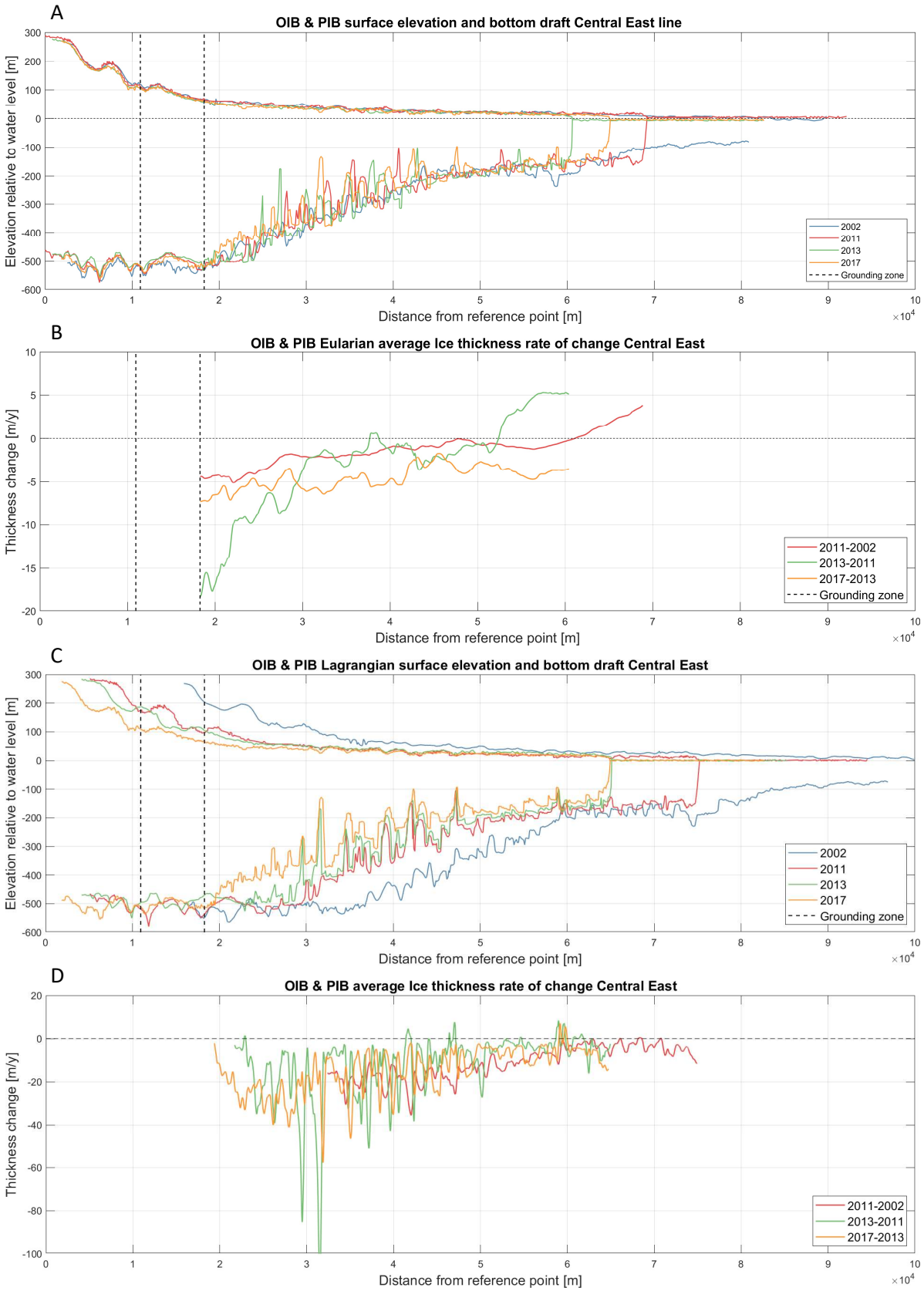

Figure 25 A: Surface elevation and bottom draft along the Central Eastern flight line of pre-OIB/OIB between 2002 and 2017. B: The average thickness change per year in an Eulerian framework smoothed with a moving average filter with a window size of 20 km. C: Surface elevation and bottom draft profiles shifted along the flight line to match the position of the 2017 profile. D: Thickness change rate in a Lagrangian framework smoothed with a moving average filter with a window size of 300 m where only floating ice is compared. The change from grounded to floating ice in the grounding zone shown as two vertical black dotted lines and the location where new fractures have been observed as the fracture zone in blue. All profiles are referenced to the sea level which is shown as the horizontal zero line.

5.2.3 Surface elevation derived ice thickness change

The ice thickness change between 2011 and 2017 is shown in Figure 26 where the thickness change is shown both in a Lagrangian and Eulerian framework. The fracture zone which is depicted in Figure 24 as two blue vertical lines is located between the two green dots. The shifted grounding zone in orange and the 2017 grounding line in black indicate where the assumption of floating ice becomes invalid. The left panel of Figure 26 shows the Lagrangian thickness change between two outer flow lines shown as black dashed lines. The Lagrangian map shows a similar change in thickness per year as in Figure 24 and Figure 25 with a relative high thickness change per year near the grounding line between -25 ±6 to -50 ±6 m a^{-1} and values close to zero near the calving front. Along all three basal channels the thickness change rate is approximately -50 ±6 m a^{-1} at the southern end and reduces within several kilometres to the surrounding thickness change rate. The right panel of Figure 26 shows the thickness change rate in an Eulerian framework. The ice thickness was not smoothed and shows a large variation in the thickness change rate with strong negative as well as strong positive thickness change rates. The areas outside of the two flow lines of the Eulerian thickness change rate show a more random signal with no clear overall thickening or thinning. In the fracture zone the thickness change rate is negative both in the Lagrangian and the Eulerian framework with thickness change rate values between -10 ±6 and -20 ±6 ma^{-1}.

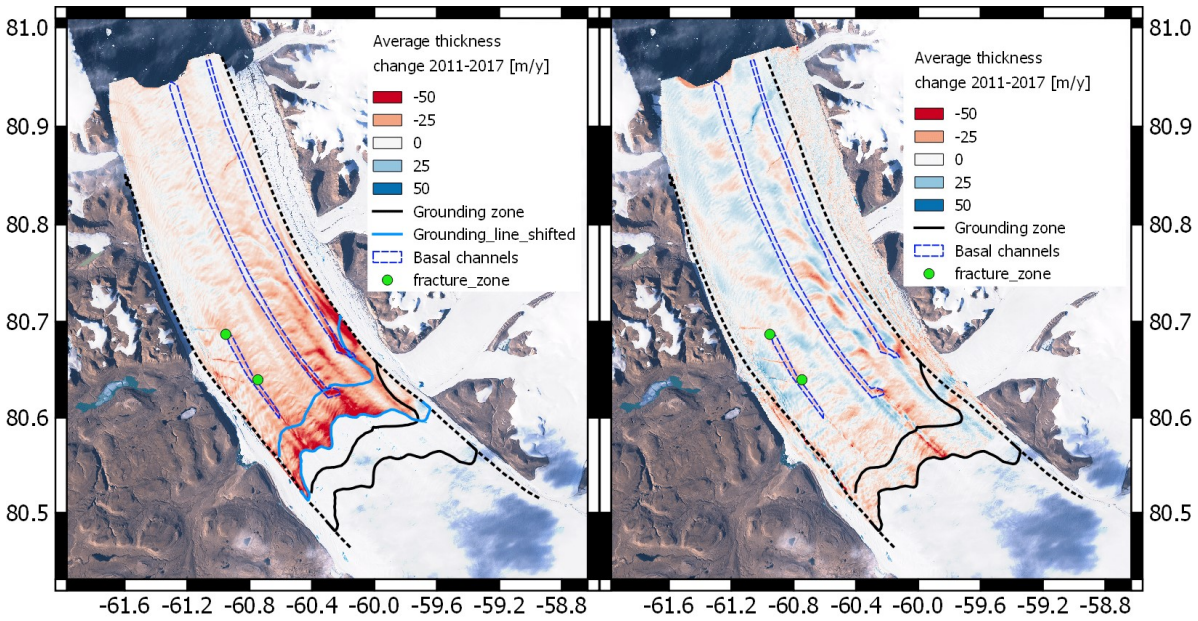

Figure 26 Thickness change rates over the Petermann glacier. Background: Sentinel-2 Aug-2016 image with latitude on the vertical and longitude on the horizontal axis. Left: Lagrangian ice thickness change between 2011 and 2017 derived from surface elevation data between the two flow lines shown as black dashed lines. Two grounding zones are shown which mark the transition from floating to grounded ice of the 2017 thickness in black and of the 2011 thickness in orange. Right: Thickness change in an Eulerian framework over the entire floating ice shelf with the grounding zone of 2017 and 2011 at the same location shown in black.

5.2.3 Melt rates

The basal mass balance and SMB are shown in Figure 27. The Basal mass balance is, averaged over the entire floating ice shelf, -8.85 ma^{-1}. The average SMB between 2011 and 2017 is far more uniform over the glacier compared to the basal melt and is between -1 and -1.5 ma^{-1} weq. The Basal mass balance is very similar to the Lagrangian thickness change as on average ~89% of the total thickness change is due to basal melt.

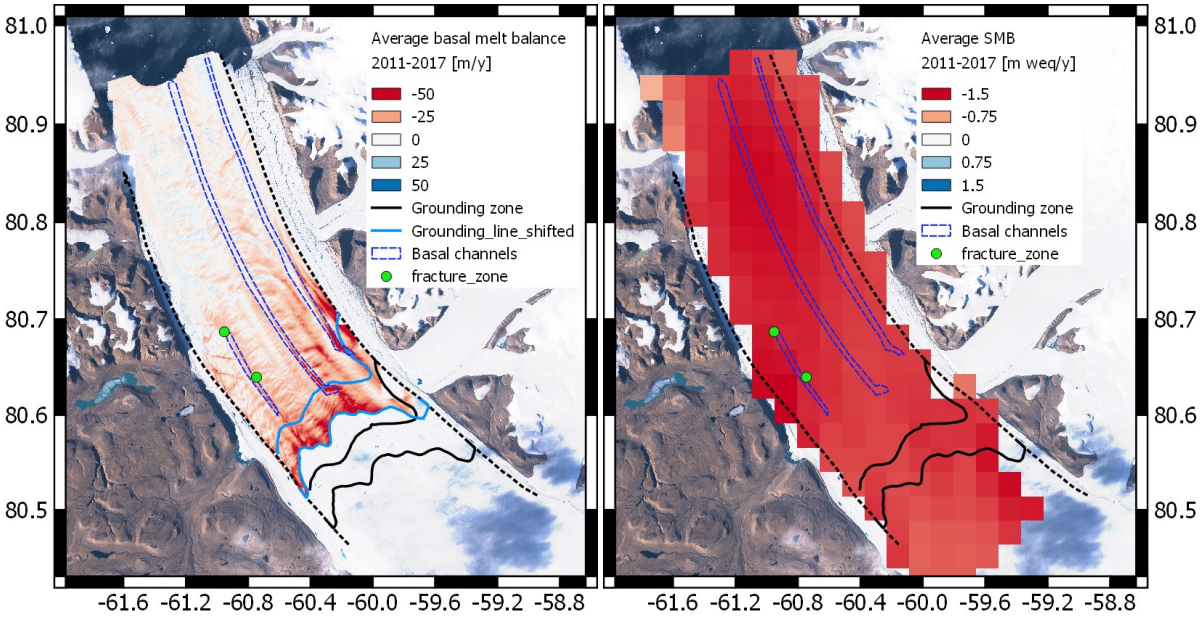

Figure 27 Melt rates over the Petermann glacier. Background: Sentinel-2 Aug-2016 image with latitude on the vertical and longitude on the horizontal axis. Two grounding zones are shown which mark the transition from floating to grounded ice of the 2017 thickness in black and of the 2011 thickness in orange. Left: Basal melt rate between 2011 and 2017 derived from the Lagrangian thickness change and the SMB. Right: SMB over the Petermann glacier from HIRHAM5/MODIS output

5.3 Velocity and stress

5.3.1 Velocity transects

Three different velocity transects are shown in Figure 28 with velocity data between 1991 and 2018. Of each year only the average velocity of January, February and March is used. All three transects show higher velocities between 2015 and 2018 compared to the 1991-2010 period. The average velocity between 2015 and 2018 along the northern transect increased by ~10% with respect the average velocity between 1991 and 2010. Along the center transect this increase was ~9% and ~4% along the southern transect.

Besides the increase in velocity of the Petermann glacier the velocity gradient along the central transect changed as well. Along this transect two distinct velocity peaks separated by a trough formed. The velocity difference between the trough and the two peak was 73 ma^{-1} in 2018 and 86 ma^{-1} in 2017, with an average standard deviation in this area of ~85 ma^{-1}. Before 2017 no clear gradient is observed. The location of the velocity gradient corresponds to the location of the central channel which is located between the two vertical dashed black lines shown in Figure 28. Further down the glacier the velocity remaind fairly uniform along the transect and no change in gradient was observed.

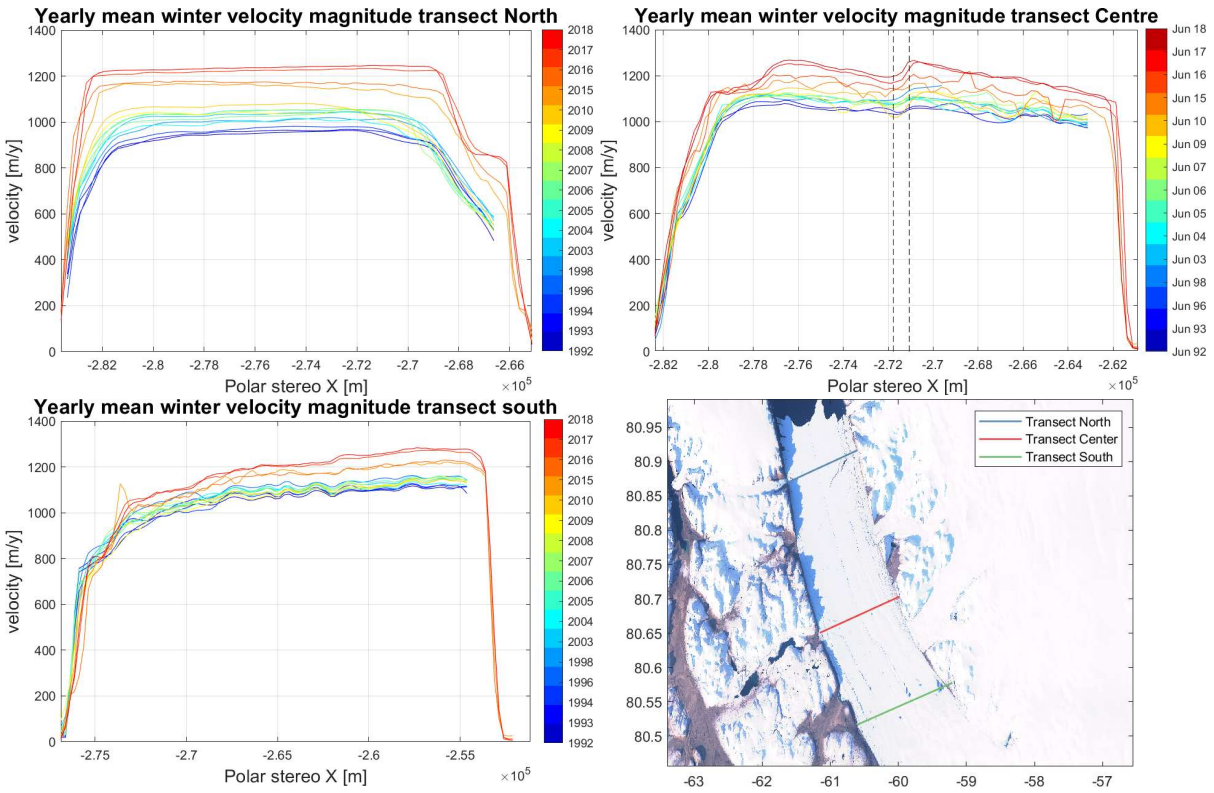

Figure 28 Top and bottom left: Winter velocity (January, February, March) transect of ENVI/ERS-1/ERS-2 data up to 2011 and Sentinel-1 data from 2015 till 2019. Top right: Winter velocity (January, February, March) transect of ENVI/ERS-1/ERS-2 data up to 2011 and Sentinel-1 data from 2015 till 2019 with location of central channel between the two vertical black dashed lines. Bottom right: Overview of transect locations over Sentinel-2 Aug-2016 image with latitude on the vertical and longitude on the horizontal axis

5.3.2 Intra-annual velocity and stress variation

The stress calculated from the strain rate is proportional to the spatial gradient in the velocity not the velocity magnitude. To show that the tensile stress is increasing with increasing flow velocities the first principle stress averaged over the floating part of the glacier is plotted as function of time in Figure 29. The measurement points during the summer months of June, July and August are plotted in red, the rest of the measurements, from September to May, are plotted in blue. Since only the positive tensile stress is relevant for fracturing the negative values are not included. From Figure 29 it is clear that both the tensile stress and the flow velocity increases during the summer months.

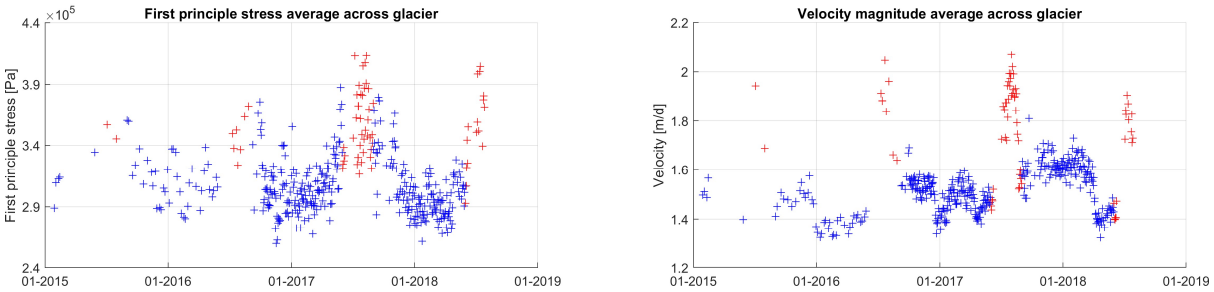

Figure 29 Left: First principle stress average over the floating part of the glacier from 2015 till August 2018. Right: Ice velocity magnitude from 2015 till August 2018. All panels: Only data with at least 75% of spatial coverage is used. Months: June, July and August are in red. The rest of the months are in blue.

5.3 Observed fractures and fracture propagation

On the Petermann glacier three main areas have been identified that show increased fracturing since 2014. In Figure 30 the fractures in these three locations are shown on the left with an overview of the Petermann glacier on the right. The fracture at location A started to form in July 2016, is located just south west of the main rift that is associated with the next major calving event by Münchow et al. (2016) and has grown by ~1.1 km between July 2016 and July 2018. In location B three fractures formed closely together over a stretch of ~4 km. The fractures at location B started to form in 2014, 2016 and 2018 respectively and their propagation is plotted in the bottom panel of Figure 30. Note that fracture 1 and 2 both formed during the month June, when the average tensile stress is high, while fracture 3 formed in March when the average tensile stress is still relatively low. Fracture 1 seems to have reached a stable length between 4 and 5 km while fracture 2 continued to increase in length, after a stable period in 2017, during the measurement period. The fracture in location C formed between 2015 and 2016. The fracture differs from the fractures in location A and B as it doubled in width, from ~30 m to ~60 m between 2016 and 2017 and only increase in length from 586 m to 676 m during the same period.

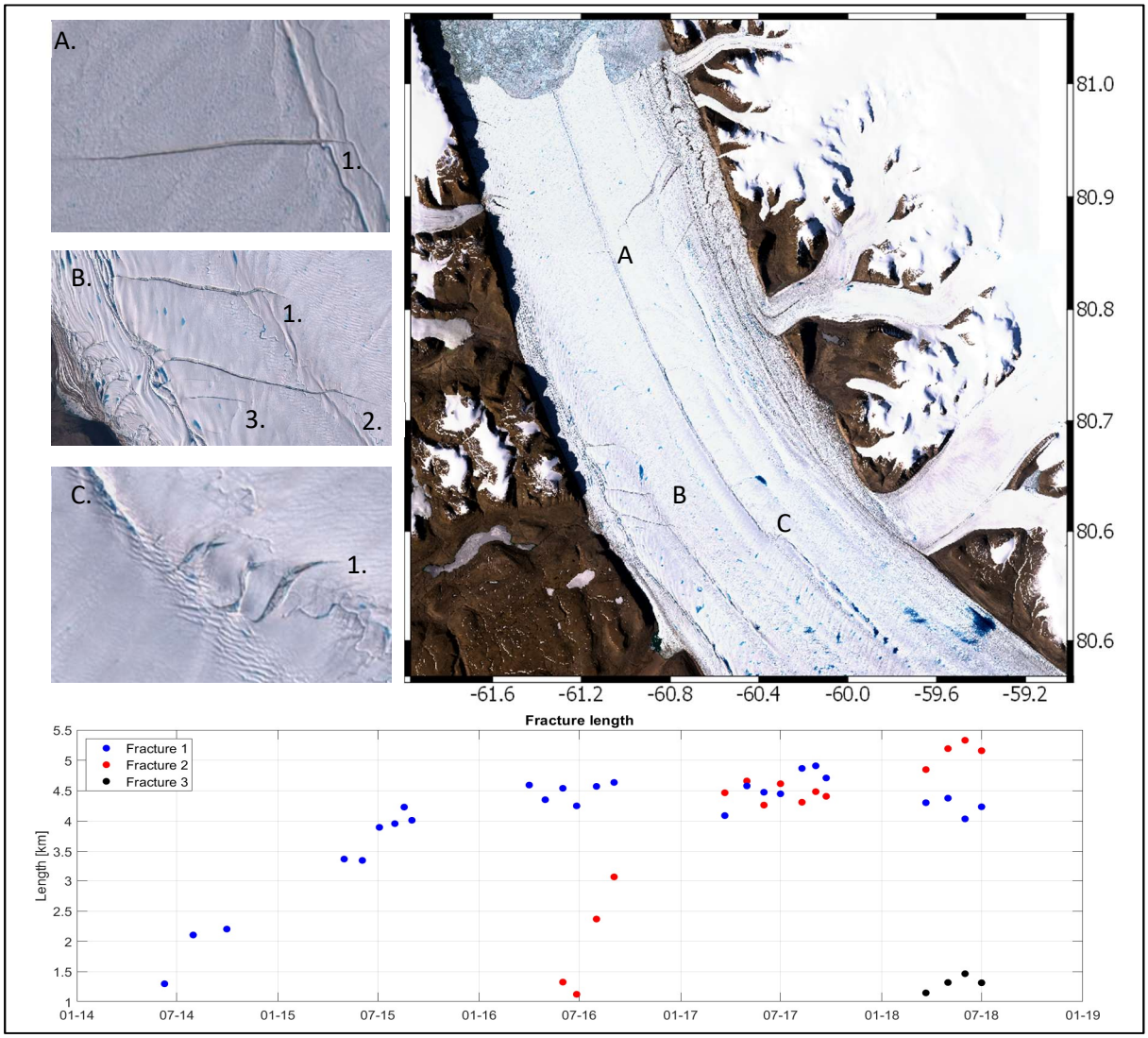

Figure 30 Top: Sentinel-2 images from 18-07-2018 of the Petermann glacier. Each zoom-in correspond to a location on the glacier where in since 2014 new fractures have appeared. Zoom-in B shows three separate fractures with each number located under the right tip of the respective fractures. The overview image has longitude on the horizontal and latitude on the vertical axes. Bottom: Fracture propagation of the three fractures shown in zoom-in B since fracture 1 started to form.

5.4 Linear Elastic Fracture Mechanics results

5.4.1 Comparison between observed and modelled crevasses

Figure 31 shows the Sentinel-1 backscatter of 21-09-2017 on the left and the crevasse depth over ice thickness ratio of the standard July 2017 scenario on the right. The Sentinel-1 backscatter image shows a high contrast between the large fractures in white and the surrounding glacier ice in blue. The fractures are predominantly located north east of the eastern channel and in fracture zone B. Relative high backscatter of ~-5 dB is visible along the central channel with the highest backscatter in fracture zone A and C.

The crevasse depth over ice thickness map of Figure 31 shows that crevasses with a relative high depth to thickness ratio, between 0.4 and 0.6, are common along the three channels and north east of the eastern channel. A crevasse depth over ice thickness of 1 means the crevasse penetrates the entire ice thickness and a crevasse depth over ice thickness of 0 means no propagation. In fracture zone B the crevasse depth to thickness ratio is not higher than on the surrounding western half of the ice shelf. With the exception of the locations where water is available the crevasse depth to thickness ratio lies between 0.1 and 0.3 in this area.

Comparison between the two images shows that not every location where fractures are visible on the image of the Sentinel-1 backscatter also show high crevasse depth to ice thickness ratios on the modelled map. The areas that do show a high crevasse depth to ice thickness ratios however are also locations that show signs of fracturing on the backscatter map. Also important to note is that the eastern and western ice shelf located on either side of the main channel shows no real signs of fracturing on the backscatter map while the modelled crevasse map indicates crevasse depth ratios between 0 and 0.3.

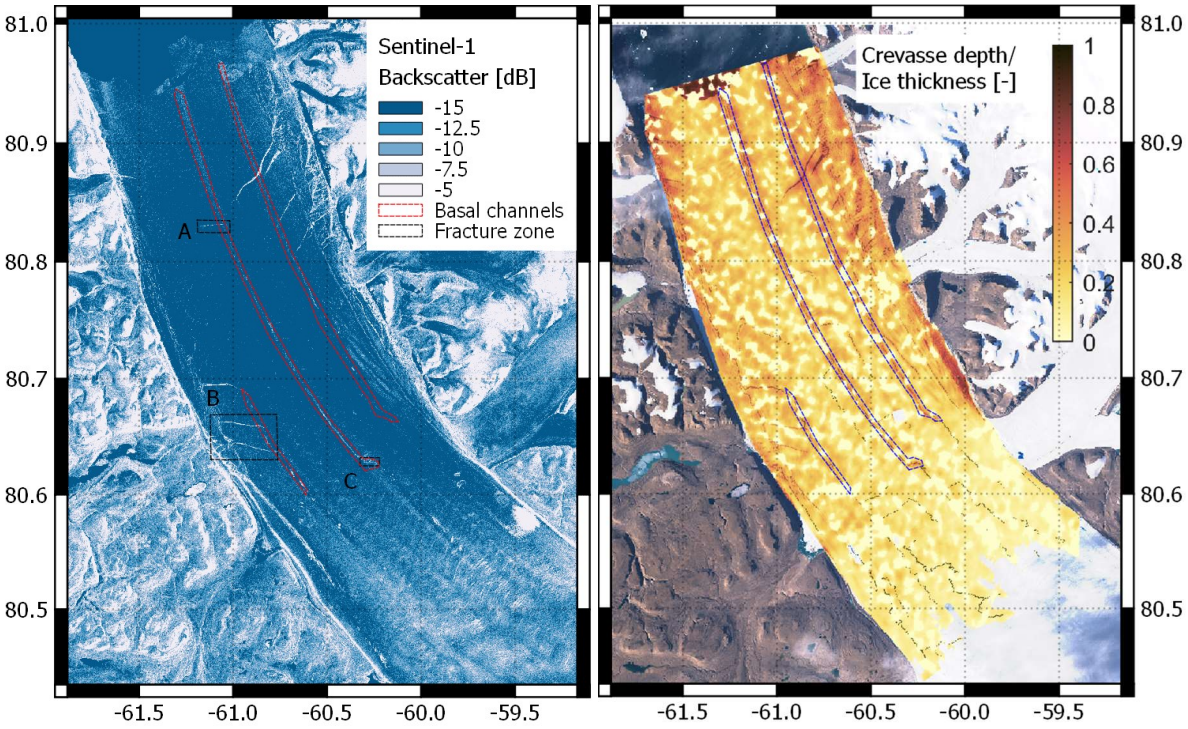

Figure 31 Left: Sentinel-1 backscatter from 21-09-2017 over Petermann glacier with latitude along vertical and longitude along horizontal axis. Right: Crevasse depth over ice thickness ratio with tensile stress and ice thickness from July 2017 and water level at locations where water is available set 5 m below the surface. Data overlies Aug-2016 Sentinel-2 image of the Petermann glacier with latitude along vertical and longitude along horizontal axis.

5.4.2 Effect of an increase in water

To show the effect of an increase in water availability on the crevasse depth over ice thickness ratio of the Petermann glacier the standard scenario of July 2017 with water is compared to the scenario of July 2017 with an increase in the locations that contain water. The difference map of Figure 32 panel on the right shows that the situation with additional water generates deeper crevasses compared to the situation where there is no water available along the central and eastern channels. Near the calving front the difference in crevasse depth over ice thickness is also showing some lateral channels between the western margin and the central channel. Noteworthy is that the increase is very concentrated and in most cases concentrated around locations where water was already available.

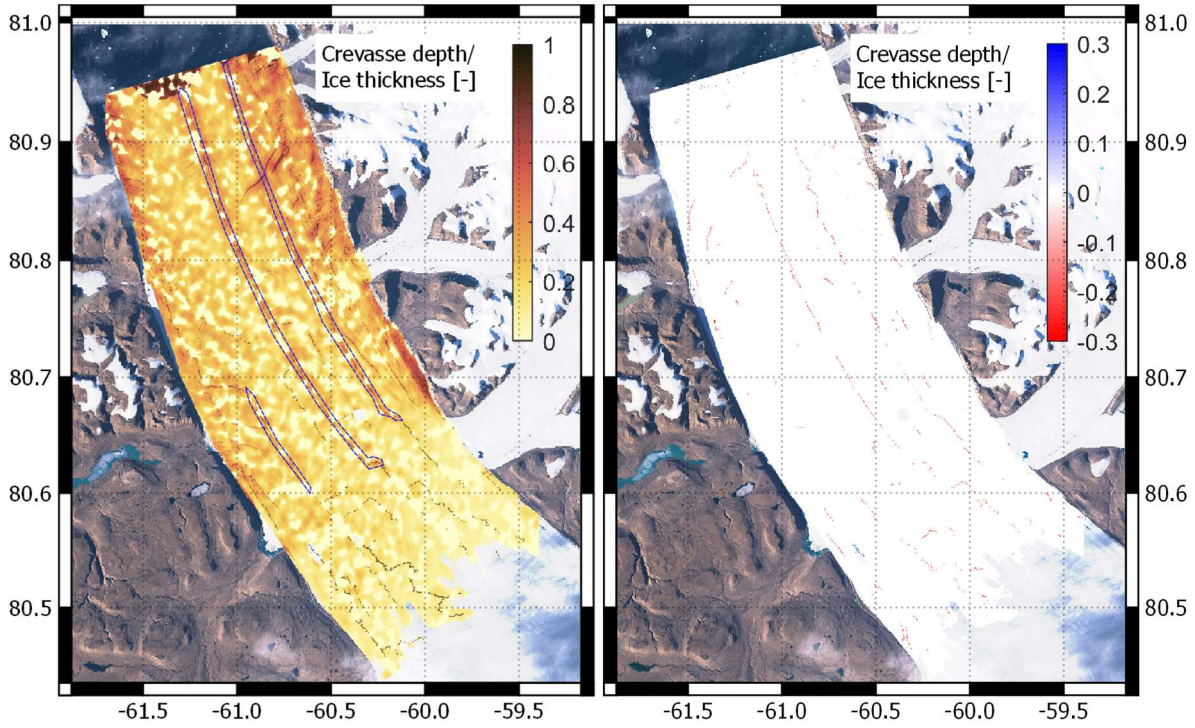

Figure 32 Comparison of LEFM model output for two different water levels. Left: Crevasse depth over ice thickness ratio with tensile stress and ice thickness from July 2017 and water level at locations where water is available set 5 m below the surface. Right: Crevasse depth over ice thickness ratio difference between the situation with water versus the situation without water

5.4.3 Effect of a reduction in ice thickness

In Figure 33 the effect of the reduction in ice thickness that took place between 2011 and 2017 and the extrapolated reduction between 2017 and 2020 on the relative crevasse depth over ice thickness is plotted. Figure 33 shows that the ratio of crevasse depth over thickness has increased most prominantly between 2011 and 2017 over the southern end of the central channel and along the southern end of the eastern margin by a ratio of approximately 0.25. Over the western channel the crevasse depth over ice thickness increased 0.05 and 0.12 during the 2011-2017 as well as the 2017-2020 period. The locations where the difference is green the ice shelf has completely disappeared due to the extended melt and no fracture propagation is possible. From both the difference maps of Figure 33 it also shows that the ambient parts around the central channel show little signs of additional fracturing and that the area near the calving front is less prone to an increase in fracturing due to thickness change compared to the floating ice shelf near the grounding line.

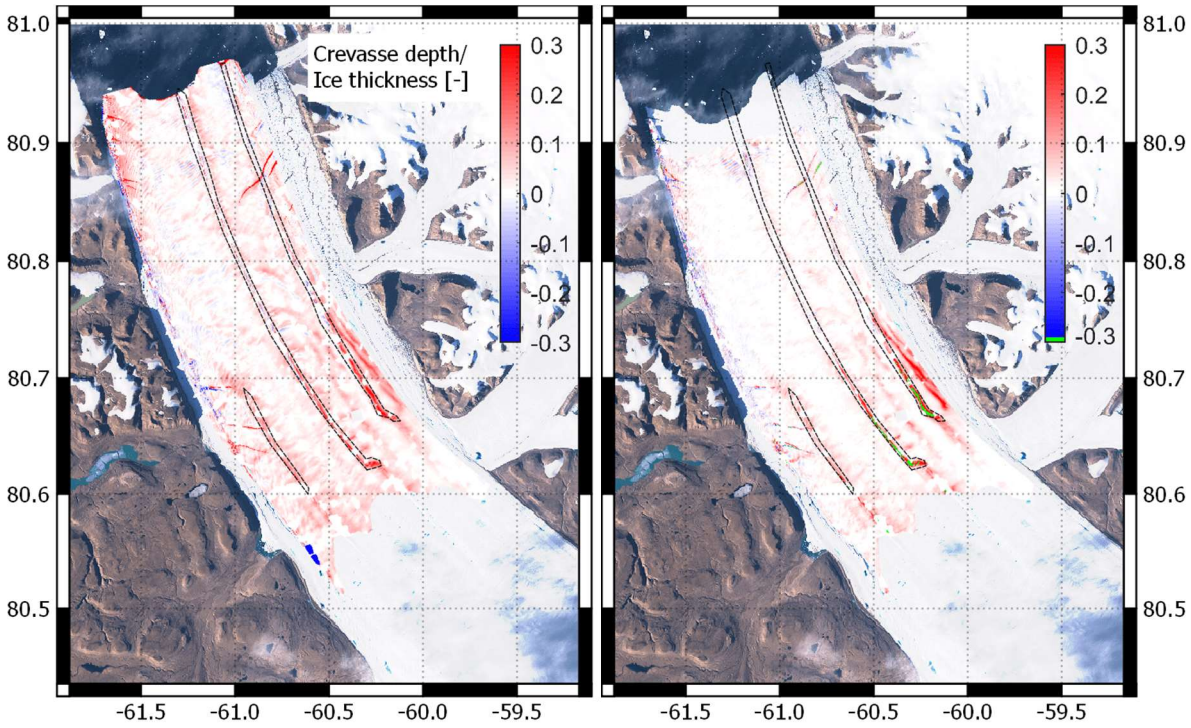

Figure 33 Left: Difference in crevasse depth over ice thickness between situation with 2017 ice thickness versus situation with ice thickness of 2011. Right: Difference in crevasse depth over ice thickness between the situation with 2017 ice thickness versus situation with ice thickness of 2020. Green corresponds to locations where the applied thickness change caused the ice thickness to fall below zero and no fracture propagation is possible.

5.4.4 Effect of a change in stress

In Figure 34 the ratio of crevasse depth over ice thickness is shown for the average January 2017 stress scenario is plotted on the left and the difference between the average July 2017 stress and average January 2017 stress scenario on the right. The difference between the July stress and January stress scenario shows an overall increase in the crevasse depth over ice thickness ratio over the entire glacier. The increase is strongest near the calving front where the crevasse depth over ice thickness ratio increases between 0.2 and 0.3. The crevasse depth over ice thickness ratio of the January stress scenario on the left shows almost no fracture propagation in these locations as the threshold for propagation is not met. Along the north east margin the crevasse depth over ice thickness ratio was already between 0.4 and 0.7 during the January scenario. At these locations only a small increase or even a decrease in crevasse depth over ice thickness ratio is observed.

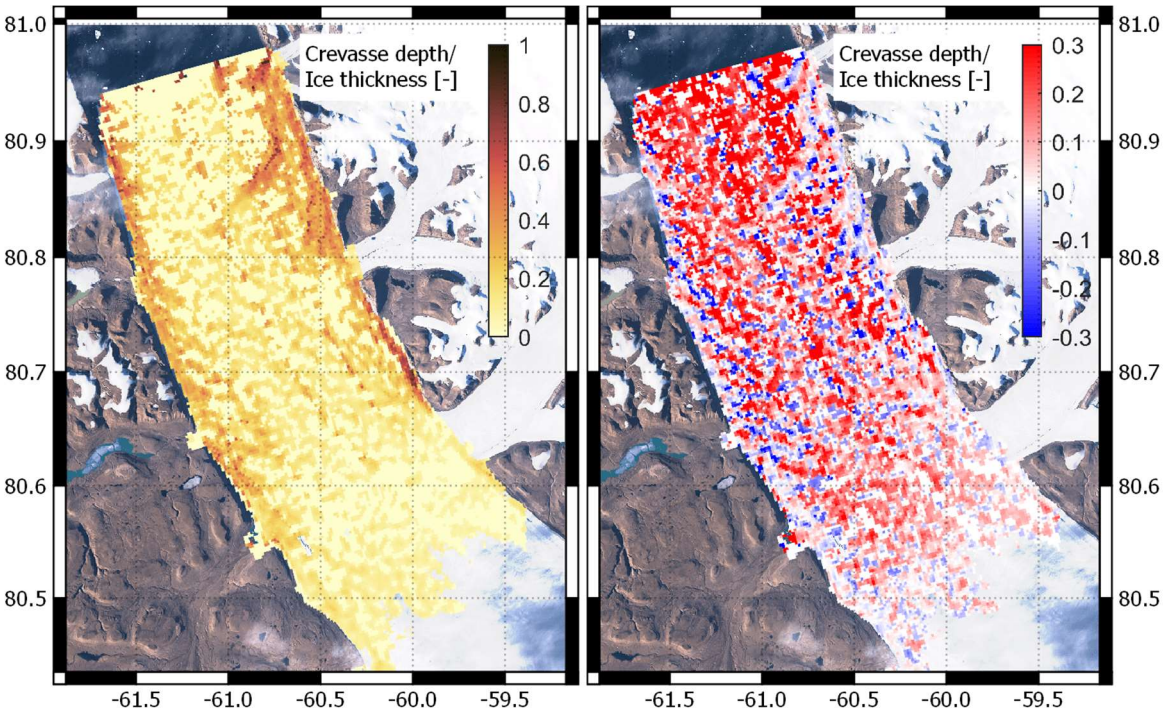

Figure 34 Left: Crevasse depth over ice thickness from winter situation without water availability. Right: Difference in crevasse depth over ice thickness between summer and winter situation

6. Discussion

6.1 Temperature and surface hydrology:

An increase in temperature can have an effect on the stability of the glacier as Münchow et al. (2016) expects the mass loss over the grounded and floating ice of the Petermann glacier to increase. This expectation is based on the long term trend in 2-m surface temperatures over the Greenland ice sheet reported by Hanna et al. (2013). Several papers describe the correlation between air temperature and glacier melt rate (Braithwaite 1981; Granger and Male 1978), but the level of correlation is location dependent according to Sicart et al. (2008). An increase in temperature can cause the altitude at which snow is still present during summer, also known as the snow line, to retreat (Naegeli et al. 2018). When bare ice is exposed after the snow line retreats less sunlight is reflected back causing an amplification of the melt rate, this process is also known as a positive albedo feedback (Naegeli et al. 2018). The increase in melt rate can in turn increase the surface water runoff.

An increase in surface water runoff can promote crevasse growth through hydrofracturing (Scambos, Hulbe, and Fahnestock 2013) and the increase in thinning ice shelf enhances the potential for calving (Bassis and Ma 2015). Besides thinning and hydrofracturing several papers have shown the influence of subglacial runoff on basal melt (Slater et al. 2016; Cowton et al. 2015). Subglacial runoff originates from melt water produced by basal sliding and surface runoff that reaches the base of the glacier through moulins, cracks and crevasses (Cai et al. 2017). The relative buoyant subglacial runoff plumes stimulate basal melt by transferring heat to the base of the ice shelf by increasing turbulent mixing (Slater et al. 2016).

6.1.1 Temperature

The average temperature of the HIRHAM5 model output is 1.52 K higher than the Alert average temperature and the HIRHAM5 linear trend is 0.024 K a^{-1} higher than the linear trend in the Alert temperature between January 1998 and January 2017. The correlation between the Alert and the AWS temperature is higher and the NRMSE is lower than the correlation and RMSE between the HIRHAM5 output and the AWS, 0.9887 versus 0.9858 and 5.4% versus 7.9 % respectively. Based on the correlation and NRSME the average temperature and linear trend on the Petermann glacier are assumed to be that of the Alert weather station: 256.48 K and 0.099 K a^{-1} respectively. Casey et al. (2017) reported trends in visible and near infra-red radiation albedo indicating the presence of increased melt conditions near Humboldt glacier, which is located approximately 140 km to the south west of the Petermann glacier. The observations on Humboldt glacier are in agreement with the observations on the Petermann glacier where the increase in temperature since 1998 is accompanied by an average increase in runoff of 200 mm a^{-1} since 2000. Thermal dampening, described in Lang and Braun (1990), could be the reason why the summer temperatures show no clear increase as the majority of the additional available energy is used by melting snow rather than heating the air temperature.

6.1.2 Drainage

The locations where hydrofracturing can occur are visualised by the drainage map. The drainage map shows the locations on the glacier where the runoff becomes concentrated and at which locations it flows of the glacier. For the drainage map only the runoff over the 2017 DEM was taken into account. Based on Macdonald et al. (2018) runoff from further upstream flows down to the floating ice shelf and increase the amount of surface water available. Including a DEM of the upstream part of the glacier could therefore increase the accuracy of the drainage map. Macdonald et al. (2018) showed the presence of glacial lakes over the Petermann glacier and that often these lakes are drained through hydrofracturing. The current drainage map does not capture the locations of these lakes and should therefore be considered as lower limit of locations that contain water for hydrofracturing and the area that these locations drain.

6.2 Thickness change and melt rates

Mapping the ice thickness is important for two reasons. First a reduction in ice thickness can promote crevasse growth (Dow et al. (2018) and Bassis et al. (2015)). A localised reduction in ice thickness in the form of (basal) channels promotes fracturing perpendicular to the flow direction (Dow et al. 2018). Dow et al. (2018) reports evidence that a major calving event on the Nansen ice shelf in Antarctica was a result of fracturing due to channelized thinning. Second the ice thickness of the Petermann glacier has an influence on its flow velocity (Hill et al. 2018). A thicker ice shelf has a larger surface area to generate friction between the fjord wall and the ice shelf compared to a thinner ice shelf. A reduction in ice thickness through surface or bottom melt can accelerate the flow velocity of the glacier by reducing the resistive stress along its margins and increase the mass loss from the GrIS (Hill et al. 2018).

6.2.1 Evolution of the thickness change rate

The results of the Eulerian thickness change rate between 2002 and 2011 along the West and the Central East flight line shows non-steady state thinning rate between -5 m a^{-1} and 0 m a^{-1}. The positive thickness change rate near the calving front between 0 m a^{-1} and 5 m a^{-1} is most likely due to temporal aliasing of thickness variations to which, the Eulerian reference frame is susceptible (Wilson et al. 2017). The Lagrangian thickness change rate between 2002 and 2011 is -20 m a^{-1} near the grounding line and decreases to a range between -5 m a^{-1} and 0 m a^{-1} near the calving front. The Lagrangian thickness change between 2002 and 2011 is approximately 20% lower than the steady state basal melt rate observed in 2002/2003 by Rignot and Steffen (2008). Rignot and Steffen (2008) included the thickness change due to ice divergence in the calculation of basal melt, which was assumed to be negligible following Münchow et al. (2014). The discrepancy could indicate that the ice divergence is in fact not negligible for the Petermann glacier or that the melt rate during 2002/2003 was higher than the average between 2002 and 2011.

The thickness change rate in the Eulerian reference frame shows thinning along the fracture zone along the West flight line after 2014. Results from the Eulerian reference frame should be interpreted with caution, but the Lagrangian thinning rate shows an increase in thickness change in this area as well making it very likely that the glacier was thinning between 2014 and 2017 by ~14 m a^{-1}. The surface elevation derived ice thickness map shows that the West flight line passes over the downstream part of the western channel and that the boundaries of the fracture zone match the boundary of the western channel. This means that the cavity in the fracture zone along the West flight line is actually the downstream tip of the western channel.

Along the Central East flight line the Eulerian thickness change between 2011 and 2013 shows a thickness change rate of approximately -15 m a^{-1} near the grounding line. The Lagrangian thickness

change rate however shows a thickness change between 0 and -10 m a^{-1} near the grounding line. Based on the Lagrangian thickness change the high Eulerian thickens change between 2011 and 2013 along the Central East flight line is therefore likely due to temporal aliasing.

Along the West and Central East flight lines the Lagrangian thickness change rate shows values up to -85 and -100 m a^{-1} respectively leading to the formation of deep basal crevasses. These extreme values are not uncommon as Münchow et al. (2014) observed a thickness change along the central channel of 300 m between 2007 and 2010. Vaughan et al. (2012) showed that on the Pine Island glacier basal crevasses similar to those on the Petermann glacier could lead to structural weakening of the floating ice shelf.

6.2.2 Average thickness change and basal melt rate

The thickness change rates over the entire glacier in an Eulerian reference frame are difficult to interpret and shows signs of strong temporal aliasing. These thickness change rates underline the necessity of working in a Lagrangian reference frame. The basal melt rates in a Lagrangian reference frame between 2011-2017 are very similar to the average basal melt rates between 2011 and 2015 Wilson et al. (2017) found. Basal melt rate values between 0 and 10 m a^{-1} are present near the calving front, which are not observed on the basal melt map of Wilson et al. (2017). These positive values are likely due to temporal aliasing and are not necessarily due to refreezing of ice. Wilson et al. (2017) used 97 DEMs acquired between 2011 and 2015 to calculate the basal melt. This appears to give better results due to a reduced influence of temporal aliasing as the time difference between the DEMs is lower.

Comparable to Wilson et al. (2017) basal melt rates of ~50 m a^{-1} near the grounding line and lower melt rates between 0 and 5 m a^{-1} are found near the calving front. The western, central and eastern channels that run parallel to the flow direction are therefore most likely formed near the grounding line and experience strongly reduced melt rates further downstream. An error source that is common for surface elevation derived ice thickness is that the basal melt rate in a Lagrangian and Eulerian reference frame can underestimate thinning over small scale basal crevasses as they are not always in hydrostatic equilibrium (Münchow et al. 2014).

6.3 Velocity and stress

Measuring the velocity on the Petermann glacier is important for two reasons. First the velocity combined with the ice thickness of the glacier determines the ice discharge. An increase in the flow velocity could therefore cause an increase in mass loss from the GrIS and eventually sea level rise (Hill et al. 2018). Second the stress on the glacier was calculated from the gradient in the velocity and according to Van der Veen (1998) the stress on the glacier causes crevasses to propagate. It is therefore important to establish whether an increase in the velocity on the Petermann glacier also causes an increase in the tensile stress and lead to an increase in fracturing.

6.3.1 Velocity transects

Rückamp et al. (2019) observed a velocity increase on the floating ice shelf of the Petermann glacier of approximately 10% between January/February 2012 and December 2016. They found that the 10% increase in velocity of was due to the 2012 calving event and the future calving event associated with the large fracture near the calving front. These results correspond well with the 9.6% and 9.4% observed increase in the velocity between the 1992-2011 and 2015-2018 average winter velocity observed at the northern and centre transect over the glacier. Rückamp et al. (2019) also showed that the increase in velocity mainly took place over the floating ice shelf and that the increase over the

grounded ice was minor, this difference in velocity increase is also visible in the difference between the South transect and the Centre and North transects.

The velocity gradient along the Centre velocity transect shows that that the Eastern and Western ice shelfs are moving faster than the central channel with a velocity difference of ~80 m a^{-1}. The velocity gradient disappears again over the North transect where the velocity is fairly uniform over the width of the glacier. The North transect is located over ice that Rückamp et al. (2019) suggests is already dynamically detached from the rest of the glacier which might explain why the flow velocity is more uniform here.

6.3.2 Inter annual velocity and stress variation

The average velocity time series over the glacier between January 2015 and August 2018 shows the intra-annual velocity variation as well as the tensile stress variation. Both the velocity and the tensile stress increase during the summer. This seasonal increase in velocity and stress is caused by enhanced basal sliding due to runoff that reaches the bed of the glacier according to Nick et al. (2012). The relation between velocity and stress also suggests that the possible future increase in the velocity due to calving reported by Hill et al. (2018) will increase the tensile stress on the glacier and thereby increase the chance of a subsequent calving event.

The dependence on the creep parameter A in Glen's flow law is the biggest source of uncertainty in the calculation of stress from strain as the creep parameter depends on temperature, water content, pressure and grain size (Cuffey and Paterson 2010). Rückamp et al. (2019) showed that the creep parameter varies with three orders of magnitude over the floating ice shelf. This would result in a factor 10 difference in stress with an equal level of strain. Assuming a constant value leads to an underestimation of the stress over the stiffer ice along the Western and Eastern ice shelf and an overestimation over the softer ice along the margins.

6.4 Observed fractures

Both the 2010 and 2012 calving events were the result of a large rift reaching the centre of the glacier (Münchow et al. 2016). Identifying the rifts that are currently forming on the glacier is therefore necessary to be able to say something about possible future calving events.

6.4.1 Zone A

The fracture in zone A formed in July 2016 and is associated with the next major calving event (Rückamp et al. 2019, Münchow et al. 2016). Fracture zone A is located on the central channel where the ice thickens is between 30 and 50 m. Dow et al. (2018) states that transverse fractures can be directly related to the formation of a basal channel and observed transverse fractures over a basal channel on the Nansen ice shelf. Dow et al. (2018) states that an increase in basal channelling could further weaken the ice shelf through the formation of these fractures.

6.4.2 Zone B

The fractures 1, 2 and 3 of zone B which initiated along the ice margin propagated through relative thick ice ~250 m to the western channel where the ice thickness has reduced to ~100 m. The propagation coincides with the reduction in ice thickness shown along the West flight line between 2011 and 2017 and along the western channel in the DEM derived Lagrangian thickness change. Bassis et al. (2015) modelled the influence of basal melt on surface crevassing and showed that basal crevasses, formed due to basal melt, can indeed trigger increased surface crevassing on a floating ice shelf. It is not certain however that the same principle applies here as the fractures in zone B are rifts

that propagated horizontally as opposed to the standard vertically propagating crevasses considered in the study of Bassis et al. (2015). The observations of Dow et al. (2018) indicate that transverse fractures can form due to basal channelling, but their focus lies on fractures that initiate from a basal channel instead of fractures that propagate towards a channel across relative thick ice. Applying a finite element model, similar to Plate (2015), to investigate what triggered these rifts to form and whether they are expected to increase in length even further would be recommended in order to predict the future of the Petermann glacier more accurately.

6.4.3 Zone C

Fracture zone C is located along the central channel precisely in the area where the ice thickness reduces significantly from ~250 m to 100 m. The fracture in zone C has a distinctively different shape compared to the fractures in zone A and B. The fractures in zone A and B are relative long and narrow whereas the fracture in zone C is relative short and wide. The western end of the fracture advanced further along the flow direction compared to the eastern end giving it a distinct S-shape. The central channel corresponds to the location where in the Central velocity transect a velocity gradient is visible after 2016, with a velocity difference of ~80 m a^{-1}, between the velocity in the channel and the velocity east of the channel. The S-shaped fracture started to form between 2015 and 2016 and doubled in width in 2017. The location of this fracture, its shape and the period in which it increased in size suggests that the ice shelf is fracturing in the centre due to a velocity gradient along the width of the glacier combined with a significant reduction in ice thickness at this location.

6.5 LEFM crevasse depth modelling

Ice shelf fractures are directly related to calving (Dow et al. 2018). Modelling whether fracturing will increase in the near future, based on the extrapolated current conditions, is needed to assess whether future calving events on the Petermann glacier are likely to take place. Considering the observed trend in runoff and the warming of deep water in the Nares Strait observed by Johnson et al. (2011) and Münchow et al. (2011) the atmospheric and oceanic conditions are likely to be favourable for additional fracturing. The significance of the different processes are investigated using the LEFM approach of Van der Veen (1998).

6.5.1 Sources of uncertainty

The LEFM crevasse depth model combines the stress, thickness and drainage results and shows the crevasse depth over ice thickness in four different experiments. The error sources related with the used input are also present in the crevasse depth over ice thickness ratio. The most prominent error sources are: the assumption of a constant creep parameter, fracture toughness and crevasse spacing, the ice thickness does not capture deep crevasses that are not in hydrostatic equilibrium and the drainage locations are likely an underestimate of the area where water is available for hydrofracturing.

The chosen creep parameter leads to an overestimation of the crevasse depth over ice thickness along the margins and an underestimation over the stiffer ice along the Western and Eastern ice shelf. With a variation of three orders of magnitude over the floating ice shelf, the creep parameter is the largest source of uncertainty. Using a variable creep parameter would therefore be recommended to improve the accuracy of the calculated crevasse depths.

The effect of a constant fracture toughness is more difficult to estimate as typical values range between 50 and 150 kPa $m^{1/2}$ (Petrovic 2003) and is dependent on: grain size, density, temperature, microstructure, water content and salt content (Cai et al. 2017). The chosen value of 100 kPa $m^{1/2}$ means that the fracture toughness can deviate ~50 kPa $m^{1/2}$ on the ice shelf as well as along the depth of the ice. Nixon and Schulson (1987) show that the fracture toughness increases by 40% when the

temperature reduces from -2 to -50 °C, however Petrovic (2003) finds a weak relation between fracture toughness and temperature. Determining the fracture toughness by taking ice samples from the Petermann glacier is recommended to improve the accuracy of the calculated crevasse depth.

The background section on LEFM shows the influence of crevasse spacing. A difference in spacing can mean the difference between a minor propagation and fractures propagation the entire ice thickness. Using high spatial resolution ~0.5 m satellite imagery to identify crevasse spacing and allowing the crevasse spacing to vary over the ice shelf is recommended to improve the accuracy of the calculated crevasse depths.

The effect of a deep crevasse which is not in hydrostatic equilibrium leads to an overestimation of the ice thickness and generally an underestimate of the crevasse depth over ice thickness ratio. The effect is likely influencing the crevasse depth over ice thickness ratio near the grounding line where large basal undulations were observed.

6.5.2 Experiments

The crevasse depth over ice thickness ratio of experiment 1 shows crevasses nearly everywhere on the ambient ice shelf with a crevasse depth over ice thickness ratio of ~0.25. Based on the Landsat-8 images and the Sentinel-1 backscatter these crevasse depths, which are around 50 m with an average ice thickness of 200 m, are most likely an overestimation due to an overestimation of the stress applied or underestimation of the fracture toughness in the model. Additionally discrepancies between the observed fractures in the Sentinel-1 backscatter map are possibly due to the fact that the LEFM crevasse model only uses mode 1 fracturing while in reality fractures are often formed due to mixed mode stress configurations where both tensile stress and shear stress combined cause a fracture to propagate (Colgan et al. 2016). Combined with the assumptions on fracture toughness, creep parameter and crevasse spacing these discrepancies mean that the modelled crevasse depth over ice thickness ratio should not be interpreted as an accurate representation of the crevasse field on the Petermann glacier. The modelled crevasse maps merely indicate in which areas (increased) vertical crevasse propagation is likely to happen considering the imposed settings and whether the conditions for fracturing will become more favourable in the future.

Since the runoff shows a positive linear trend it is likely that the average runoff is going to increase further in the future and higher daily runoff rates will be reached more often. The overall effect of the increase in runoff is mainly limited to the basal channels parallel to the flow direction. No major increase in crevasse depth across the glacier is visible. This could indicate that the runoff will not play a major role in allowing fractures to propagate over the thicker ambient ice shelf, but further enhance the possibility of fractures forming in the channels such as in fracture zone A and C.

The effect of the decrease in ice thickness between 2017 and 2020 is most noticeable along the three channels running parallel to the flow direction. If indeed the fractures in fracture zone B are the results of thinning along the eastern channel the conditions for those fractures to propagate further and cross the thicker ice between the eastern and central channel will become more favourable between 2017 and 2020. The eastern channel shows a strong increase in crevasse depth over ice thickness ratio, while in this region, as the sentinel-1 backscatter shows, extensive fracturing is currently not observed. The strong increase in crevasse depth over ice thickness due to thinning along the eastern channel indicates conditions for the formation of similar fractures to the fractures which have formed along the western channel will increase.

The difference in crevasse depth between the winter and summer stress state shows that an increase in stress of ~25% increases the crevasse depth over ice thickness significantly over the entire floating ice shelf. A velocity increase of ~25% is predicted to occur after the Petermann glacier loses approximately 20 km of its ice shelf relative to the current calving front by Hill et al. (2018). This

indicates that according to the LEFM model when the ice shelf reduces in length beyond 20 km the conditions for further fracturing are promoted.

7. Conclusions

The Petermann glacier is the fourth largest glacier in Greenland (Rignot and Kanagaratnam 2006) and drains approximately 12 Gt of ice from the Greenland Ice Sheet per year (Rignot and Steffen, 2008). During the past decade the glacier has lost ~40% of its floating ice shelf in two large calving events (Nick et al. 2012) and what is left is threatened as both air and ocean temperatures are increasing (Hanna et al. 2008, Johnson et al. 2011, Münchow et al. 2011). A collapse of the entire floating ice shelf could increase the ice discharge and the contribution of the Petermann glacier to global sea level rise significantly (Hill et al. 2018). Here the main research question: "how long will it approximately take before the floating ice shelf of the Petermann glacier collapses?" is answered based on the extrapolated conditions between 2017 and 2020.

7.1 Temperature and surface hydrology

On average the temperature over the Petermann glacier is increasing by 0.099 K a^{-1} since 1998. The increase in temperature is accompanied by a linear trend in the runoff which is strongest over the grounded part of the glacier and increased the runoff on average by approximately 200 mm weq a^{-1}. An increase in runoff is expected to enhance basal melting although further research is needed to fully understand the ocean ice interaction of the Petermann glacier (Münchow et al. 2016). 81% of the runoff is drained from the glacier either at the calving front or at the glacier margins. The remaining 19% is either drained through hydrofracturing or refreezes in during the winter (Macdonald et al. 2018).

7.2 Thickness change and melt rates

West of the central channel a new channel has formed due to basal melt rates of ~14 m a^{-1}. Increased thickness change started between 2001 and 2011 and increased further between 2014 and 2017. Near the grounding line large basal crevasses formed west of the central channel between 2002 and 2017 due to thickness change rates exceeding 80 m a^{-1}. Over the eastern ice shelf several large basal crevasses formed between 2011 and 2017. In some cases these crevasses reduce the ice thickness locally from ~360 m to ~120 m. On average 81% of the thickness change is due to basal melt, which is high near the grounding line ~50 m a^{-1} and lower near the calving front between 0 and 5 m a^{-1}. The high basal melt rates carve out deep basal channels that run parallel to the flow direction. The stability of the glacier is expected to reduce due to the presence of basal channels and crevasses as they can enhance the formation of transverse and vertical crevasses (Bassis and Ma 2015; Dow et al. 2018).

7.3 Velocity and stress

Comparison of the average velocity between 1992-2010 and 2015-2018 showed an increase in the winter velocity along the Northern and Central transects across the glacier of ~9%. Rückamp et al. (2019) showed that this increase followed the 2012 calving event and is a precursor to the anticipated next calving event. Across the centre of the glacier a velocity gradient developed after 2016 as the thicker ice on either side of the central channel experienced an increase in velocity relative to the central channel of ~80 m a^{-1}. The gradient is not present over the ice near the calving front. Rückamp et al. (2019) suspects this ice to be already dynamically detached from the main floating ice shelf which possibly explains the uniform flow velocity.

The tensile stress increases during the summer months following the increase in velocity. Nick et al. (2012) showed that the summer velocity increases due to subglacial runoff enhanced basal lubrication. Hill et al. (2018) showed that an increase in velocity will follow if the Petermann glacier retreats approximately 20 km behind the current calving front. The increase in velocity during the summer followed by an increase in the tensile stress indicates that further retreat of the glacier could increase the tensile stress on the glacier as well.

7.4 Fracturing due to channelized bottom melt and velocity gradients

The fracture in fracture zone A is associated with the next calving event by Münchow et al. (2016) and Rückamp et al. (2019). Calving is likely to happen when the main rift reaches the centre and connects with the fracture in fracture zone A as the 2010 and 2012 calving events were triggered by a large rift reaching the centre of the glacier (Münchow et al. 2016).

In the region where the western basal channel has formed between 2011 and 2017 three new fractures have formed between 2014 and 2018. Of these three fractures two propagated from the ice sheet margin through relative thick ice of ~250 m to the western channel where the ice thickness is ~100 m. The propagation of these fractures indicates that at least one fracture shows no sign it reached its final length and will possibly continue to increase in length even further. Calving is associated with a fracture propagating from the glacier margin to the centre (Münchow et al. 2016) therefore ~2/3 of the glacier could calve if one of these fractures reaches the centre. Although research by Dow et al. (2018) and Bassis et al. (2015) show that the formation of basal crevasses and channels can enhance fracturing the mechanism that drives the propagation of the fractures in fracture zone B is not yet understood well enough to predict future fracture propagation. Fracture modelling using a finite element model would be recommended in order understand the process that drives fracture propagation in this region.

A distinct S-shaped fracture in an area where the ice thickness reduces to ~100 m is likely formed due to a lateral velocity gradient across the glacier. It is difficult to predict what the implications are of this fracture on the stability of the glacier as most research is performed on calving due to transverse fractures opposed to longitudinal fractures.

7.5 Crevasse depth modelling based on future scenarios

Crevasse depth modelling using the LEFM model based on Van der Veen (1998b) over the Petermann glacier has considerable short comings. The heavy reliance on parameters such the creep parameter, fracture toughness and crevasse spacing which can vary over the glacier significantly means that the result should not be interpreted as an accurate approximation of the crevasse depth on the glacier. The relative low computational costs and easy implementation however make it a useful tool to

investigate what the effect is of certain processes are on fracture propagation over the entire floating ice shelf.

Increasing the runoff from the average of the melt season to the maximum value shows that the effect of the increase is not strong enough to enable hydrofracturing across the thick western and eastern ice shelf and is expected to slightly enhance hydrofracturing along several channels running parallel to the flow direction. This indicates that the runoff will probably not play a key role in triggering calving by allowing a fracture to reach the centre.

Extrapolating the average thickness change between 2011 and 2017 to 2020 shows that increased fracture propagation is expected along the three channels running parallel to the flow direction. Due to the extended thickness change the ice thickness along the central channel and parts of the eastern channel will have been reduced to zero making fracture propagation impossible. The strong increase in crevasse depth over ice thickness due to thinning along the eastern channel indicates favourable conditions for fracture propagation. The change in ice thickness seems to have no significant effect on the relative thick eastern and western ice shelf between the channels.

The seasonal increase in velocity of ~25% leads to an increase in the crevasse depth over ice thickness ratio over nearly the entire floating ice shelf. The increase in velocity and therefore stress causes crevasses to propagate approximately ~0.3 of the glacier in locations where in the low stress situation no propagation was observed. A velocity increase of ~25% is predicted to occur after the Petermann glacier loses approximately 20 km of its ice shelf relative to the current calving front by Hill et al. (2018) indicating that extended retreat of the glacier would enable more crevasses to propagate over the entire floating ice shelf.

7.6 Future stability of the Petermann glacier

Increasing runoff and thinning along several channels along the glacier combined with extensive fracturing far behind the calving front indicates that the Petermann glacier has not reached an equilibrium position. The gradient in the velocity across the glacier likely initiated fracturing in the central channel, but further research is needed to understand the effect on the long term stability. How long it will take for the floating ice shelf to collapse will depend on whether the melt rate will continue to reduce the thickness along the channels and whether the fractures in zone B will reach the central channel. Based on the extrapolated average thickness change rate between 2011 and 2017 the thickness will continue to decrease along the three channels on the glacier. Conditions are likely to be more favourable for crevasse propagation due to the reduction in ice thickness and increase in the water available for hydrofracturing. Stress levels are expected to increase following the speed up after the calving front retreated more than 20 km behind the current calving front. Based on the findings in this thesis the floating ice shelf of the Petermann glacier is expected to collapse within the next decade if the current conditions are an indication for the future. Collapse of the ice sheet will lead to more than a doubling in ice flux across the grounding line and cause a substantial increase in the Petermann glacier's contribution to global sea level rise according to Hill et al. (2018).

8. Bibliography

Allen, Chris. 2010. “IceBridge MCoRDS L2 Ice Thickness, Version 1.” NASA National Snow and Ice Data Center Distributed Active Archive Center. https://doi.org/10.5067/GDQ0CUCVTE2Q.

———. 2011. “Pre-IceBridge MCoRDS L2 Ice Thickness, Version 1.” NASA National Snow and Ice Data Center Distributed Active Archive Center. https://doi.org/10.5067/QKMTQ02C2U56.

AMAP. 2017. *Snow, Water, Ice and Permafrost in the Arctic (SWIPA) 2017*. Oslo, Norway: Arctic Monitoring and Assessment Programme.

Babiker, Mohamed, and Martin W. Miles. 2013. “Unprecedented Retreat in a 50-Year Observational Record for Petermann Glacier, North Greenland AU - Johannessen, Ola M.” *Atmospheric and Oceanic Science Letters* 6 (5): 259–65. https://doi.org/10.3878/j.issn.1674-2834.13.0021.

Bamber, J. L., M. J. Siegert, J. A. Griggs, S. J. Marshall, and G. Spada. 2013. “Paleofluvial Mega-Canyon Beneath the Central Greenland Ice Sheet.” *Science* 341 (6149): 997–99. https://doi.org/10.1126/science.1239794.

Bassis, J.N., and Y. Ma. 2015. “Evolution of Basal Crevasses Links Ice Shelf Stability to Ocean Forcing.” *Earth and Planetary Science Letters* 409 (January): 203–11. https://doi.org/10.1016/j.epsl.2014.11.003.

Braithwaite, Roger J. 1981. “On Glacier Energy Balance, Ablation, and Air Temperature.” *Journal of Glaciology* 27 (97): 381–91. https://doi.org/10.3189/S0022143000011424.

Cai, Cilan, Eric Rignot, Dimitris Menemenlis, and Yoshihiro Nakayama. 2017. “Observations and Modeling of Ocean-Induced Melt beneath Petermann Glacier Ice Shelf in Northwestern Greenland: MELTING PETERMANN ICE SHELF.” *Geophysical Research Letters* 44 (16): 8396–8403. https://doi.org/10.1002/2017GL073711.

Carr, J. Rachel, Andreas Vieli, and Chris Stokes. 2013. “Influence of Sea Ice Decline, Atmospheric Warming, and Glacier Width on Marine-Terminating Outlet Glacier Behavior in Northwest Greenland at Seasonal to Interannual Timescales: CONTROLS OF OUTLET GLACIER BEHAVIOR.” *Journal of Geophysical Research: Earth Surface* 118 (3): 1210–26. https://doi.org/10.1002/jgrf.20088.

Casey, Kimberly A., Chris M. Polashenski, Justin Chen, and Marco Tedesco. 2017. “Impact of MODIS Sensor Calibration Updates on Greenland Ice Sheet Surface Reflectance and Albedo Trends.” *The Cryosphere* 11 (4): 1781–95. https://doi.org/10.5194/tc-11-1781-2017.

Colgan, William, Harihar Rajaram, Waleed Abdalati, Cheryl McCutchan, Ruth Mottram, Mahsa S. Moussavi, and Shane Grigsby. 2016. “Glacier Crevasses: Observations, Models, and Mass Balance Implications: Glacier Crevasses.” *Reviews of Geophysics* 54 (1): 119–61. https://doi.org/10.1002/2015RG000504.

Cook, S., I. C. Rutt, T. Murray, A. Luckman, T. Zwinger, N. Selmes, A. Goldsack, and T. D. James. 2014. “Modelling Environmental Influences on Calving at Helheim Glacier in Eastern Greenland.” *The Cryosphere* 8 (3): 827–41. https://doi.org/10.5194/tc-8-827-2014.

Cowton, Tom, Donald Slater, Andrew Sole, Dan Goldberg, and Peter Nienow. 2015. “Modeling the Impact of Glacial Runoff on Fjord Circulation and Submarine Melt Rate Using a New Subgrid-Scale Parameterization for Glacial Plumes.” *Journal of Geophysical Research: Oceans* 120 (2): 796–812. https://doi.org/10.1002/2014JC010324.

Cuffey, Kurt, and W. S. B. Paterson. 2010. *The Physics of Glaciers*. 4th ed. Burlington, MA: Butterworth-Heinemann/Elsevier.

Dow, Christine F., Won Sang Lee, Jamin S. Greenbaum, Chad A. Greene, Donald D. Blankenship, Kristin Poinar, Alexander L. Forrest, Duncan A. Young, and Christopher J. Zappa. 2018. "Basal Channels Drive Active Surface Hydrology and Transverse Ice Shelf Fracture." *Science Advances* 4 (6). https://doi.org/10.1126/sciadv.aao7212.

Egbert, Gary D., and Svetlana Y. Erofeeva. 2002. "Efficient Inverse Modeling of Barotropic Ocean Tides." *Journal of Atmospheric and Oceanic Technology* 19 (2): 183–204. https://doi.org/10.1175/1520-0426(2002)019<0183:EIMOBO>2.0.CO;2.

Enderlin, E. M., and T. C. Bartholomaus. 2019. "Poor Performance of a Common Crevasse Model at Marine-Terminating Glaciers." *The Cryosphere Discuss.* 2019 (June): 1–19. https://doi.org/10.5194/tc-2019-128.

Gade, Herman G. 1979. "Melting of Ice in Sea Water: A Primitive Model with Application to the Antarctic Ice Shelf and Icebergs." *Journal of Physical Oceanography* 9 (1): 189–98. https://doi.org/10.1175/1520-0485(1979)009<0189:MOIISW>2.0.CO;2.

Granger, R. J., and D. H. Male. 1978. "Melting of a Prairie Snowpack." *Journal of Applied Meteorology* 17 (12): 1833–42.

Griffith, A. A. 1921. "The Phenomena of Rupture and Flow in Solids." *Philosophical Transactions of the Royal Society A: Mathematical, Physical and Engineering Sciences* 221 (582–593): 163–98. https://doi.org/10.1098/rsta.1921.0006.

Hanna, Edward, Philippe Huybrechts, Konrad Steffen, John Cappelen, Russell Huff, Christopher Shuman, Tristram Irvine-Fynn, Stephen Wise, and Michael Griffiths. 2008. "Increased Runoff from Melt from the Greenland Ice Sheet: A Response to Global Warming." *Journal of Climate* 21 (2): 331–41. https://doi.org/10.1175/2007JCLI1964.1.

Hanna, Edward, Francisco J. Navarro, Frank Pattyn, Catia M. Domingues, Xavier Fettweis, Erik R. Ivins, Robert J. Nicholls, et al. 2013. "Ice-Sheet Mass Balance and Climate Change." *Nature* 498 (7452): 51–59. https://doi.org/10.1038/nature12238.

Higgins, A. K. 1991. *North Greenland Glacier Velocities and Calf Ice Production*. Vol. 60. 1. Bremerhaven: Alfred Wegener Institute for Polar and Marine Research & German Society of Polar Research.

Hill, Emily A., G. Hilmar Gudmundsson, J. Rachel Carr, and Chris R. Stokes. 2018. "Velocity Response of Petermann Glacier, Northwest Greenland to Past and Future Calving Events." *The Cryosphere Discussions*, September, 1–21. https://doi.org/10.5194/tc-2018-162.

Irwin, George R. 1947. "Fracture Dynamics." *Fracturing of Metals*.

———. 1957. "Analysis of Stresses and Strains Near the End of a Crack Traversing a Plate" J. Appl. Mech.

J. F. Nye. 1957. "The Distribution of Stress and Velocity in Glaciers and Ice-Sheets." *Proceedings of the Royal Society of London. Series A. Mathematical and Physical Sciences* 239 (1216): 113–33. https://doi.org/10.1098/rspa.1957.0026.

Johannessen, O. M., M. Babiker, and M. W. Miles. 2011. "Petermann Glacier, North Greenland: Massive Calving in 2010 and the Past Half Century." *The Cryosphere Discussions* 5 (1): 169–81. https://doi.org/10.5194/tcd-5-169-2011.

Johannessen, Ola M., Mohamed Babiker, and Martin W. Miles. 2013. "Unprecedented Retreat in a 50-Year Observational Record for Petermann Glacier, North Greenland." *Atmospheric and Oceanic Science Letters* 6 (5): 259–65. https://doi.org/10.3878/j.issn.1674-2834.13.0021.

Johnson, H. L., A. Münchow, K. K. Falkner, and H. Melling. 2011. "Ocean Circulation and Properties in Petermann Fjord, Greenland." *Journal of Geophysical Research* 116 (C1). https://doi.org/10.1029/2010JC006519.

Kollmeyer, Ronald C. 1980. "West Greenland Outlet Glaciers: An Inventory of the Major Iceberg Producers." *Cold Regions Science and Technology* 1 (3–4): 175–81. https://doi.org/10.1016/0165-232X(80)90046-4.

Krug, J., J. Weiss, O. Gagliardini, and G. Durand. 2014. “Combining Damage and Fracture Mechanics to Model Calving.” *The Cryosphere* 8 (6): 2101–17. https://doi.org/10.5194/tc-8-2101-2014.

Lang, H., and L. Braun. 1990. “On the Information Content of Air Temperature in the Context of Snow Melt Estimation.” *IAHS Publ* 190: 347–54.

Langen, P. L., R. H. Mottram, J. H. Christensen, F. Boberg, C. B. Rodehacke, M. Stendel, D. van As, et al. 2015. “Quantifying Energy and Mass Fluxes Controlling Godthåbsfjord Freshwater Input in a 5-Km Simulation (1991–2012).” *Journal of Climate* 28 (9): 3694–3713. https://doi.org/10.1175/JCLI-D-14-00271.1.

Langen, Peter L., Robert S. Fausto, Baptiste Vandecrux, Ruth H. Mottram, and Jason E. Box. 2017. “Liquid Water Flow and Retention on the Greenland Ice Sheet in the Regional Climate Model HIRHAM5: Local and Large-Scale Impacts.” *Frontiers in Earth Science* 4 (January). https://doi.org/10.3389/feart.2016.00110.

Larour, E., Rignot, E., and Aubry, D. 2004. “Modelling of Rift Propagation on Ronne Ice Shelf, Antarctica, and Sensitivity to Climate Change.” *Geophysical Research Letters* 31 (16). https://doi.org/10.1029/2004GL020077.

Macdonald, Grant J., Alison F. Banwell, and Douglas R. MacAyeal. 2018. “Seasonal Evolution of Supraglacial Lakes on a Floating Ice Tongue, Petermann Glacier, Greenland.” *Annals of Glaciology* 59 (76pt1): 56–65. https://doi.org/10.1017/aog.2018.9.

Moon, T., I. Joughin, B. Smith, and I. Howat. 2012. “21st-Century Evolution of Greenland Outlet Glacier Velocities.” *Science* 336 (6081): 576–78. https://doi.org/10.1126/science.1219985.

Mottram, Ruth H., and Douglas I. Benn. 2009. “Testing Crevasse-Depth Models: A Field Study at Breiðamerkurjökull, Iceland.” *Journal of Glaciology* 55 (192): 746–52. https://doi.org/10.3189/002214309789470905.

Münchow, Andreas, Kelly Falkner, Humfrey Melling, Berit Rabe, and Helen Johnson. 2011. “Ocean Warming of Nares Strait Bottom Waters Off Northwest Greenland, 2003–2009.” *Oceanography* 24 (3): 114–23. https://doi.org/10.5670/oceanog.2011.62.

Münchow, Andreas, Laurie Padman, and Helen A. Fricker. 2014a. “Interannual Changes of the Floating Ice Shelf of Petermann Gletscher, North Greenland, from 2000 to 2012.” *Journal of Glaciology* 60 (221): 489–499. https://doi.org/10.3189/2014JoG13J135.

———. 2014b. “Interannual Changes of the Floating Ice Shelf of Petermann Gletscher, North Greenland, from 2000 to 2012.” *Journal of Glaciology* 60 (221): 489–99. https://doi.org/10.3189/2014JoG13J135.

Münchow, Andreas, Laurie Padman, Peter Washam, and Keith Nicholls. 2016. “The Ice Shelf of Petermann Gletscher, North Greenland, and Its Connection to the Arctic and Atlantic Oceans.” *Oceanography* 29 (4): 84–95. https://doi.org/10.5670/oceanog.2016.101.

Nick, F.M., A. Luckman, A. Vieli, C.J. Van Der Veen, D. Van As, R.S.W. Van De Wal, F. Pattyn, A.L. Hubbard, and D. Floricioiu. 2012. “The Response of Petermann Glacier, Greenland, to Large Calving Events, and Its Future Stability in the Context of Atmospheric and Oceanic Warming.” *Journal of Glaciology* 58 (208): 229–39. https://doi.org/10.3189/2012JoG11J242.

Nick, F.M., C.J. Van Der Veen, A. Vieli, and D.I. Benn. 2010. “A Physically Based Calving Model Applied to Marine Outlet Glaciers and Implications for the Glacier Dynamics.” *Journal of Glaciology* 56 (199): 781–94. https://doi.org/10.3189/002214310794457344.

Nixon, W. A., and E. M. Schulson. 1987. “A Micromechanical View of the Fracture Toughness of Ice.” *Le Journal de Physique Colloques* 48 (C1): C1-313-C1-319.

Noh, Myoung-Jong, and Ian M. Howat. 2017. “The Surface Extraction from TIN Based Search-Space Minimization (SETSM) Algorithm.” *ISPRS Journal of Photogrammetry and Remote Sensing* 129 (July): 55–76. https://doi.org/10.1016/j.isprsjprs.2017.04.019.

Petrovic, J. J. 2003. “Review Mechanical Properties of Ice and Snow.” *Journal of Materials Science* 38 (1): 1–6. https://doi.org/10.1023/A:1021134128038.

Plate, Carolin. 2015. *Fracture Mechanical Analysis of Failure Processes in Antarctic Ice Shelves*. Forschungsbericht / Technische Universität Kaiserslautern, Lehrstuhl Für Technische Mechanik 11. Kaiserslautern: Techn. Univ., Lehrstuhl für Techn. Mechanik.

Porter, Claire, Paul Morin, Ian Howat, Myoung-Jon Noh, Brian Bates, Kenneth Peterman, Scott Keesey, et al. 2018. "ArcticDEM." Harvard Dataverse. https://doi.org/10.7910/DVN/OHHUKH.

Reeh, Niels, Christoph Mayer, Ole B. Olesen, Erik Lintz Christensen, and Henrik Højmark Thomsen. 2000. "Tidal Movement of Nioghalvfjerdsfjorden Glacier, Northeast Greenland: Observations and Modelling." *Annals of Glaciology* 31: 111–17. https://doi.org/10.3189/172756400781820408.

Rignot, E., J. E. Box, E. Burgess, and E. Hanna. 2008a. "Mass Balance of the Greenland Ice Sheet from 1958 to 2007." *Geophysical Research Letters* 35 (20). https://doi.org/10.1029/2008GL035417.

———. 2008b. "Mass Balance of the Greenland Ice Sheet from 1958 to 2007." *Geophysical Research Letters* 35 (20). https://doi.org/10.1029/2008GL035417.

Rignot, E., and K. Steffen. 2008. "Channelized Bottom Melting and Stability of Floating Ice Shelves." *Geophysical Research Letters* 35 (2). https://doi.org/10.1029/2007GL031765.

Rignot, Eric. 1996. "Tidal Motion, Ice Velocity and Melt Rate of Petermann Gletscher, Greenland, Measured from Radar Interferometry." *Journal of Glaciology* 42 (142): 476–85. https://doi.org/10.3189/S0022143000003464.

Rignot, Eric, Michele Koppes, and Isabella Velicogna. 2010. "Rapid Submarine Melting of the Calving Faces of West Greenland Glaciers." *Nature Geoscience* 3 (February): 187.

Rist, M. A., P. R. Sammonds, S. A. F. Murrell, P. G. Meredith, Hans Oerter, and C. S. M. Doake. 1996. "Experimental Fracture and Mechanical Properties of Antarctic Ice: Preliminary Results." *Annals of Glaciology* 23: 284–92.

Rückamp, Martin, Niklas Neckel, Sophie Berger, Angelika Humbert, and Veit Helm. 2019. "Calving Induced Speed-up of Petermann Glacier." *Journal of Geophysical Research: Earth Surface*, January. https://doi.org/10.1029/2018JF004775.

Scambos, Ted, Christina Hulbe, and Mark Fahnestock. 2013. "Climate-Induced Ice Shelf Disintegration in the Antarctic Peninsula." In *Antarctic Research Series*, edited by Eugen Domack, Amy Levente, Adam Burnet, Robert Bindschadler, Pete Convey, and Matthew Kirby, 79–92. Washington, D. C.: American Geophysical Union. https://doi.org/10.1029/AR079p0079.

Shi, Lei, Christopher T. Allen, John R. Ledford, Fernando Rodriguez-Morales, William A. Blake, Ben G. Panzer, Stephen C. Prokopiack, Carlton J. Leuschen, and Sivaprasad Gogineni. 2010. "Multichannel Coherent Radar Depth Sounder for NASA Operation Ice Bridge." In *2010 IEEE International Geoscience and Remote Sensing Symposium*, 1729–32. Honolulu, HI, USA: IEEE. https://doi.org/10.1109/IGARSS.2010.5649518.

Shroyer, E. L., L. Padman, R. M. Samelson, A. MüNchow, and L. A. Stearns. 2017. "Seasonal Control of Petermann Gletscher Ice-Shelf Melt by the Ocean's Response to Sea-Ice Cover in Nares Strait." *Journal of Glaciology* 63 (238): 324–30. https://doi.org/10.1017/jog.2016.140.

Shroyer, Emily L., Roger M. Samelson, Laurie Padman, and Andreas Münchow. 2015. "Modeled Ocean Circulation in Nares Strait and Its Dependence on Landfast-Ice Cover: OCEAN CIRCULATION IN NARES STRAIT." *Journal of Geophysical Research: Oceans* 120 (12): 7934–59. https://doi.org/10.1002/2015JC011091.

Sicart, Jean Emmanuel, Regine Hock, and Delphine Six. 2008. "Glacier Melt, Air Temperature, and Energy Balance in Different Climates: The Bolivian Tropics, the French Alps, and Northern Sweden." *Journal of Geophysical Research* 113 (D24). https://doi.org/10.1029/2008JD010406.

Slater, Donald A., Dan N. Goldberg, Peter W. Nienow, and Tom R. Cowton. 2016. “Scalings for Submarine Melting at Tidewater Glaciers from Buoyant Plume Theory.” *Journal of Physical Oceanography* 46 (6): 1839–55. https://doi.org/10.1175/JPO-D-15-0132.1.

Steur, L. de, M. Steele, E. Hansen, J. Morison, I. Polyakov, S. M. Olsen, H. Melling, et al. 2013. “Hydrographic Changes in the Lincoln Sea in the Arctic Ocean with Focus on an Upper Ocean Freshwater Anomaly between 2007 and 2010: Hydrographic Changes In The Lincoln Sea.” *Journal of Geophysical Research: Oceans* 118 (9): 4699–4715. https://doi.org/10.1002/jgrc.20341.

Straneo, Fiammetta, Patrick Heimbach, Olga Sergienko, Gordon Hamilton, Ginny Catania, Stephen Griffies, Robert Hallberg, et al. 2013. “Challenges to Understanding the Dynamic Response of Greenland’s Marine Terminating Glaciers to Oceanic and Atmospheric Forcing.” *Bulletin of the American Meteorological Society* 94 (8): 1131–44. https://doi.org/10.1175/BAMS-D-12-00100.1.

Tinto, Kirsty J., Robin E. Bell, James R. Cochran, and Andreas Münchow. 2015. “Bathymetry in Petermann Fjord from Operation IceBridge Aerogravity.” *Earth and Planetary Science Letters* 422 (July): 58–66. https://doi.org/10.1016/j.epsl.2015.04.009.

Vaughan, David G., Hugh F. J. Corr, Robert A. Bindschadler, Pierre Dutrieux, G. Hilmar Gudmundsson, Adrian Jenkins, Thomas Newman, Patricia Vornberger, and Duncan J. Wingham. 2012. “Subglacial Melt Channels and Fracture in the Floating Part of Pine Island Glacier, Antarctica: SUBGLACIAL CHANNELS AND CREVASSING.” *Journal of Geophysical Research: Earth Surface* 117 (F3): n/a-n/a. https://doi.org/10.1029/2012JF002360.

Veen, C. J. van der. 1998. “Fracture Mechanics Approach to Penetration of Surface Crevasses on Glaciers.” *Cold Regions Science and Technology* 27 (1): 31–47. https://doi.org/10.1016/S0165-232X(97)00022-0.

Veen, C. J. van der. 1999. “Crevasses on Glaciers.” *Polar Geography* 23 (3): 213–45. https://doi.org/10.1080/10889379909377677.

Westergaard, H.M.W. 1939. “Bearing Pressures and Cracks” Journal of Applied Mechanics (6): A49–53.

Westergaard-Nielsen, Andreas, Mojtaba Karami, Birger Ulf Hansen, Sebastian Westermann, and Bo Elberling. 2018. “Contrasting Temperature Trends across the Ice-Free Part of Greenland.” *Scientific Reports* 8 (1). https://doi.org/10.1038/s41598-018-19992-w.

Wilson, Nat, Fiammetta Straneo, and Patrick Heimbach. 2017. “Satellite-Derived Submarine Melt Rates and Mass Balance (2011–2015) for Greenland’s Largest Remaining Ice Tongues.” *The Cryosphere* 11 (6): 2773–82. https://doi.org/10.5194/tc-11-2773-2017.